INFORMATION TO USERS

.

Effects of Anisotropy and Lateral Heterogeneities on Elastic waves and Mode Coupling in Shallow water

by

Minkyu Park

A dissertation submitted in partial fulfillment

of the requirements for the degree of

Doctor of Philosophy

University of Washington

1997

Approved by _____Robert J. Odom_____

(Chairperson of Supervisory Committee)

Program Authorized
to Offer Degree_____Geophysics_____

Date_____August 7, 1997_____

UMI Number: 9807015

Copyright 1997 by
Park, Minkyu

UMI

300 North Zeeb Road
Ann Arbor, MI 48103

In presenting this dissertation in partial fulfillment of the requirements for the Doctoral degree at the University of Washington, I agree that the Library shall make its copies freely available for inspection. I further agree that extensive copying of this dissertation is allowable only for scholarly purposes, consistent with "fair use" as prescribed in the U.S. Copyright Law. Requests for copying or reproduction of this dissertation may be referred to University Microfilms, 1490 Eisenhower Place, P.O. Box 975, Ann Arbor, Michigan 48106, to whom the author has granted "the right to reproduce and sell (a) copies of the manuscript in microform and/or (b) printed copies of the manuscript made from microform."

Signature

Date August 7, 1997

University of Washington

Abstract

Effects of Anisotropy and Lateral Heterogeneities on Elastic waves and Mode Coupling in Shallow water

by Minkyu Park

Chairperson of Supervisory Committee: Professor Robert I. Odom
Geophysics Program

Effects of anisotropy and lateral heterogeneities on elastic waves and mode coupling in shallow water is examined. Especially, the sensitivity of bottom interacting modes to transverse isotropy, the most common type of anisotropy of most marine sediments, is numerically studied based on the coupled mode theory of Maupin [Geophys. J. 93, 173-185 (1988)]. Effects of transverse isotropy on modal phase and group velocities, mode energy and mode coupling is quantitatively evaluated by numerical computation.

The range dependent shallow water signal propagation problem is also treated. Computation codes, which include the effects of bottom shear, transverse isotropy and general range dependence, are developed by an application of the invariant imbedding to Maupin's coupled mode theory. The mode coupling matrix and the reflection and transmission matrices are computed and the forward propagating and backward propagating waves in the frequency domain, and signals in the time domain are numerically generated for a realistic range dependent shallow water model.

The theory for the elastic wave scattering is developed by incorporating the effect of stochastic fluctuations of the interface boundaries into the elastic coupled mode

equations for 2-D range dependent media. Enforcing energy conservation on the system of the first order perturbation leads to a Lippmann-Schwinger type integral equation for the random medium propagator. These formal theoretical results are valid to all orders of multiple scattering. From the Born approximation solution of the Lippmann-Schwinger equation, the modal scattering cross section and the reciprocal scattering quality factor is numerically computed.

TABLE OF CONTENTS

LIST OF FIGURES

ACKNOWLEDGMENTS

DEDICATION

I dedicate this dissertation to my wife **Misook**.

Chapter 1

INTRODUCTION

The shallow water environment probably shows the most variation in character of all the various environmental ocean provinces. While some shallow water waveguides have small or gradual range variation for which an adiabatic descripton of the propagation is adequate, other shallow water regions can exhibit very strong range dependence requiring the introduction of mode coupling to accurately model the propagation process. It is the more strongly varying regions for which the adiabatic approach is not appropriate, and for which bottom interactions must be considered that we are concerned with in this thesis.

The range dependence of a strongly varying shallow water waveguide can be both geometric and material in nature. Fluctuations in water depth and layer thicknesses of bottom sediments impose geometric variations of the medium with range. Range dependent gradients in elastic parameters and density of individual layers further complicate the task of characterizing and understanding shallow water acoustic propagation. Adequate modeling and understanding of shallow water signals that interact strongly with the bottom require a proper treatment of the marine sediment and basement properties. Marine sediments typically exhibit finite shear wave speeds that are much less than the sound speed in the water column (Hamilton 1980; Ewing et al. 1992). The vertical gradients of the shear speed can be quite large, and velocity anisotropy is an almost universal feature of marine sediments, with transverse isotropy (TI) being the most common type of anisotropy (Bachman 1979; Bachman

1983; Oakley & Vidmar 1983; Carlson, Schaftenaar & Moore 1984).

Strong range dependence causes energy in an initially unidirectional propagating signal to be redistributed among forward and backward discrete and continuum modes. Inclusion of finite shear speed in the sediment is necessary to model the Stoneley wave propagating at the water sediment interface and to properly account for the component of transmission loss due to conversion to shear waves. Acoustic energy can be scattered from the water column into the Stoneley wave by range dependence of the water-sediment interface (Kuperman & Schmidt 1989). Assuming that the bottom properties are isotropic when they are really transversely isotropic can lead to underestimating sediment sound speed gradients, and overestimating sediment thickness and shear velocity (Fryer & Miller 1986). Also, as will be seen below, incorrectly assuming isotropy has a significant effect on the redistribution of acoustic energy through range dependence induced mode coupling.

The original formulation of the coupled mode equations for sound propagation in a range dependent ocean effected a local separation of the Helmholtz equation for the velocity potential or, equivalently, the pressure (Pierce 1965; Milder 1969). The pressure is represented as the superposition of a set of range varying basis functions, the "local modes," with range dependent amplitude coefficients. The elements of this local basis are chosen to be the modes of the plane layered structure that corresponds locally in terms of material properties and layer thicknesses to the range dependent structure. This approach leads to another second order differential equation that must be solved to obtain the range dependent modal amplitude coefficients. The right hand side of this equation consists of source terms quantifying the strength of the coupling between different local modes. The formulations presented by Pierce (1965) and Milder (1969) yield first and second order coupling coefficients that depend on the first and second order derivatives, respectively, with respect to the range coordinate of the local mode functions.

The second order coupling coefficients are cumbersome to deal with analytically.

They can be shown to depend on the second derivatives and the squares of the first derivatives with respect to the range coordinate of the boundary slopes and material parameters. Consequently, the second order coupling coefficients have been routinely ignored (Chwieroth et al. 1978; Rutherford and Hawker 1981; McDaniel 1982; Hall 1986).

It is interesting to note, however, that the presence of the second order coupling coefficients is an artifact of the formulation. It is a consequence of working with the Helmholtz equation (a second order differential equation) rather than directly with the coupled first order equations for the pressure and velocity. Odom (1980; 1986) has derived a local coupled mode theory directly from the field quantities pressure and velocity that contains all the modal interaction physics in a single coupling coefficient. This formulation exhibits explicit dependence on geometric and material gradients, and is mathematically and numerically more efficient. Boyles (1984) also derived a well known coupled mode theory based on the first order equations for an ocean with a range dependent surface and sound speed. Maupin (1988) extended the results of Odom (1980; 1986) to take elastic effects including anisotropy into account. We have applied Maupin's extensions to the case of fluid-elastic media in order to examine the mode coupling in a realistic shallow water model in Chapter 2.

One of the advantages of a coupled mode representation for propagation in a range dependent medium is that the physics of the propagation process can be unravelled mode by mode if desired. Since the coupled mode theory employs range independent local modes as a range varying basis, we have included a number of numerical examples that illustrate the effects of transverse isotropy on the local modes in Chapter 2. It is important to understand which characteristics of the basis are affected by the transverse isotropy in order to appreciate the effects on the mode coupling. The main result of Chapter 2 is the quantitative evaluation of the effect of anisotropy on the local mode basis and on the mode-mode coupling coefficients. Two particularly important points are that rather small departures from isotropy (2.4%) can produce

rather large (15%) changes in the phase velocity of bottom interacting modes. In addition the presence of sediment anisotropy actually suppresses mode coupling, forcing the interactions to be more nearest-neighbor like.

Chapter 2 has been published as: Odom, R.I., M. Park, J.A. Mercer, R.S. Crosson and P. Paik, Effects of transverse isotropy on modes and mode coupling in shallow water, *J. Acoust. Soc. Am.*, **100**, 2079-2092, 1996.

Chapter 3 treats computational aspects of modeling seismo-acoustic propagation in shallow water at low frequencies. The model is one in which the frequency and bottom geoacoustic properties are such that the bottom cannot be treated as either a perfectly rigid reflector or as a simple bulk absorber.

The shallow water/bottom/subbottom system form a waveguide which, in the most general case, may contain range dependent geometry and material properties. The bottom may also be anisotropic, but we are limited here to the relatively simple case of transverse isotropy (TI). The bottom may also be poroelastic. However we do not include that in this work.

For our treatment of the range dependent shallow water signal propagation problem, we use Maupin's (1988) formulation in terms of local coupled modes and we have developed FORTRAN code which includes the effects of bottom shear, transverse isotropy and quite general range dependence. A brief outline of the transformation of Maupin's coupled mode theory to a numerically stable form by the invariant imbedding technique is introduced in Section 3.1.

In Section 3.2, the deterministic and stochastic coupling matrices and the reflection and transmission matrices are computed and the forward-propagating and backward-propagating wave in the frequency domain, and signals in the time domain are numerically generated for a realistic range-dependent shallow water model.

Chapter 3 has been submitted for publication to *J. Acoust. Soc. Am.* as: Park, M. & R.I. Odom, Effects of elastic heterogeneities and anisotropy on mode coupling and signals in shallow water.

In Chapter 4, the effect of rough surfaces on elastic wave scattering is studied on the assumption that the models used to represent the earth for computational elastic wavefield modelling are all idealizations on some scale. Typical idealized earth models are the sphere or, on local or regional scales, a stack of constant velocity layers. More accurate representations of the real earth are developed by incorporating deterministic perturbations into the basic idealizations. Examples are ellipticity corrections to a spherical earth model or smooth velocity variations for plane layered models. Beyond these and several other commonly employed deterministic perturbations, the remaining deviations from the idealizations are usually assumed to be random. One advantage of making this assumption of randomness is that rather complicated perturbations, e.g., interface boundary roughness or volume velocity or impedance heterogeneities can be characterized by just a few parameters such as mean, variance, correlation length and, perhaps, some higher order statistical moments. In this chapter, we consider the effect of random interface boundary fluctuations on a layered reference structure. We employ Maupin's (1988) coupled mode theory for layered elastic media, so the deterministic reference structure may have rather arbitrary 2-D lateral heterogeneity or range dependence. We have incorporated the effects of random interface boundary fluctuations of strength ε into Maupin's theory using perturbation theory. In our perturbation expansion the $\mathcal{O}(1)$ equations are identical to Maupin's (1988) coupled mode equations. The $\mathcal{O}(\varepsilon)$ system of equations describes wave propagation in a range dependent layered medium with random interface fluctuations or roughness.

Many different methods have been used to study rough surface scattering. Reviews of the classical asymptotic methods are summarized in a number of books. Examples of those methods are perturbation theory (Bass and Fuks 1979), Kirchhoff approximation (Beckmann and Spizzichino 1963; Bass and Fuks 1979). DeSanto and Brown (1986) review the methods appropriate to the study of multiple scattering. A recent review of the theory and literature is found in the book by Ogilvy (1991).

Quite a bit of work on rough surface scattering is available in the ocean acoustics literature. Scattering from a rough sea bottom or ocean surface affects the performance of any system using acoustic energy in the ocean either for communication or oceanographic measurement. There is both experimental and theoretical evidence that rough surface scattering plays a significant role in the generation of the ambient noise field in the ocean and the microseimic noise field in the ocean bottom (Schreiner & Dorman 1990; Liu et al. 1993). We mention a few investigators treating problems similar to ours, or approaching the boundary roughness problem in a similar manner.

Kuperman (1975) applied a boundary perturbation method to seismo-acoustic wave scattering at random interfaces. Kuperman and Schmidt (1986) presented numerical results illustrating the effect of the generation of Stoneley waves as a loss mechanism for water borne acoustic signals. Their reference structure was a plane-layered fluid-solid medium. McDaniel and McCammon (1986) applied a coupled mode approach to the acoustic wavefield in an inhomogeneous fluid waveguide. Their theory is based on a 2nd order differential equation for the range dependent mode amplitudes. Bahar (1978, 1980) developed a spectral approach he termed the full wave method, and applied his method to acoustic wave scattering (Bahar 1990). He expanded the unknown scattered field in a complete set of orthonormal basis functions representing all possible modes, i.e., surface waves, head waves and body waves, resulting in a set of first-order coupled differential (Telegraphist's) equations. Bahar also employed a plain layered medium as a reference structure.

There are fewer references in the seismic literature about scattering from rough interfaces. Schultz & Toksöz (1993, 1994) studied enhanced backscattering from integral expressions for the wavefield singly scattered from a rough surface. Most research on seismic wave scattering is confined to volume scattering from the material property fluctuations or from discrete point-like scatterers. Aki (1969) first suggested that the seismic coda waves can be treated as single backscattered waves. Aki and Chouet (1975) investigated S wave scattering by random heterogeneities as the cause

for the seismic coda. The single scattering model was developed and used to model scattering loss in time and space (Sato 1977). Problems of higher-order scattering in 2-D and 3-D media with isotropic scatterers were studied (Kopnichev 1977; Gao et al. 1983a, b). Radiative transfer theory was used by Wu (1985) to study the seismic coda.

Section 4.1 covers a statistical description of rough surfaces. Section 4.2 describes the perturbation method we used to characterize the rough surface scattering. In Section 4.3, we construct a unitary vector space with the local modes as the basis vectors. In Section 4.4, we derive the propagating solutions for the primary field and scattered field from the Green's function for the elastic wave propagation problem. Section 4.5 covers the derivation of the spatial evolution equations and coupling matrices for the randomly perturbed medium. In Section 4.6, we derive the coupled mode propagator for 2-D laterally heterogeneous media, and in Section 4.7, we prove the unitarity of the propagator. In Section 4.8, we derive a Lippmann-Schwinger integral equation for the coupled mode propagator and derive the Dyson equation and Bethe-Salpeter equations for the mean of the propagator and its covariance, respectively.

Taking the Born approximation solution to the Lippmann-Schwinger equation, we derive an expression for the scattering attenuation Q_S^{-1} after defining a modal scattering cross section in Section 4.9. Section 4.10 describes an inverse problem for the roughness variance and roughness correlation length again based on the Born approximation to the Lippmann-Schwinger equation. The final section, Section 4.11, presents a summary and conclusions.

Chapter 4 is submitted for publication to *Geophy. J. Int.* as: Park, M. & R.I. Odom, The Effect of Stochastic Rough Interfaces on Coupled-Mode Elastic Waves.

Chapter 2

EFFECTS OF TRANSVERSE ISOTROPY ON MODE AND MODE COUPLING IN SHALLOW WATER

Most marine sediments exhibit transverse isotropy (TI) that can have a significant effect on the signal properties of strongly bottom interacting sound. Locally, transverse isotropy has the greatest effect on the fundamental and near fundamental modal overtones. The local shallow water TI modes have reduced amplitude in the sediment relative to the corresponding shallow water modes for an isotropic bottom. Even a small departure from isotropy (2.4%) can have a significant (15%) effect on the phase velocity of bottom interacting modes. Calculations of mode-mode coupling coefficients for a range dependent medium indicate that mode coupling is more strongly confined to modal nearest neighbors for a TI medium characterized predominantly by shear wave anisotropy, when compared to the corresponding isotropic medium. As the frequency increases, the strongest coupling occurs between higher overtones and also becomes more strongly peaked around nearest neighbors. The coupled mode theory of Maupin[Geophys. J. **93**, 173-185 (1988)] is employed to model the coupling. This theory can treat smooth gradients and sloping layer boundaries for all five of the bottom elastic moduli in a TI medium, the densities, and the range dependence of the water column itself. This coupled mode formulation also properly accounts for the continuity of stress and displacement boundary conditions in an exact way at irregular interfaces.

2.1 Theory

This section contains a brief, self-contained summary of the coupled mode theory for layered fluid-elastic media as developed by Maupin (1988). This theory should have wide applicability to bottom interacting ocean acoustics. A particularly important point is the treatment of the boundary conditions at the interface between two geometrically irregular layers. Rutherford and Hawker (1981) derived corrections to the eigenfunctions for a plane layered medium that satisfy the boundary conditions at irregular layer interfaces to first order in the interface slope. It is, however, possible to satisfy the boundary conditions at the irregular interface exactly by transforming inhomogeneous boundary conditions to homogeneous boundary conditions and adding an additional source term to the governing system of differential equations (Maupin 1988). This has recently been rediscovered by Fawcett (1993) for fluid media. Gillette (1994) introduced a local coordinate transformation that leads to a solution that exactly satisfies the boundary conditions for the case of a single perfectly rigid range dependent boundary. Gillette's problem can also be solved with the local mode theory described here without transforming to a special local coordinate system. In fact the following treatment of the coupled mode problem leads to a solution which exactly satisfies the range dependent boundary conditions at all interfaces with no approximations or neglected terms. As will be seen below, it is not necessary to construct depth functions satisfying boundary conditions involving normal derivatives on a range dependent boundary. This exact solution is also numerically tractible, and may be computed using any good normal mode code as the core program. The treatment is valid for solid-solid as well as fluid-solid and fluid-fluid boundaries. It is also valid for general anisotropic media. Our specific examples are carried out for transversely isotropic media with a vertical axis of symmetry.

2.1.1 Mode coupling in solid elastic media

We use a Cartesian coordinate system in which the x axis (or x_1 axis) is the direction of the range dependence, y-axis (or x_2 axis) is the axis along which there is no variation in medium properties, and z-axis (or x_3 axis) is the depth axis and taken to be positive downward. The particle displacement vector is $\mathbf{w} = (w_x, w_y, w_z)$.

For the elastic moduli, the matrix notation of Woodhouse (1974) is employed such that

$$(C_{ij})_{kl} = c_{kilj}. \tag{2.1}$$

Note that this is *not* the same as the widely used abbreviated subscript notation for the elasticity tensor as described by Auld (1990) for example. The individual C_{ij}'s in Woodhouse's notation are matrices, not individual matrix elements as in the abbreviated subscript notation.

The equations of motion for an elastic medium are

$$\rho \frac{\partial^2 \mathbf{w}}{\partial t^2} = \nabla_i \mathbf{t}_i + \mathbf{f}, \tag{2.2}$$

where ρ is the density, $\mathbf{f}$ is an external force and the traction vector $\mathbf{t}$ is defined by

$$\mathbf{t}_i = C_{ij} \left(\frac{\partial \mathbf{w}}{\partial x_j} \right), \tag{2.3}$$

where $\mathbf{w} = (w_x, w_y, w_z)$ and $\mathbf{t}_i = (\tau_{ix}, \tau_{iy}, \tau_{iz})$.

The displacement, Fourier transformed with respect to y and t, is represented as

$$\mathbf{w}(x, z, p, \omega) = \int_{-\infty}^{+\infty} \int_{-\infty}^{+\infty} \mathbf{w}(x, y, z, t) \exp(i(py - \omega t)) dy dt \tag{2.4}$$

where p is the spatial wave number in the y-direction. The equations of motion can then be written as

$$-\rho \omega^2 \mathbf{w} = \frac{\partial \mathbf{t}_1}{\partial x} - ip \mathbf{t}_2 + \frac{\partial \mathbf{t}_3}{\partial z} + \mathbf{f} \tag{2.5}$$

where

$$t_i = C_{i1}\frac{\partial \mathbf{w}}{\partial x} - ipC_{i2}\mathbf{w} + C_{i3}\frac{\partial \mathbf{w}}{\partial z}. \tag{2.6}$$

The same symbol $\mathbf{w}$ is used for both the transformed and untransformed displacement. The subsequent development is carried out completely in the (x, z, p, ω) domain, and there should be no confusion. The use of i as both an index and as $\sqrt{-1}$ should also be clear from context.

Introducing the 6-component displacement-stress vector $\mathbf{u} = (\mathbf{w}, \mathbf{t})^T$ where $\mathbf{w}$ is as defined above and $\mathbf{t} = \mathbf{t}_1 = (\tau_{xx}, \tau_{xy}, \tau_{xz})$, the equations of motion can be written as the first order system where the derivatives with respect to the propagation direction, that is, the direction of the range dependence of the structure, appear only on the left hand side of equation

$$\frac{\partial \mathbf{u}}{\partial x} = A\mathbf{u} - \left\{ \begin{array}{c} 0 \\ \mathbf{f} \end{array} \right\}. \tag{2.7}$$

The differential operator

$$A = \begin{pmatrix} -C_{11}^{-1}C_{13}\frac{\partial}{\partial z} + C_{11}^{-1}C_{12}ip & C_{11}^{-1} \\ -\rho\omega^2 - \frac{\partial}{\partial z}\left(Q_{33}\frac{\partial}{\partial z}\right) + ipQ_{23}\frac{\partial}{\partial z} + \frac{\partial}{\partial z}(Q_{32}ip) + p^2Q_{22} & -\frac{\partial}{\partial z}C_{31}C_{11}^{-1} + ipC_{21}C_{11}^{-1} \end{pmatrix} \tag{2.8}$$

does not depend on the horizontal derivatives. The matrices Q_{ij} are defined as

$$Q_{ij} = C_{ij} - C_{i1}C_{11}^{-1}C_{1j}. \tag{2.9}$$

The boundary conditions require the continuity of traction and displacement across interfaces. The free surface condition for an elastic (fluid) medium is that

the traction (pressure) vanishes and a radiation condition is assumed as $z \to \infty$. The interfaces of the range dependent medium are taken to be of the form $z = h(x)$ with normal n. Thus the slope of m-th interface can be written as

$$\frac{dz_m}{dx} = \frac{\partial h_m}{\partial x} = \dot{h}_m.$$ (2.10)

By introducing the inclination angle $\theta_m = \tan^{-1}(\dot{h}_m)$, the normal vector can be expressed as

$$\mathbf{n} = \sin \theta \hat{\mathbf{i}} - \cos \theta \hat{\mathbf{k}}.$$ (2.11)

The continuity of traction $\mathbf{T} = t_j n_j$ across m-th interface can be written as

$$\begin{aligned}
[\mathbf{T}] &= [t_1 \sin \theta_m - t_3 \cos \theta_m]_m \\
&= \frac{1}{\sqrt{1 + \dot{h}_m^2}}[t_3 - \dot{h}_m t]_m = 0.
\end{aligned}$$ (2.12)

The square brackets $[\cdot]_m$ indicate the jump of the enclosed quantity across the mth interface, taken from bottom to top. Consequently, we have

$$[t_3]_m = \dot{h}_m [t]_m.$$ (2.13)

The continuity of traction *normal* to a sloping interface is then equivalent to a *jump* in the traction along the vertical axis. The equations of motion (2.7) along with the interface boundary conditions (2.13) and the free surface and radiation conditions are an exact formal representation of the equations for the displacement-stress field in a range dependent layered elastic medium. What makes a solution of the problem difficult is the inhomogeneous form of the interface boundary condition Eq.(2.13). Historically this inhomogeneous boundary condition has been dealt with by ignoring the inhomogeneity (McDaniel 1982; Odom 1980; Odom 1986), and replacing it with the approximate homogeneous condition. That is, the condition that the normal component of the traction be continuous across interfaces was replaced by the condition that only the vertical component of the traction be continuous. A different

approach taken by Evans (1983) was to approximate the medium with a series of stepwise depth variations. Evans' formulation conserves energy and is an exact solution to the approximate problem. He points out that when stepwise coupled modes are applied to a problem with a semi-infinte halfspace bottom and a continuously varying water-sediment interface, his method is approximate. It was pointed out by Maupin (1988) that the traction discontinuity in the interface boundary conditions can be converted to a localized volume force located along the interface. This follows from a representation theorem for elastic media investigated by Burridge and Knopoff (1964). The resulting equivalent volume force becomes a source term on the right hand side of Eq.(2.7), and the interface boundary conditions become homogeneous. Equations (2.7) and (2.13) can now be written in the absence of body forces as

$$\frac{\partial \mathbf{u}}{\partial x} = A\mathbf{u} + \sum_m \dot{h}_m \left\{ \begin{array}{c} 0 \\ [\mathbf{t}]_m \delta(z - h_m(x)) \end{array} \right\}$$

(2.14)

with the interface conditions

$$[t_3]_m = [\mathbf{w}]_m = 0.$$

(2.15)

Equations (2.14) and (2.15) are a very important result. This first order system of inhomogeneous equations with homogeneous boundary conditions formally describes the evolution of the displacement-stress fields along the range direction. The solution to this system will now be expressed in terms of coupled local modes. These local modes, defined below, are the eigenfunctions of the *range independent* medium that locally share the same depth dependence as the *range dependent* medium. This means that locally at some point x_0 in range, the density $\rho(x_0, z)$ and the elastic moduli $C_{ij}(x_0, z)$ are taken to be functions of depth only so that

$$\rho(x_0, z) = \rho(z) \quad \text{and} \quad C_{ij}(x_0, z) = C_{ij}(z).$$

(2.16)

The wave propagation problem for a 2-dimensional range dependent medium can

be solved exactly in terms of the eigenfunctions of the range independent medium. These eigenfunctions are the homogeneous solutions to Eq.(2.14) with homogeneous boundary conditions Eq.(2.15). The boundary conditions at the irregular interfaces are satisfied exactly by including the effective source term in Eq.(2.14). No approximations have been made.

Local homogeneous solutions of the equations of motion (Eq.(2.14)) which depend parametrically on x are represented as

$$\mathbf{u}(x_0, z)\exp\{-ik^r(x_0)x\} \tag{2.17}$$

with $\mathbf{u}$ satisfying

$$-ik^r(x_0)\mathbf{u}^r(x_0, z) = A\mathbf{u}^r(x_0, z) \tag{2.18}$$

and the homogeneous boundary conditions $[\mathbf{w}^r]_m = 0$ and $[\mathbf{t}_3^r]_m = 0$ across interfaces. The horizontal wave number in the x-direction is $k^r(x_0)$, and taken to be real.

The final definition required is the following scalar product between two local eigenfunctions of index r and q.

$$\langle \mathbf{u}^q, \mathbf{u}^r \rangle = i \int_0^\infty (\mathbf{w}^{q*}\mathbf{t}^r - \mathbf{t}^{q*}\mathbf{w}^r)dz \tag{2.19}$$

where $*$ indicates complex conjugation. The scalar product (2.19) is Hermitian, i.e.

$$\langle f, g \rangle = \langle g, f \rangle^*. \tag{2.20}$$

The local modes at fixed values of frequency and p are orthogonal with respect to this scalar product. The local modes are normalized such that

$$\langle \mathbf{u}^q, \mathbf{u}^r \rangle = \delta_{rq}. \tag{2.21}$$

Thus, they all carry the same energy flux across planes $x = $ constant.

The basic idea of the coupled local mode technique is to seek a solution for the equations of motion as a coupled set of local modes whose amplitudes and phases vary with laterally varying structure. The evolution of the range dependent amplitude determines how energy is exchanged between modes as a signal propagates through the medium. The solution of the equations of motion for the displacement-stress field in the range dependent medium is represented as the sum over forward(+) and backward(−) propagating local modes

$$\mathbf{u} = \left\{ \begin{array}{c} \mathbf{w} \\ \mathbf{t} \end{array} \right\} = \sum_r c_r^{\pm}(x) \exp\left(\mp i \int_0^x k^r(\zeta) d\zeta \right) \left\{ \begin{array}{c} \mathbf{w}^r(x,z) \\ \mathbf{t}^r(x,z) \end{array} \right\}, \qquad (2.22)$$

where $k(\zeta)$ is the local horizontal wavenumber. The local modes satisfy the homogeneous boundary conditions, Eq.(2.15), of a plane layered medium, and can therefore be computed with any appropriate normal mode code.

The derivation of the evolution equation for the range dependent amplitude coefficients $c_r(x)$ proceeds in the same fashion as previous coupled mode developments. The representation Eq.(2.22) is substituted into the equations of motion Eq.(2.14). The scalar product of the resulting expression is formed with the displacement-stress vector of the qth mode $\mathbf{u}^q$, yielding:

$$\frac{\partial c_q}{\partial x} = B_{qr} c_r \qquad (2.23)$$

with the coupling matrix

$$B_{qr} = \{-\langle \mathbf{u}^q, \frac{\partial \mathbf{u}^r}{\partial x} \rangle + i \sum_m h_m \mathbf{w}^{q*}[\mathbf{t}^r]_m\} \exp\left(i \int_0^x (k^q - k^r) d\zeta \right) \qquad (2.24)$$

In the case of very weak range dependence, we can set

$$B_{qr} = 0, \qquad (2.25)$$

indicating that individual modes propagate independently without interacting. This is the adiabatic approximation (Pierce 1965; Milder 1969; Woodhouse 1974; Nagl et al. 1978). The validity of the adiabatic approximation requires that the medium properties change very slowly with range. The total change can actually be quite large, but the rate of change with range must be small enough so that modes do not exchange energy among each other and are able to adjust their shapes to the local environment. Backscattering is automatically excluded by the adiabatic approximation, as is radiation to the continuum. A medium characterized by layer thicknesses or material properties that change significantly over a mode equivalent ray cycle distance will not be well modeled by the adiabatic approximation.

The form of the coupling matrix in Eq.(2.24) is not well suited to numerical computation because of the presence of the range derivatives of the local mode functions. The coupling matrix B_{qr} can be transformed so that the only range derivatives appearing in the expression are of the density and elastic moduli within layers and of the interface functions $h_m(x)$ at layer boundaries. We have relegated to the Appendix the lengthy expression for B_{qr}, and a discussion of extra terms required at fluid-solid interfaces.

The coupling matrix Eq.(A.1) involves an integral term related to the lateral derivative of the elastic moduli and density inside the layers. The interface term is a combination of an expression derived from the continuity conditions and another arising from jumps in the lateral derivatives of the elastic coefficients. It is the former of the these two interface terms that appears as the effective volume source term on Eq.(2.14). There are no range derivatives of the local eigenfunctions, and there is no need to introduce a special coordinate system. The expression(A.1) describes the coupling in a fully anisotropic 2-dimensional medium. The form of the matrices C_{ij} and Q_{ij} for a transversely isotropic medium have been given by Maupin (1992) and we do not repeat them here.

In order to synthesize a complete signal propagating in a strongly range dependent

medium for which the adiabatic approximation is not valid, we must solve the evolution equation Eq.(2.23) for the mode amplitudes. A complete solution for a strongly range dependent medium must account for the interaction of both forward($+$) and backward($-$) propagating modes. The evolution of both the forward and backward propagating components of a signal is described by

$$\frac{\partial}{\partial x}\begin{pmatrix} \mathbf{c}^+(x) \\ \mathbf{c}^-(x) \end{pmatrix} = \begin{pmatrix} \mathbf{B}^{++}(x) & \mathbf{B}^{+-}(x) \\ \mathbf{B}^{-+}(x) & \mathbf{B}^{--}(x) \end{pmatrix} \begin{pmatrix} \mathbf{c}^+(x) \\ \mathbf{c}^-(x) \end{pmatrix} \qquad (2.26)$$

where $\mathbf{c}^+$ and $\mathbf{c}^-$ are n-dimensional vectors whose elements are the amplitude coefficients of n forward and backward propagating modes. The $n \times n$ matrices $\mathbf{B}^{++}$, $\mathbf{B}^{+-}$, $\mathbf{B}^{-+}$ and $\mathbf{B}^{--}$ describe forward-to-forward, forward-to-backward, backward-to-forward and backward-to-backward coupling, respectively. The two point boundary value problem described by Eq.(2.26) is not numerically stable. However, Eq.(2.26) can be recast as a set of coupled Riccati equations for the reflection and transmission coefficients of the range dependent region (Kennett 1984), which is stable. We are in the process of doing this.

2.1.2 Energy conservation

As indicated by Eq.(2.21), the local modes are normalized to carry the same energy flux across planes $x =$ constant. We can obtain a statement of energy conservation for a lossless range dependent medium by substituting the local mode representation of the displacement-stress field Eq.(2.22) into the scalar product Eq.(2.19) and setting the derivative with respect to x equal to 0, yielding

$$\begin{aligned} \frac{\partial}{\partial x}\langle \mathbf{u}^q, \mathbf{u}^r \rangle &= \frac{\partial}{\partial x}\sum_q |c_q(x)|^2 \\ &= \sum_q \left(\frac{\partial}{\partial x}c_q(x)c_q^*(x) + c_q(x)\frac{\partial}{\partial x}c_q^*(x) \right) \end{aligned}$$

$$= \sum_{q,r} \left(B_{qr} + B_{rq}^* \right) c_r(x) c_q^*(x)$$

$$= 0. \tag{2.27}$$

We have used the fact that

$$\sum_q c_q(x) \left(\sum_r B_{qr}^* c_r^*(x) \right) = \sum_r c_r(x) \left(\sum_q B_{rq}^* c_q^*(x) \right), \tag{2.28}$$

since the mode indices $\{q, r\}$ are summed over the same set.

The only way for Eq.(2.27) to be satisfied generally is for the coupling matrix to be anti-Hermitian, i.e.

$$B_{qr} = -B_{rq}^*. \tag{2.29}$$

This anti-Hermiticity is a necessary consequence of energy conservation in a lossless medium. It can be seen by inspection that the coupling matrix B_{qr} given by Eq.(A.1) is anti-Hermitian. The additional coupling terms for the fluid layer and interface, Eq.(A.2) and Eq.(A.3) are also anti-Hermitian.

An obvious consequence of Eq.(2.29) is that

$$Re(B_{rr}) = 0. \tag{2.30}$$

If we insist that the phase of the local modes be continuous from point to point in the medium then we should also choose

$$Im(B_{rr}) = 0. \tag{2.31}$$

In the abiabatic case where all cross branch coupling can be ignored, the phase of the modes is just as shown in Eq.(2.22), which varies smoothly from point to point.

2.1.3 Specification of a transversely isotropic medium

Elastic anisotropy is a well established geoacoustic property of marine sediments (Bachman 1979; Bachman 1983; Oakley & Vidmar 1983; Carlson, Schaftenaar & Moore 1984). The most common form of anisotropy observed in marine sediments is transverse isotropy(TI) with a vertical axis of symmetry. In a TI medium propagation in all azimuthal directions lying in planes including the symmetry axis is equivalent. In TI marine sediments with vertical symmetry axes, horizontally polarized and horizontally propagating waves travel faster than vertically propagating and vertically polarized waves. The primary mechanisms for transverse isotropy in marine sediments are: 1. aligned cracks and pores; 2. recrystallization of anisotropic minerals; and 3. compositional layering on a very fine scale. If isotropy is erroneously assumed sound speed gradients are underestimated, sediment layer thicknesses can be overestimated and shear velocity can be overestimated (Fryer & Milder 1986). The most likely mechanism for the observed transverse isotropy of sediments at the water-bottom interface is compositional layering. Recrystallization of anisotropic minerals may be important for deeper lying sediments, but to depths of at least 1 km beneath the ocean bottom, compositional layering is believed to be the dominant mechanism (Carlson, Schaftenaar & Moore 1984).

In order to specify the anisotropy, we introduce the dimensionless parameters

$$\eta' \;=\; 1 - \eta \;=\; 1 - \frac{F}{A - 2L}, \tag{2.32}$$

and

$$\phi' \;=\; 1 - \phi \;=\; 1 - \frac{C}{A}, \tag{2.33}$$

Values of

$$\eta' = 0 \quad \text{and} \quad \phi' = 0 \tag{2.34}$$

indicate isotropy. The departure from isotropy increases as η' and/or ϕ' change from 0.

The dynamic stability of a transversely isotropic medium requires that certain conditions be imposed on the elastic moduli (Auld 1990; Postma 1955; Backus 1962):

$$A \geq N \geq 0,$$
$$C \geq 0,$$
$$L \geq 0,$$
$$F^2 \leq C(A - N). \tag{2.35}$$

The most plausible physical mechanism for TI with a vertical symmetry axis within the interfacial sediments is fine compostional layering. This mechanism imposes the additional constraints

$$C \geq F,$$
$$C \geq \frac{4}{3}L,$$
$$N \geq L \tag{2.36}$$

(Backus 1962). A final independent inequality constraint for compositionally layered TI media is

$$(A - L)(C - L) \geq (F + L)^2 \tag{2.37}$$

(Postma 1955; Berryman 1979).

When $A = C = \lambda + 2\mu$, $L = N = \mu$, and $F = \lambda$ the medium is isotropic. The relationship between the notation of Love (1944) and the abbreviated subscript notation for the elastic moduli of a TI medium is

$$A = c_{11}, \quad F = c_{13}, \quad C = c_{33}, \quad L = c_{44}, \quad N = c_{66}.$$

This concludes our summary of the complete 2-D coupled mode theory. This theory incorporates an exact treatment of the boundary conditions at sloping interfaces as well as being able to handle smooth gradients in density and all elastic moduli. We have applied the theory to a transversely isotropic medium with a vertical symmetry axis. The theory is, however, valid for general anisotropic media at the expense of additional algebraic and numerical complexity. In a general anisotropic medium the horizontally polarized shear waves do not decouple from the compressional waves and vertically polarized shear waves. Consequently, the motion is represented by a single 6×6 system of equations rather than the separate 4×4(P-SV) and 2×2(SH) systems required for isotropic and transversely isotropic media.

2.2 Numerical Results

In this section we numerically investigate the effects of transverse isotropy on the modal dispersion, eigenfunctions and the coupling matrix B_{qr} for a realistic shallow water model. We have not performed calculations for a specific range dependent model; we concentrate instead on the material properties.

We have examined the effect of transverse isotropy on the mode structure and mode coupling of a bottom interacting signal propagating in shallow water. The code used to generate the eigenvalues, eigenfunctions and kinetic energy integrals for a plane layered fluid-elastic TI medium was DISPER80 (Saito 1988). The computations were carried out on a Sun SPARCstation LX, mostly in double precision. At the highest frequencies it was necessary to employ quadruple precision for the first few eigenvalues and eigenfunctions. Our shallow water model was taken from Berge et al. (1991) who analyzed multi-component seismic data from an experiment conducted in 21 m of water about 10 km east of New Jersey.

The data analyzed by Berge et al. (1991) were collected in 1986 by Roundout Associates Inc. and Woods Hole Oceanographic Institution. Initial attempts at mod-

eling the data assuming isotropy of the bottom material were not considered adequate (1991), and led to further modeling efforts employing an anisotropic reflectivity program. The resulting TI models estimated by Berge et al. (1991) provided a good fit to their data and constrained four of the five elastic parameters necessary to describe a TI medium. They did not have enough resolution to determine the compressional wave anisotropy and assumed $c_{11} = c_{33}$ ($A = C$ in Love's (1944) notation).

2.2.1 The shallow water model

The model, shown in Fig. 2.1, consists of a 21 m thick isovelocity water layer over 12.5 m of TI sediments, followed by 12.5 m of isotropic sediments with a steep gradient in both compressional and shear speeds. The density of the sediments is taken to be constant at 2100 kg/m^3. The TI layer is characterized by $\eta' = 0.012$ and $\phi' = 0$. The base of the model is an isotropic elastic half-space with a shear speed of 1450 m/s, a compressional speed of 3000 m/s, and a density of 2400 kg/m^3.

We have explicitly focused on the qP-qSV component of propagation in the sediments. The excitation of horizontally polarized shear waves(SH) in the sediments by a propagating acoustic signal in the water requires 3-D heterogeneity or anisotropy of a more general nature than we treat.

2.2.2 Dispersion curves, eigenfunctions and normalization

Fig. 2.2 illustrates the phase velocity dispersion for the model of Fig. 2.1. The modal phase velocities for the TI model are generally higher than for the corresponding isotropic medium. This was apparently first noted by Stoneley (1949), and is a consequence of greater material stiffness sampled by components of wave particle motion parallel to the bedding plane. The difference between the modal phase velocities for the TI and isotropic media increases with increasing frequency. As the frequency increases, the phase velocity of the TI mode can approach the phase velocity of the

Figure 2.1: The transversely isotropic shallow water model of Berge et al. (1991) (Their **Table1.**). The 12.5m thick sediment layer immediately below the water sediment interface is transversely isotropic. We have terminated their model with an isotropic half-space with a shear speed of 1450 m/s, a compressional wave speed of 3000 m/s and a density of 2400 kg/m^3.
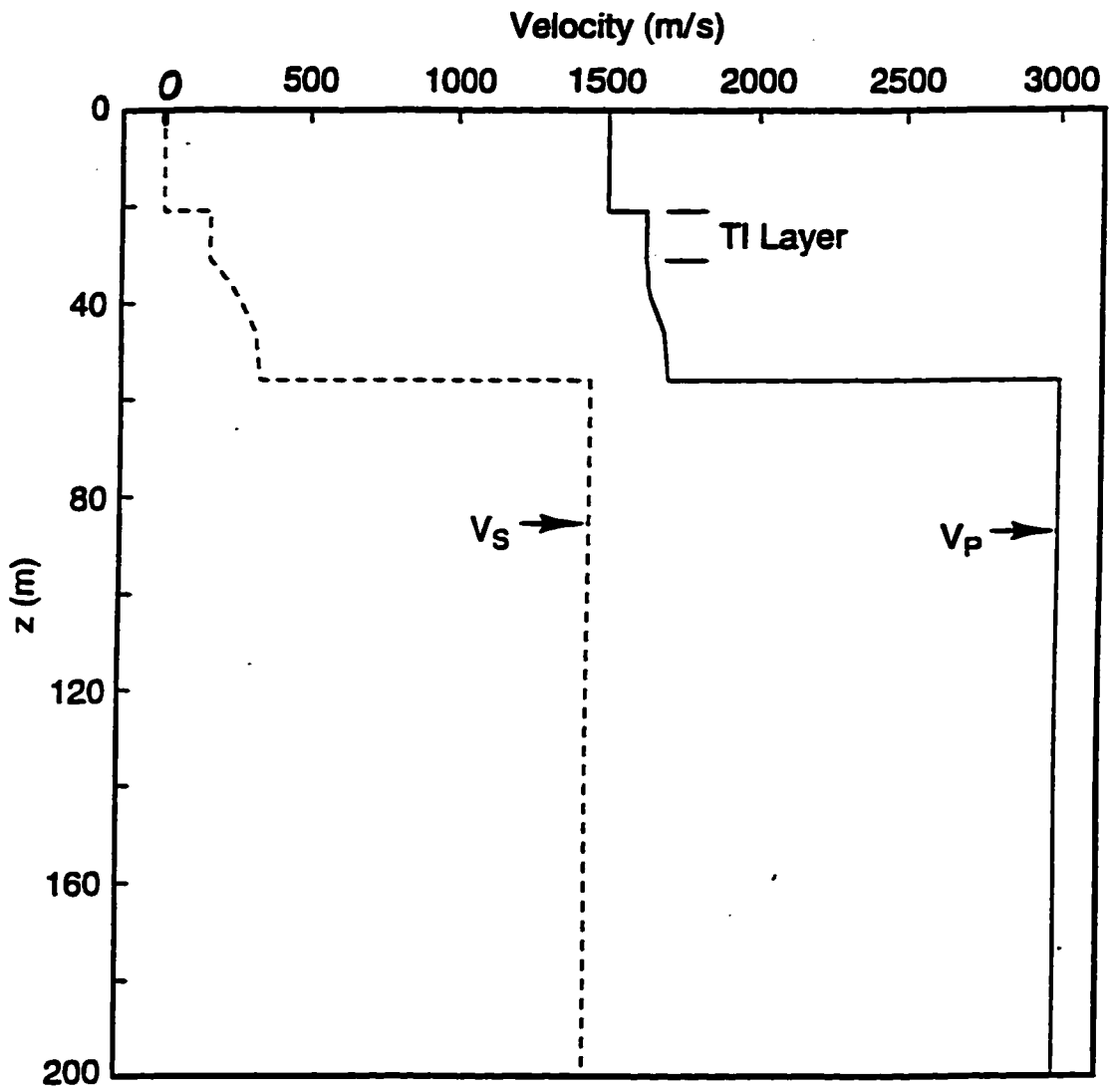
next higher isotropic mode. This is also evident in the group velocity curves shown in Fig. 2.3.

Despite a relatively small difference in the fundamental mode phase velocity between the TI and isotropic models, the eigenfunctions are substantially different. Because the eigenfunction calculation depends on the inverse of the eigen-phase velocity, small changes in the smallest eigen-phase velocity can have significant effects on the computation of the corresponding eigenfunction. This is also the reason for using quadruple precision at the higher frequencies for the first few modes. DIS-PER80 directly integrates the equations of motion which become quite stiff at high frequencies. Efficient methods of generating the fluid-elastic modes are important for high frequency applications.

The eigenfunctions for the vertical component of displacement at $10Hz$ and $20Hz$ are shown in Fig. 2.4 and Fig. 2.5, respectively. Although it is not visible on the scale at which the modes are plotted, all eigenfunctions have been normalized such that the vertical component of displacement is unity at the sea surface. The scale of the other three components of the eigenfunctions is derived from this normalization. This choice of normalization is somewhat arbitrary and merits discussion since the energy integrals and their partial derivatives (Fig. 2.6(a-c), Fig. 2.7 and Fig. 2.8), and the fundamental eigenfunctions in Fig. 2.9 are computed using this normalization. The computations for Fig. 2.10 use the normalization specified by Eq.(2.21 with each mode normalized to carry the same energy flux across planes $x =$ constant as required by the derivation of the coupled mode equations. The purpose of Fig. 2.4 and Fig. 2.5 is to illustrate the effect of the transverse isotropy on the eigenfunctions. The eigenfunctions could have been normalized so the isotropic and corresponding TI eigenfunctions had equal energy, or so that they had equal peak amplitudes or equal amplitudes at the water sediment interface. Although we have not computed the Green's function for the medium, which forces the selection of an explicit source location, we are assuming that the source and receiver are located within the water

Figure 2.2: Phase velocity dispersion curves for the shallow water model of Fig. 2.1. Note that the phase velocities in the TI medium are generally higher than in the equivalent isotropic medium. As the frequency increases, the phase velocity of a TI mode can approach the phase velocity of the next higher isotropic mode. This is also true of the group velocities plotted in Fig. 2.4.
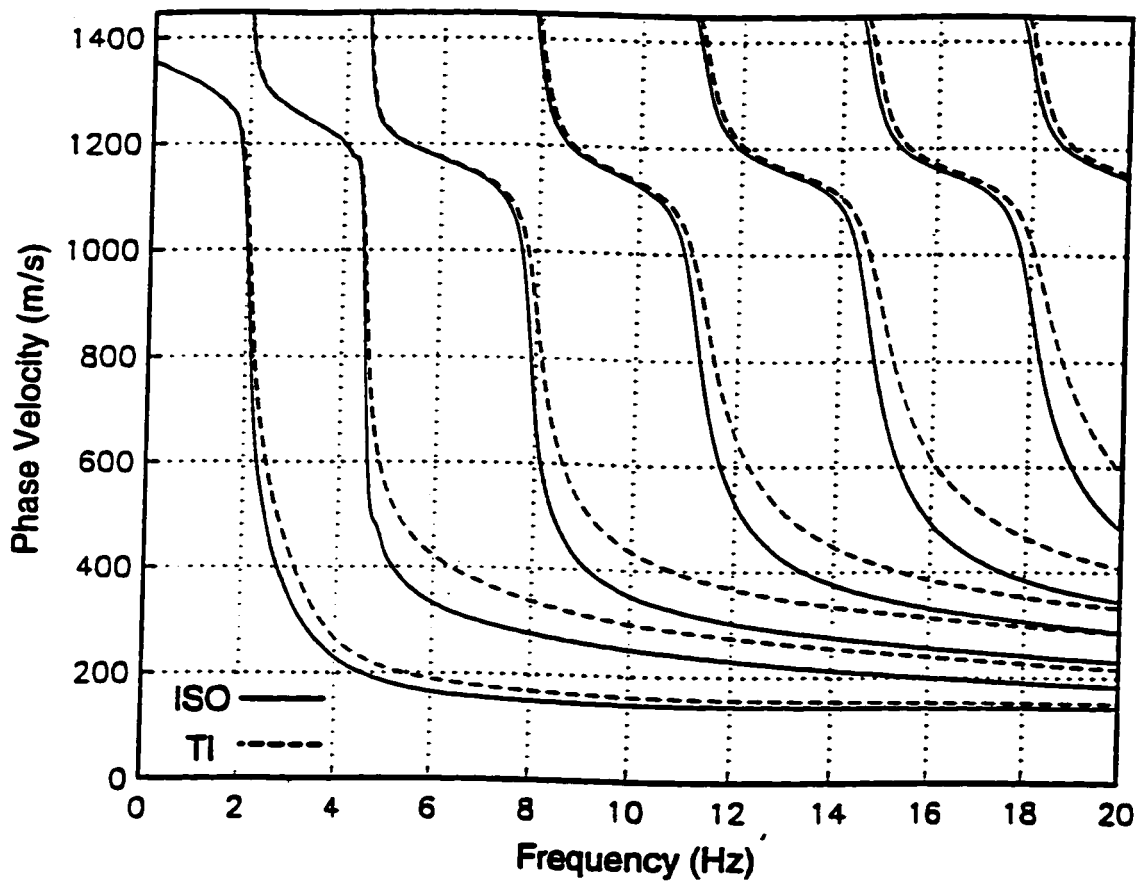
Figure 2.3: Group velocities of the first three modes for the model shown in Fig. 2.1.
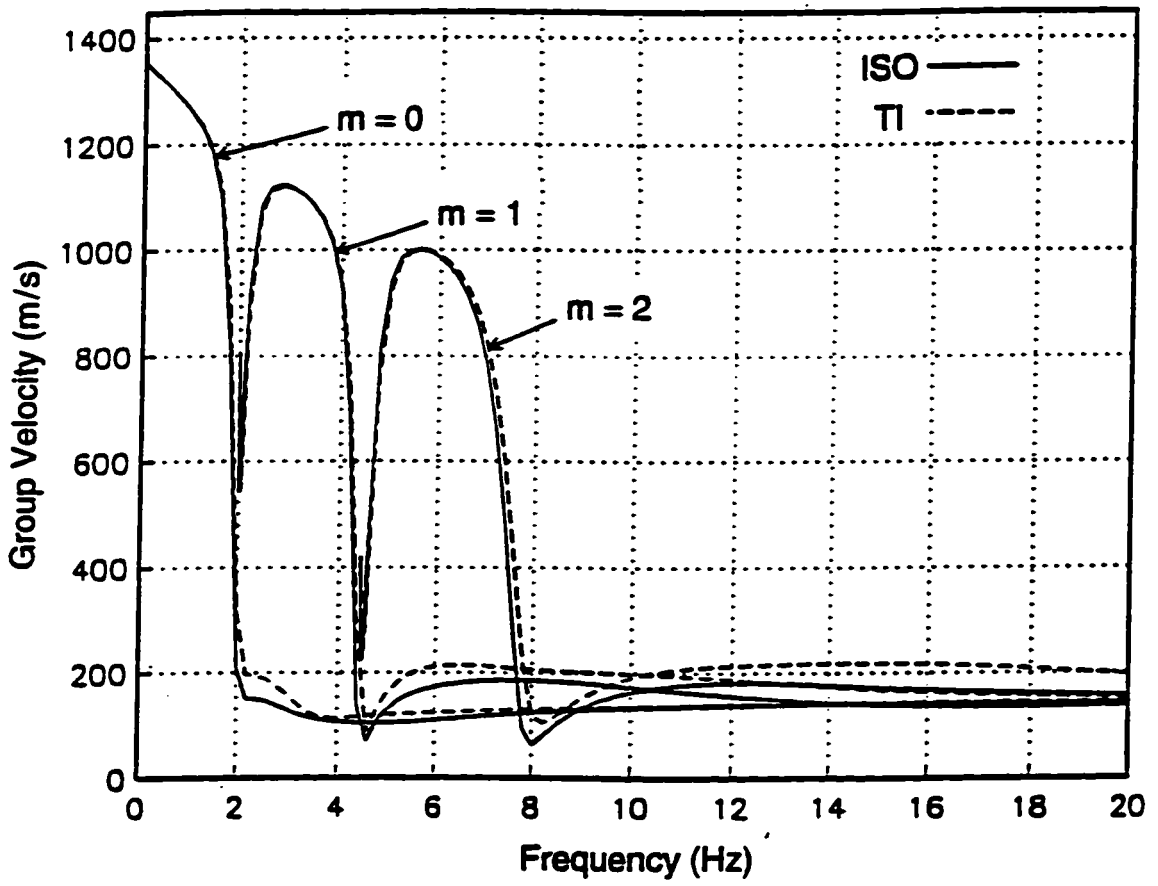
column or at, or slightly beneath, the water-sediment interface. Our chosen normalization emphasizes differences near the water-sediment interface. Modes with a given surface amplitude will have very different amplitudes at the water-sediment interface depending on whether the bottom is isotropic or anisotropic. Had we chosen a normalization such that the peak vertical displacement was unity, corresponding amplitudes in the water column would be quite different. Our normalization yields eigenfunctions with different energies in isotropic and corresponding TI media, but because they have the same vertical displacement at the surface, the differences in energy reflect the different amount of energy input into the medium required to produce the same surface displacement. The contribution of an individual mode to the Green's function for the medium is directly proportional to the mode amplitude at the chosen source depth. Therefore our choice of normalization will emphasize differences resulting from shallow sources.

Comparison of eigenfunctions between isotropic and anisotropic media is somewhat problematic in any case, since there is no simple method of establishing correspondence between the two. Because of the constraint relations among the elastic parameters listed earlier, it is not possible to arbitrarily perturb one elastic modulus without corresponding perturbations to other moduli. Arbitrary perturbations to elastic moduli can destroy the symmetry of the elastic stiffness tensor and produce unphysical results in calculations.

In the 10-20 Hz frequency range the water depth is approximately $\lambda/4$, which means that the bottom is near an acoustic radiation maximum. A propagating acoustic signal in this band will thus be dominated by the fundamental mode guided along the water sediment interface. For frequencies greater than approximately 7 Hz for the isotropic medium and 11 Hz for the TI medium, the phase velocity of the fundamental mode is less than the sediment shear speed at the water sediment interface. The fundamental mode above the threshhold frequency is therefore a Stoneley wave. At frequencies lower than the threshhold, the mode is more properly termed a pseudo-

Figure 2.4: The vertical displacement eigenfunctions for the first four modes at 10 Hz. Notice that for mode 3, the isotropic and TI vertical displacements are virtually identical, but that the amplitude of the TI displacement in the halfspace is slightly greater than the isotropic displacement. Modes are normalized to have unit vertical displacement at the water surface. At 10 Hz, the signal is dominated by the fundamental (Stoneley) mode.

Vertical Displacement, w_z

1000   2000   3000   4000

0

40

80

z (m)

120

160

200

Mode 0

ISO ———

TI - - - -

Vertical Displacement, w_z

-150   -100   -50   0   50   100

0

40

80

z (m)

120

160

200

Mode 1

ISO ———

TI - - - -

Vertical Displacement, w_z

-20   -10   0   10   20   30

0

40

80

z (m)

120

160

200

Mode 2

ISO ———

TI - - - -

Vertical Displacement, w_z

0   1   2   3   4

0

40

80

z (m)

120

160

200

Mode 3

ISO ———

TI - - - -
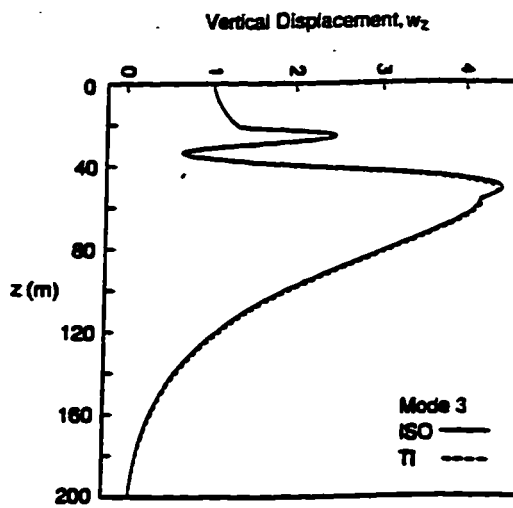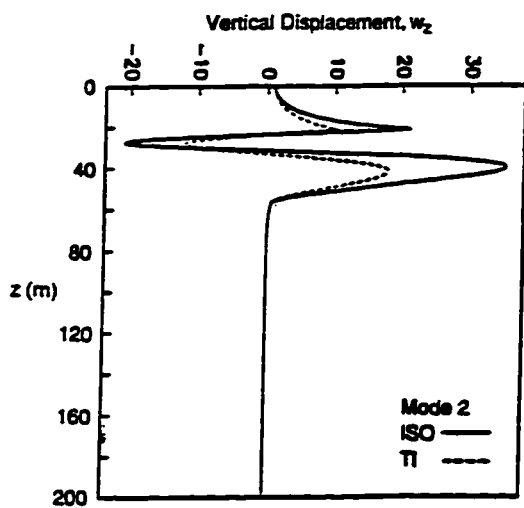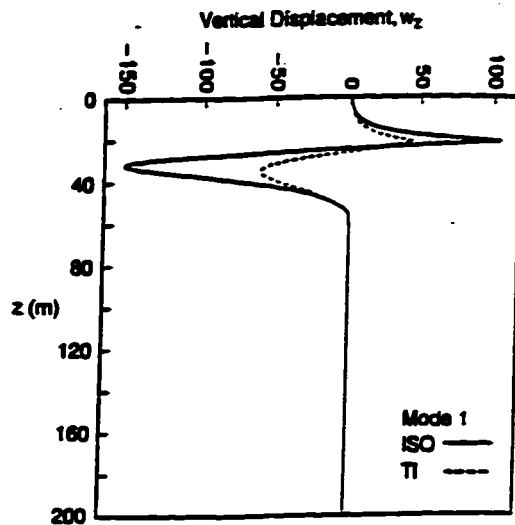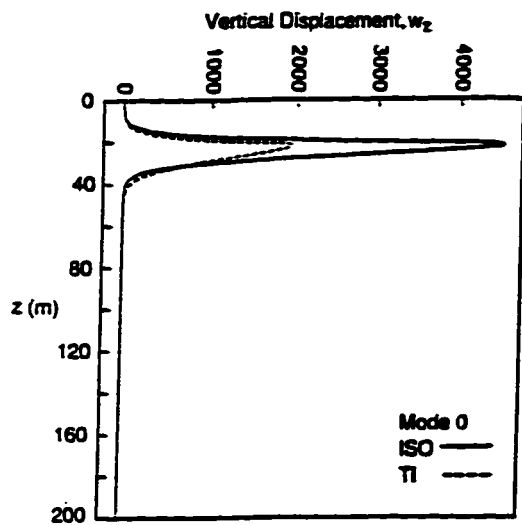
Figure 2.5: The vertical displacement eigenfunctions for the first four modes at 20 Hz. The isotropic and TI modes are distinct. In fact, although not shown here, there are significant differences between the isotropic and TI modes for the first five modes.

Vertical Displacement, w_z

Mode 0
ISO
TI

Vertical Displacement, w_z

Mode 1
ISO
TI

Vertical Displacement, w_z

Mode 2
ISO
TI

Vertical Displacement, w_z

Mode 3
ISO
TI
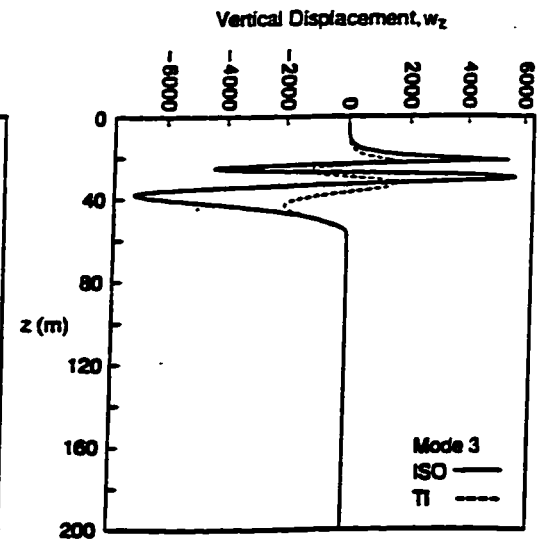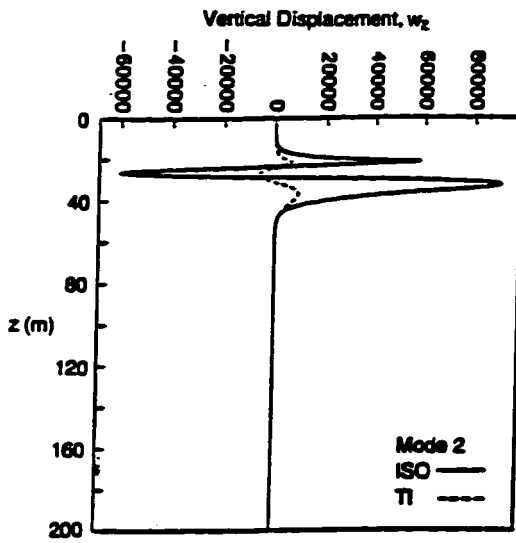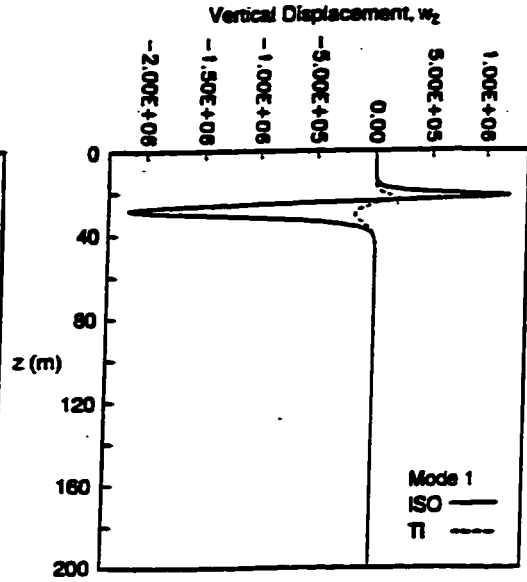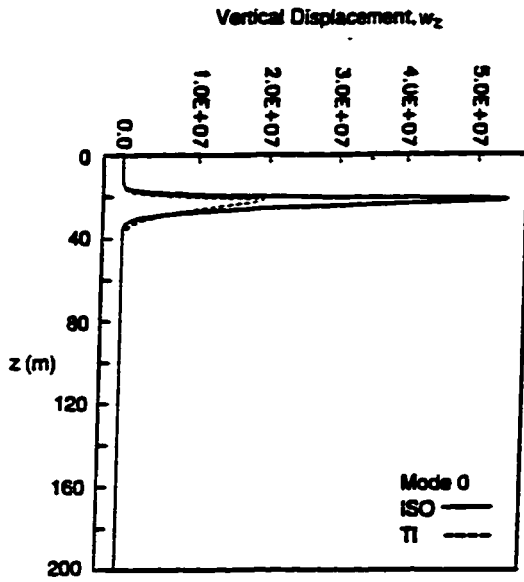
Rayleigh wave.

It can be clearly seen from Fig. 2.4 and Fig. 2.5 that the fundamental carries the most energy in this frequency band. The generally smaller peak amplitude of the low order TI modes relative to the isotropic modes is a consequence of the greater material stiffness for horizontally propagating waves in the TI medium. As the mode number increases for a given frequency, the eigenfunctions persist to greater depths in the structure. The fractional amount of modal energy within the 10 m thick TI layer decreases, so the influence of the anisotropy on the eigenfunctions also decreases. Also, as the frequency of a given mode increases the component of the mode in the bottom becomes more and more like pure SV. It can be seen from Fig. 2.2 that as the frequency of a mode increases, its phase velocity approaches the shear speed at the sediment interface. The compressional speed is much higher than the sediment shear speed, and so the compressional component of the mode is evanescent, leading to the almost pure SV behavior of the modes at high frequency.

2.2.3 Mode kinetic energy

Fig. 2.6 (a-c) shows the relative mode kinetic energy as a function of frequency for the first three modes. The kinetic energy E_m of the mth mode is

$$E_m = \omega^2 \int_0^\infty \rho \left(w_x^m w_x^{m*} + w_z^m w_z^{m*} \right) dz. \tag{2.38}$$

The energy in the Stoneley wave peaks at around $11 Hz$. Berge et al. (1991) have plotted amplitude vs. frequency for the unfiltered vertical component of the data from one of their profiles. (Their Figure 7, and here reproduced as our Fig. 2.6d.) The main features of the lower frequency part of their spectrum are reasonably well represented by our kinetic energy plots. The low amplitude maxima appearing at 1.8 Hz and 5 Hz in Fig. 2.6a and Fig. 2.6b, respectively, and the kink at approximately 8 Hz in Fig. 2.6c occur at the knees of the modal dispersion curves(Fig. 2.2). These

Figure 2.6: Kinetic energy as a function of frequency for the first three modes (a-c). These match quite well the lower frequency part of the spectrum of some shallow water data (d) shown by Berge et al.[33] (Their Fig. 2.7, used by permission of Blackwell Scientific Publications Ltd.) The Stoneley wave peak at about 11 Hz in Berge et al.[33] appears to be particularly well modeled by our mode calculations. Note that the frequency ranges of (a-c) and (d) are not the same.

(a) m = 0
(b) m = 1
(c) m = 2
(d)
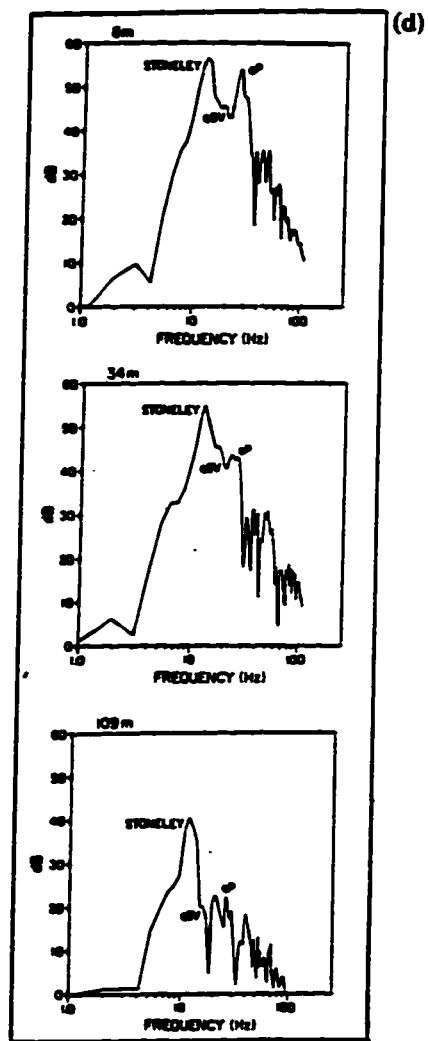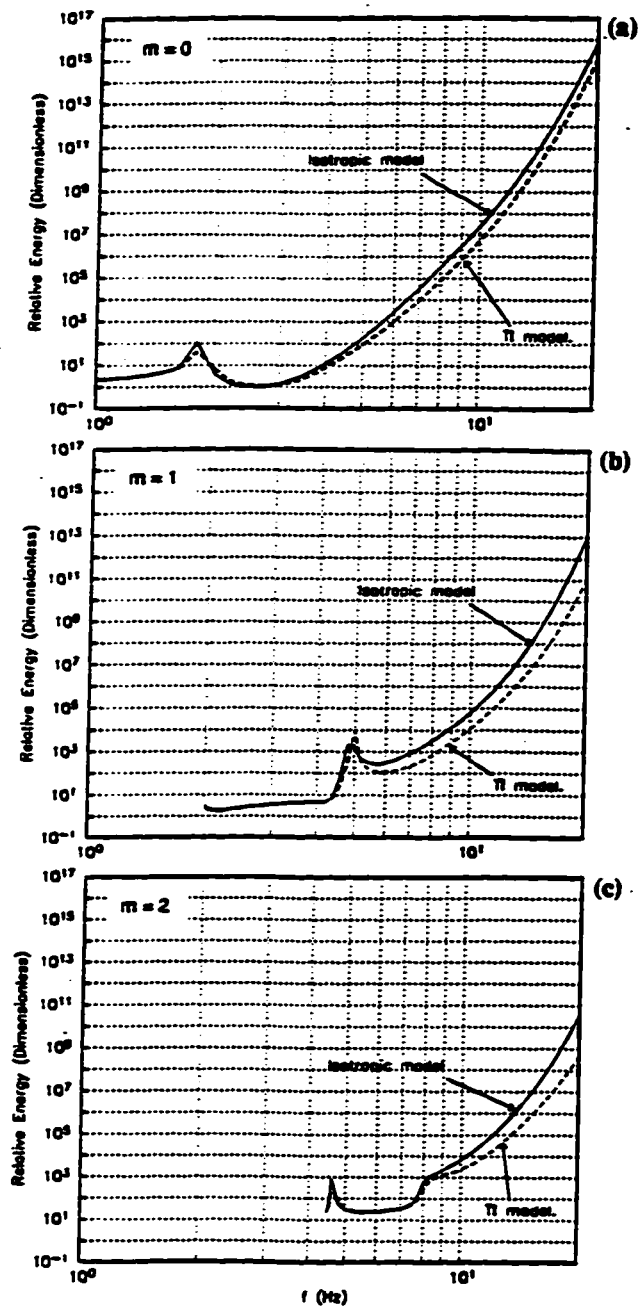
knees occur at the frequency at which a mode becomes trapped in the sediment layer. The mode dies out very rapidly in the underlying halfspace, and the phase velocity drops abruptly towards the sediment shear wave speed. The peak at 4.5 Hz in Fig. 2.6c corresponds to the very sharp minimum in the group velocity curve for $m = 2$(Fig. 2.3). At this point the group velocity rises to meet the phase velocity at the cutoff value. Our mode calculations show the increase of energy towards the Stoneley wave peak, but we did not quite reach the energy maximum in frequency. The comparisons between our model calculations and Berge et al.'s (1991) data is not direct as we have not attempted to correct our modeling results in such a way that would permit absolute amplitude comparisons with their experimental data.

2.2.4 Mode sensitivity to transverse isotropy

Berge et al. (1991) reported that their synthetic seismograms were quite sensitive to small perturbations in the elastic modulus F (c_{13} in the abbreviated subscript notation). The modulus F affects the the propagation of qP and qSV at angles intermediate between the horizontal and vertical in a TI medium with a vertical symmetry axis. In an attempt to illuminate the sensitivity of a bottom interacting acoustic signal to sediment anisotropy, we computed partial derivatives of mode energy with respect to a parameter η'.

The dimensionless partial derivative of the mode energy is defined by

$$\frac{1}{E_m}\frac{\partial E_m}{\partial \eta'} = \frac{1}{E_m}\frac{\partial F}{\partial \eta'}\frac{\partial E_m}{\partial F} = -\frac{A - 2L}{E_m}\frac{\partial E_m}{\partial F}. \qquad (2.39)$$

In Fig. 2.7 the partial derivative Eq(2.39) is plotted versus $\eta' \times 100$ for the first three modes at 10 Hz. Since a value of $\eta' = 0$ indicates isotropy, the anisotropy increases with increasing values of the abcissa. The magnitudes of the derivatives for the first three modes are relatively large and negative. The negativity of the derivatives indicates that the energy of the modes will decrease with increasing anisotropy as

measured by increasing η'. Again, we mention that the vertical component of the eigenfunctions are all normalized to have unit displacement at the surface.

Physically Fig. 2.7 illustrates that, as the elastic modulus F departs from its isotropic value, less energy is required to produce the same vertical surface displacement. (In an isotropic medium, F corresponds to the Lamé parameter λ.) Our perturbation reduces F from its isotropic value, thereby reducing the stiffness of the medium somewhat at angles intermediate between the horizontal and vertical. The effect is the same as reducing the spring constant of a mass-spring system. Less energy is required to produce a given displacement of the mass suspended from a weaker spring. The relatively large dimensionless magnitudes of the derivatives are a measure of the sensitivity of the eigenfunction, and hence the acoustic signal, to anisotropic medium perturbations. Since the fundamental has the largest derivative, it will also be most sensitive to changes in F. Although not shown in Fig. 2.7, at 10 Hz for the mode $m = 3$, $\partial E_m / \partial \eta'$ is a very weak function of η' and nearly zero. The mode $m = 3$ persists to greater depth into the bottom, and has relatively more energy both in the water column and the underlying halfspace.

We also found for this model that a 2.4% change in η' could produce a 15% change in the phase velocity of the Stoneley wave mode. Over the range of η' from 0 to 0.024, the phase velocity of the fundamental increases from 145.57 m/s to 169.67 m/s.

The frequency sensitivity of the mode energy for a single value of the anisotropy parameter $\eta' = 0.012$ is illustrated in Fig. 2.8 by a plot of $\partial E_m / \partial \eta'$ versus frequency. The main thing to notice is, that over the 4 Hz to 20 Hz frequency range depicted, the magnitude of the derivative is increasing. A shallow water signal with a strongly excited Stoneley wave will become more sensitive to the anisotropy with increasing frequency. Of course as the frequency increases still further, the excitation of the Stoneley wave will drop off, and the influence of the anisotropy on that part of the signal will also decrease.

We have not computed the corresponding partial derivatives with respect to ϕ',

Figure 2.7: Nondimensional partial derivatives of mode energy with respect to the parameter η'. The negativity of the derivatives indicates that the mode energy for the first three modes decreases upon departure from isotropy.
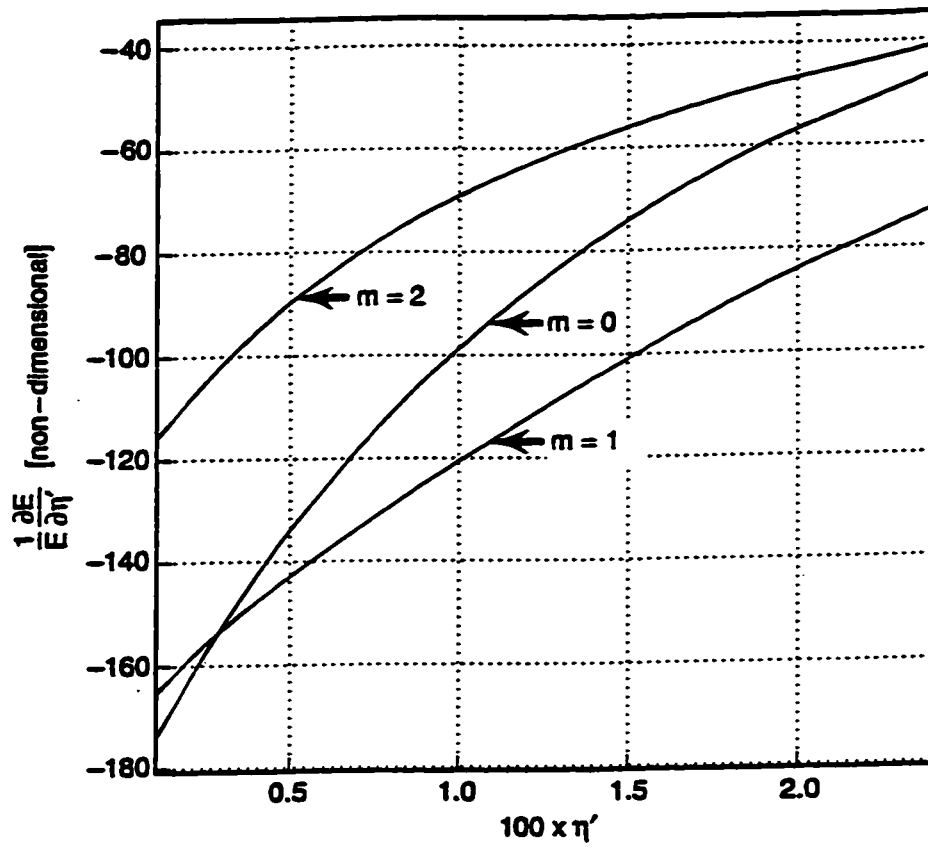
Figure 2.8: The partial derivative of the fundamental mode energy with respect to η' evaluated at $\eta' = 0.012$ as a function of frequency. Note that the absolute value of the magnitude of the derivative generally increases over the plotted frequency range. Indicating an increasing sensitivity with frequency of the fundamental mode to the anisotropy. A value of $\eta' = 0.012$ corresponds to the best fitting TI model for the long profile data of Berge et al.'s (1991) (their Table 1).

$\frac{1}{E}\frac{\partial E}{\partial \eta'}$ [non-dimensional]

-20
-30
-40
-50
-60
-70
-80
-90
-100

4   8   12   16   20

Frequency (Hz)
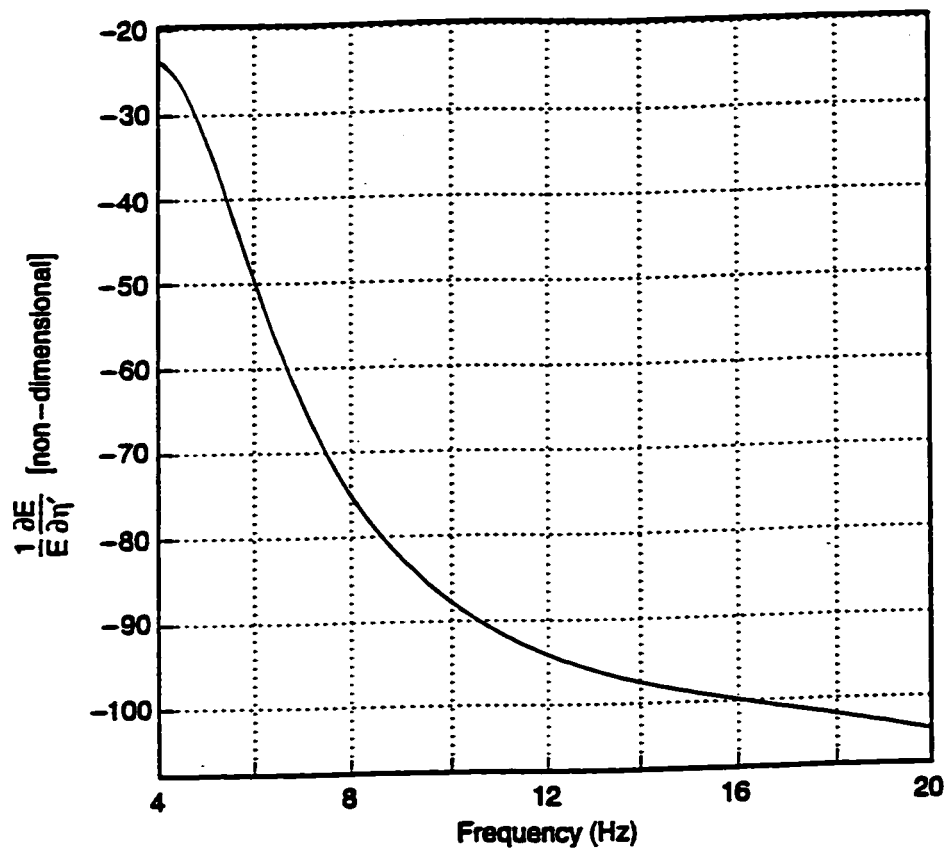
which controls the P wave anisotropy, while holding $\eta' = 0$. This combination of anisotropy parameters violates the condition expressed by Eq.(2.37), while the converse, i.e. $\phi' = 0$ and $\eta' > 0$ does not. We have, however, computed an example that shows the effect of both $\eta' > 0$ and $\phi' > 0$. As previously mentioned, Berge et al. (1991) did not investigate the effects of P-wave anisotropy because their profiles were not long enough to resolve it. The length of their long profile was about 200 m. The P-wave anisotropy could be important for longer propagation paths, since values as high as 40% have been reported in shale (1955), although 8% to 14% is probably more typical of marine sediments (Bachman 1979).

Fig. 2.9 is a plot of the vertical displacement component of the fundamental eigenfunction for the isotropic case $\eta' = 0$ and $\phi' = 0$ (solid line), and for the two transversely isotropic cases corresponding to $\eta' = 0.012$ and $\phi' = 0$ (dashed line), and $\eta' = 0.012$ and $\phi' = 0.012$ (dotted line). A value of $\eta' = 0.012$ corresponds to Berge et al.'s (1991) long profile model (their Table 1). The vertical components of the eigenfunctions are all normalized to have unit displacement at the surface. The amplitude of the fundamental for the case $\eta' = 0.012$ and $\phi' = 0.012$ lies between the the amplitude for the isotropic case and for the case $\eta' = 0.012$ and $\phi' = 0$. The inclusion of this very modest amount of P-wave anisotropy draws the appearance of the fundamental back towards isotropy. It may be possible to increase the P-wave anisotropy enough so that there is essentially no detectable difference between the shapes of the isotropic and anisotropic eigenfunctions, but, in reality the P-wave anisotropy near the water-sediment interface is likely to be even smaller than the value used for our calculations (Fryer & Miller 1986). The phase velocity of the fundamental for the case $\eta' = 0.012$ and $\phi' = 0$ is 159.83 m/s, which is actually slightly higher than the horizontally propagating qSV speed (158.26 m/s).

Figure 2.9: Vertical displacement component of the fundamental eigenfunction for the isotropic medium(solid line, phase velocity = 145.57 m/s), and for TI media characterized by $\eta' = 0.012$(dashed line, phase velocity = 159.83 m/s) and $\eta' = \phi' = 0.012$(dotted line, phase velocity = 153.73 m/s). They have all been normalized to unit displacement at $z = 0$. The frequency is 10 Hz. The speed of horizontally propagating qSV waves ($\sqrt{L/\rho}$) at the water sediment interface is 158.26 m/s.

Vertical Displacement (w_z)

η'	ϕ'	
0	0	———
0.012	0	—·—·—
0.012	0.012	- - - - -
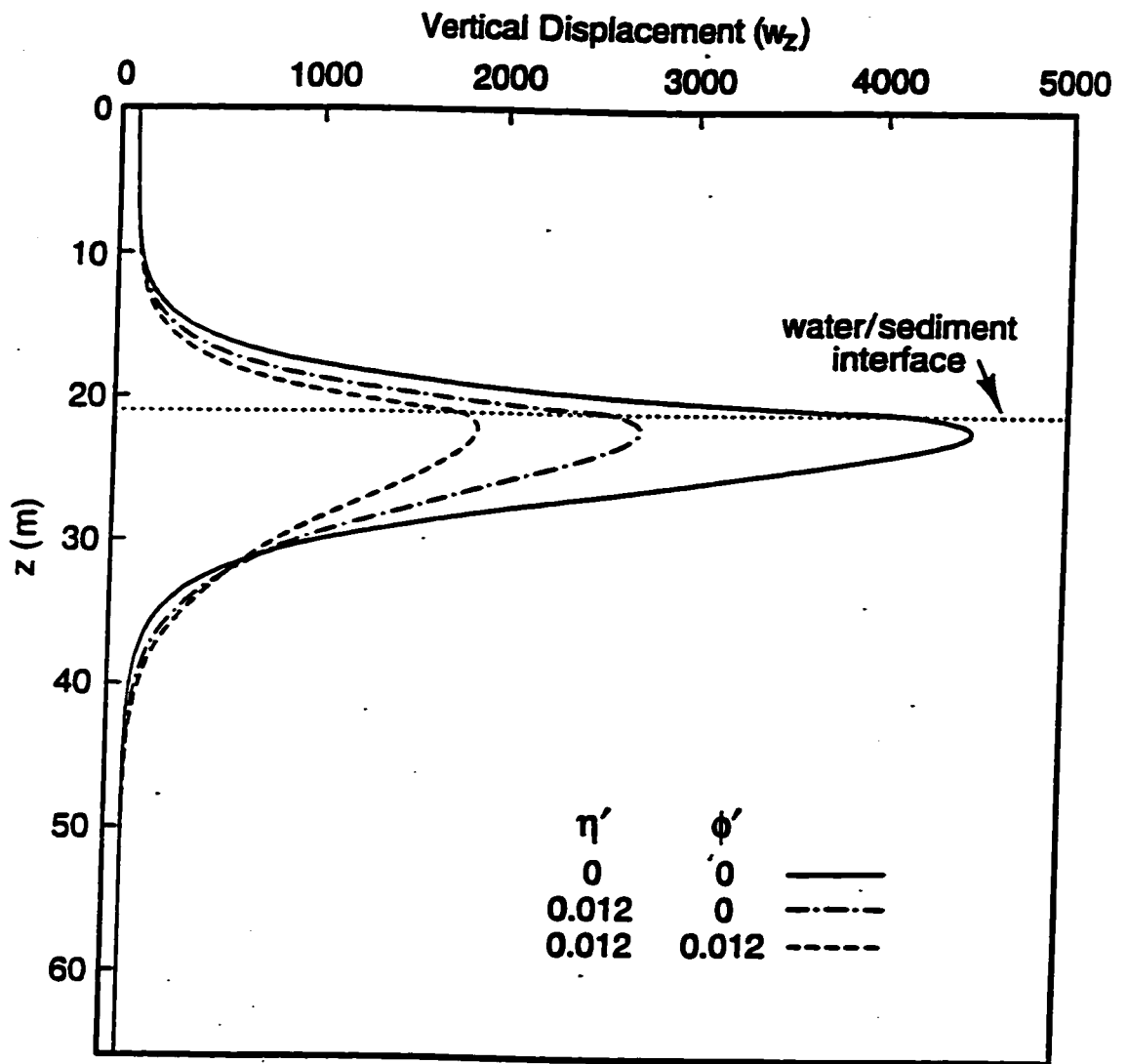
2.2.5 Medium effects on mode coupling

Our ultimate goal is to improve our ability to model and predict shallow water acoustic signal propagation in a range dependent medium. We have computed the coupling matrix B_{qr} (Eq. A.1) including the fluid-solid boundary interaction terms described in Eq.(A.2) and Eq.(A.3) for the isotropic model ($\eta' = 0$ and $\phi' = 0$) equivalent to Berge et al.'s model (Fig. 2.10a,b); for the TI model of Berge et al. (1991) ($\eta' = 0.012$ and $\phi' = 0$) (Fig. 2.10c,d); and for a model ($\eta' = 0.012$ and $\phi' = 0.012$) incorporating the weak P-wave anisotropy (Fig. 2.10e,f). The calculations were done at two frequencies 10 Hz and 20 Hz.

Berge et al.'s (1991) TI model is a range independent model. What we have computed is the coupling matrix for a model with the same local vertical structure as Berge et al. (1991). The absolute values of the coupling matrix $|B_{qr}|$ in Fig. 2.10 represent the effects of the geometric medium properties only. The layer boundary slopes, $\dot{h}_n = dh_n/dx$, have been set equal to 1. All material parameter horizontal gradients such as $\dot{\rho}$ have been set equal to 0. The absolute values of the elements of all six coupling matrices depicted in Fig. 2.10 have been normalized by dividing all elements by the largest matrix element of the entire set so comparisons can be made between frequencies and between the isotropic and both TI media. The diagonals have been intentionally left blank. Referring back to Eqs.(2.30) and (2.31), we see that the diagonals are zero.

As the frequency increases, the shallow water structure can support a greater number of modes, so there are more modes to participate in the coupling. Comparing Fig. 2.10a and Fig. 2.10b for the isotropic medium, it is clear that the coupling is stronger at 20 Hz than at 10 Hz, and that a fairly large number of modes participate almost equally in the coupling at 20 Hz. There is also fairly strong coupling among non-nearest neighbor modes for the lower order modes.

Comparing Fig. 2.10(c,d) with Fig. 2.10(a,b), it can be seen that at 10 Hz there

Figure 2.10: The absolute value of the elements of the coupling matrix B_{qr} Eq.(A.1) for the model in Fig. 2.1. Layer boundary slopes $\dot{h}$ have been set equal to 1, and all horizontal material parameter gradients such as $\dot{\rho}$ have been set to 0. This emphasizes the effects of geometric (boundary) heterogeneities. The absolute values of the elements of the six coupling matrices have been normalized by the largest matrix element of the entire set so comparisons can be made between frequencies and between isotropic and TI media. The array elements have been normalized so that dark red is unit coupling and dark blue is zero coupling. The diagonals have been purposely left blank to reflect our choice of phase for the local modes (Eq.(2.31)).

10 Hz   20 Hz
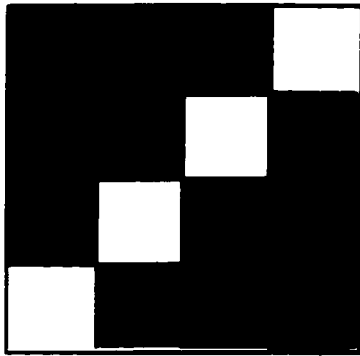
(a)   (b)

$\eta' = 0$
$\phi = 0$
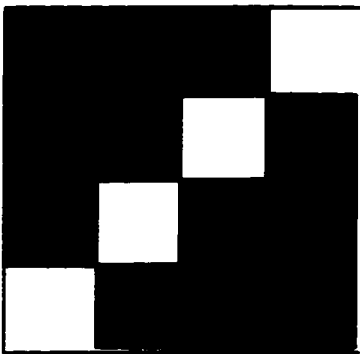
(c)   (d)

$\eta' = 0.012$
$\phi = 0$

(e)   (f)
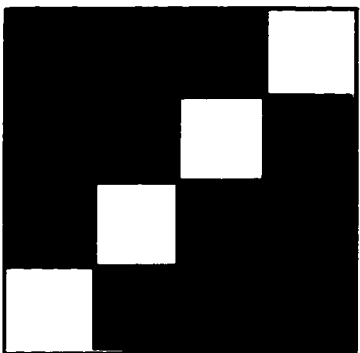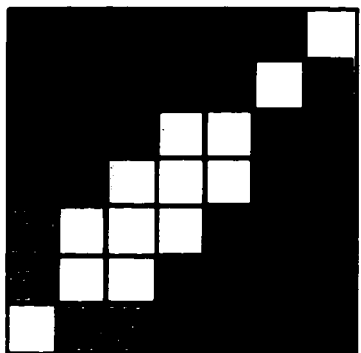
$\eta' = 0.012$
$\phi = 0.012$

0   1   2   3   0 1 2 3 4 5 6

Mode #   Mode #

0   1

is little difference between the isotropic and the TI medium, but that at 20 Hz, the differences are much greater. The coupling is confined more strongly to nearest neighbors and at 20 Hz there is a preferred mode pair {4,5} in the TI medium (Fig. 2.10d). The coupling strengths are much more uniform for the isotropic medium at 20 Hz. Coupling strength decreases away from the diagonal and also away from the preferred mode pair. This latter effect illustrates the most striking difference between the TI and isotropic media, and is a qualitative indicator of the difficulties that may be encountered by ignoring sediment anisotropy when attempting to model range dependent shallow water acoustic propagation. Away from the diagonal, other mode pairs participate nearly equally in the coupling process. This indicates that a careful examination of the coupling matrix is necessary before deciding on a truncated mode set to employ when synthesizing complete propagating signals in a range dependent medium. Use of too small a mode set will alias the coupling, and affect the amplitude and phase of a synthesized signal, but also, it may occur that coupling is confined to a small number of model configurations leading to more efficiency in calculations.

We have also computed the coupling matrix for a TI medium containing weak P-wave anisotropy in addition to the S-wave anisotropy of Berge et al.'s (1991) model (Fig. 2.10e,f). The addition of weak P-wave anisotropy to the model has only a slight effect, and Fig. 2.10(e,f) look very similar to Fig. 2.10(c,d). This is not too surprising, since the particle motion of the Stoneley wave and pseudo-Rayleigh waves that comprise the sediment modes is mostly shear motion. This explains why addition of S-wave anisotropy has a greater effect than addition of P-wave anisotropy. Also because of the almost order of magnitude difference between the shear and compressional wavelengths at the water-sediment interface, the effects of the shear wave anisotropy will accumulate much faster for a strongly bottom interacting shallow water acoustic signal.

The results shown in Fig. 2.10 are quite general, because they indicate the dependence of mode coupling on the medium properties independent of any specific

range dependent model. Fig. 2.10 represents the excitation of the modal spectrum and it's sensitivity of the excitation to any imposed range dependence. To get a complete picture of propagation in heterogeneous media, the actual range dependent structure of the medium must be imposed and the evolution equation Eq.(2.26) for the heterogeneous region must be solved.

2.3 Summary and Conclusions

We have summarized a coupled mode theory for fluid-elastic media that is formulated as a coupled set of first order equations, and accounts exactly for the inhomogeneous boundary condition due to range dependent interface irregularities (Maupin 1988). We have applied this theory to a realistic shallow water model derived from experimental data. A particular feature of this work is the inclusion of transversely isotropic bottom sediments.

Our modeling results show that there can be significant qualitative and quantitative differences between the eigenvalues and modes in shallow water models with an isotropic and a tranversely isotropic bottom. A 2.4% departure from isotropy can result in a 15% change in phase velocity for a bottom interacting mode. These differences are also reflected in the mode coupling induced by range dependence. Transversely isotropic sediments will exhibit somewhat suppressed mode coupling in comparison to the equivalent isotropic sediments. The Stoneley wave at the water sediment interface is particularly sensitive to the transverse isotropy of the sediments. Conversion to Stoneley waves has been shown to be an important loss mechanism by Hawker (1978). In light of the sensitivity of the Stoneley waves to the transverse isotropy of the bottom, and the apparent ease with which they can be excited by bottom roughness (Kuperman & Schmidt 1989), some care should be taken regarding interpretations of strongly bottom interacting acoustic signals derived from models that assume isotropic sediment properties.

Chapter 3

EFFECTS OF ELASTIC HETEROGENEITIES AND ANISOTROPY ON MODE COUPLING AND SIGNALS IN SHALLOW WATER

Coupled mode theory is applied to acoustic/elastic wave propagation in shallow water to examine the effects of lateral heterogeneities and transverse isotropy on mode coupling and signals. A numerical code is developed by applying the invariant imbedding technique to the coupled mode theory. From the code, the reflection and transmission matrices and the forward/backward propagating wavefields in the frequency domain are generated for a deterministic range-dependent medium. The effect of transverse isotropy of bottom sediment layers is also considered. Time domain signals are synthesized with a 2-Hz bandwidth between 10 Hz and 12 Hz for the excitation by a unit line force and for an incident fundamental mode. The generation of higher overtones and the decay of the fundamental mode propagating in a range dependent medium are clearly shown. First order perturbation theory is applied to the coupled mode theory to incorporate scattering from stochastic boundary roughness. The stochastic coupling matrix describing the coupling from the primary field to the scattered field, is computed. Numerical results show the strong scattering of the Scholte wave (fundamental mode) to other higher modes.

3.1 Theory

In this section, we present the method based on Maupin's (1988) coupled mode theory. First, we briefly summarized the coupled mode theory for layered fluid-elastic

media (Maupin 1988). Next, we introduce the invariant imbedding technique (IIT) as applied to coupled mode theory by Kennett (1984). The evolution equation is converted to coupled differential Riccati equations for the transmission matrix and the reflection matrix. The transmission matrix accounts for the interaction between the modes of the incident wave and those of the transmitted (or forward propagating) wave, and the reflection matrix describes the coupling to the the reflected (or backward propagating) wave. In the third subsection, we represent the source as a decomposition of local modes. In the last subsection, we apply perturbation theory to the coupled mode theory to derive the evolution equation for the secondary field scattered from a randomly rough boundary.

3.1.1 Mode coupling in deterministic range-dependent media

Because our shallow water model consists of a fluid layer over an elastic bottom, we employ the coupled mode theory based on the local mode representation, as formulated by Maupin (1988) for fluid-elastic media. Only a brief outline of the theory, required for the development in the following subsections, is therefore given in this paper. Details are given in Maupin (1988) or Odom et al. (1996). For the numerical implementation in the following section, the range-dependence is assumed to be confined in the interval $[x_L, x_R]$ as illustrated in Fig. 3.1, and the boundary conditions for the equation of motion are set according to that interval.

The particle displacement vector $\mathbf{w} = (w_x, w_y, w_z)$ is Fourier transformed with respect to y and t:

$$\mathbf{w}(x, z, k_y, \omega) = \int_{-\infty}^{+\infty} \int_{-\infty}^{+\infty} \mathbf{w}(x, y, z, t) \exp(i k_y y - i\omega t) dy dt \qquad (3.1)$$

The stress is

$$\boldsymbol{\tau} = (\ \mathbf{T}(\hat{\mathbf{x}}_1) \quad \mathbf{T}(\hat{\mathbf{x}}_2) \quad \mathbf{T}(\hat{\mathbf{x}}_3)\ ) = (\ \mathbf{t} \quad \mathbf{t}_2 \quad \mathbf{t}_3\ ), \qquad (3.2)$$

where the unit vectors of coordinates are $(\hat{\mathbf{x}}_1, \hat{\mathbf{x}}_2, \hat{\mathbf{x}}_3) = (\hat{\mathbf{x}}, \hat{\mathbf{y}}, \hat{\mathbf{z}})$ and the traction vector is $\mathbf{t}_i = (\tau_{ix}, \tau_{iy}, \tau_{iz})^T$ for $i = 1, 2, 3$. By introducing the six-component

44

Figure 3.1: The figure illustrates the geometry of the range dependent medium modeled by the coupled Riccati equations Eq.(3.31) and Eq.(3.32). The range dependent region (II) is sandwiched between two plane layered (range independent) regions (I) and (III) that need not be the same. The integration of Eq.(3.31) and Eq.(3.32) proceeds backwards from the point x_R to the point x_L.

x

z

I

II

III

x_L

x_R

$\rho^{(I)}(z),\ c^{(I)}(z)$

INCIDENT

R

$\rho^{(II)}(x,z),\ c^{(II)}(x,z)$

$\rho^{(III)}(z),\ c^{(III)}(z)$

T

$\rho^{(I)}(z)$
$C_{ij}^{(I)}(z)$

$\rho^{(II)}(x,z)$
$C_{ij}^{(II)}(x,z)$

$\rho^{(III)}(z)$
$C_{ij}^{(III)}(z)$
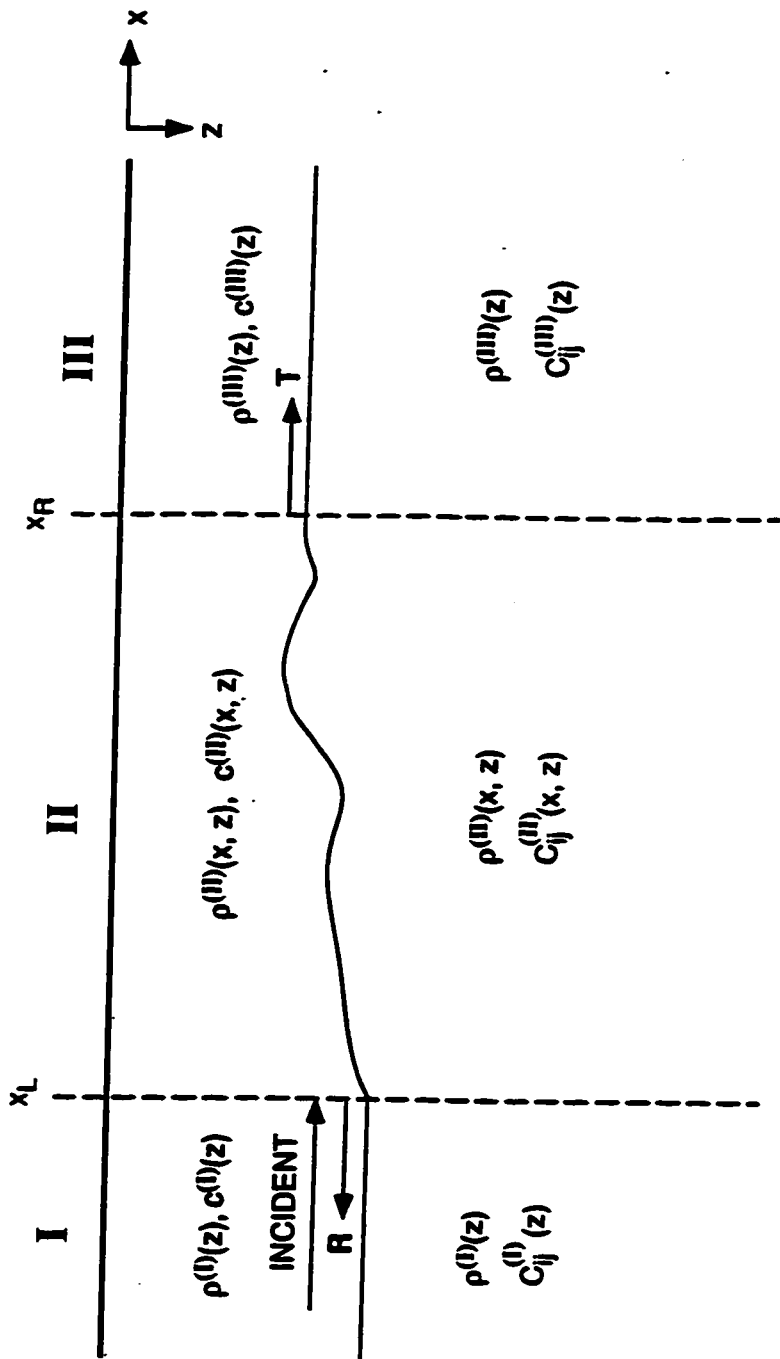
displacement-stress vector $\mathbf{u} = (\mathbf{w}, \mathbf{t})^{\mathbf{T}}$, the equation of motion and the constitutive law for elasticity can be written as the first-order system:

$$\frac{\partial \mathbf{u}}{\partial x} = A\mathbf{u} - \mathbf{F}^S + \mathbf{F}^0 \tag{3.3}$$

with the boundary conditions

$$[\mathbf{t}_3]_m = [\mathbf{w}]_m = 0, \tag{3.4}$$

where the traction vector on the vertical plane whose surface normal is $\hat{\mathbf{x}}$, $\mathbf{t} = \mathbf{t}_1 = (\tau_{xx}, \tau_{xy}, \tau_{xz})^T$ and the external source $\mathbf{F}^S$ and the effective source $\mathbf{F}^0$ resulting from non-planar boundaries are

$$\mathbf{F}^S = \left\{ \begin{array}{c} \mathbf{0} \\ \mathbf{f}^S \end{array} \right\}, \tag{3.5}$$

$$\mathbf{F}^0 = \left\{ \begin{array}{c} \mathbf{0} \\ [\mathbf{t}]_m \, \delta\,(z - h_m(x)) \end{array} \right\}. \tag{3.6}$$

The source $\mathbf{F}^0$ is a localized volume force located along the interface which is converted from a traction discontinuity at the interface by the representation theorem (Burridge & Knopoff 1964). The square brackets $[\cdot]_m$ in eq. (3.4) indicate the jump of the enclosed quantity across the mth interface, taken from bottom to top. The range coordinate, x in eq. (3.3) represents the propagation direction and the differential operator A on the r.h.s. of eq. (3.3) contains only the derivatives with respect to the depth coordinate, z. For horizontal transmission in transversely isotropic elastic media, the displacement-stress vector can be written as

$$\mathbf{u} = \left(\begin{array}{cccccc} w_x & 0 & w_z & \tau_{xx} & 0 & \tau_{xz} \end{array} \right)^T \quad \text{for Rayleigh } (P\text{-}SV) \text{ waves}, \tag{3.7}$$

$$\mathbf{u} = \left(\begin{array}{cccccc} 0 & w_y & 0 & 0 & \tau_{xy} & 0 \end{array} \right)^T \quad \text{for Love } (SH) \text{ waves}, \tag{3.8}$$

and in a fluid layer

$$\mathbf{u} = \left(\begin{array}{cccccc} \frac{1}{i\omega}V_x & 0 & 0 & p & 0 & 0 \end{array} \right)^T \quad \text{for acoustic waves}, \tag{3.9}$$

where the symbol P represents the compressional waves, SV the vertically polarized shear waves, and SH the horizontally polarized shear waves. In eq. (3.9), p is the pressure, V_x is the x-component of the velocity. The matrix differential operator A is

$$A = \begin{pmatrix} A^{11} & A^{12} \\ A^{21} & A^{22} \end{pmatrix}. \tag{3.10}$$

For a TI elastic medium, the submatrices of the differential operator A are

$$A^{11} = \begin{pmatrix} 0 & ik_y\frac{A-2N}{A} & \frac{F}{A}\frac{\partial}{\partial z} \\ ik_y & 0 & 0 \\ \frac{\partial}{\partial z} & 0 & 0 \end{pmatrix} \tag{3.11}$$

$$A^{12} = \begin{pmatrix} \frac{1}{A} & 0 & 0 \\ 0 & \frac{1}{N} & 0 \\ 0 & 0 & \frac{1}{L} \end{pmatrix} \tag{3.12}$$

$$A^{21} = \begin{pmatrix} -\rho\omega^2 & 0 & 0 \\ 0 & -\rho\omega^2 - \frac{\partial}{\partial z}\left(L\frac{\partial}{\partial z}\right) & ik_y\frac{2NF}{A}\frac{\partial}{\partial z} + \frac{\partial}{\partial z}(ik_yL) \\ 0 & ik_yL\frac{\partial}{\partial z} + \frac{\partial}{\partial z}\left(ik_y\frac{2NF}{A}\right) & -\rho\omega^2 - \frac{\partial}{\partial z}\left(\frac{AC-F^2}{A}\frac{\partial}{\partial z}\right) + k_y^2L \end{pmatrix} \tag{3.13}$$

$$A^{22} = \begin{pmatrix} 0 & ik_y & -\frac{\partial}{\partial z} \\ ik_y\frac{A-2N}{A} & 0 & 0 \\ -\frac{\partial}{\partial z}\frac{F}{A} & 0 & 0 \end{pmatrix}, \tag{3.14}$$

where the elastic parameters in a TI medium are defined for horizontal transmission as (Takeuchi & Saito 1972)

$$\sqrt{\frac{A}{\rho}} \equiv \alpha_H \qquad \text{for } P\text{-waves} \tag{3.15}$$

$$\sqrt{\frac{L}{\rho}} \equiv \beta_V \qquad \text{for } SV\text{-waves,} \tag{3.16}$$

$$\sqrt{\frac{N}{\rho}} \equiv \beta_H \qquad \text{for } SH\text{-waves,} \tag{3.17}$$

and for vertical transmission, they are given by

$$\sqrt{\frac{C}{\rho}} \equiv \alpha_V \qquad \text{for compressional waves,} \tag{3.18}$$

$$\sqrt{\frac{L}{\rho}} \;\equiv\; \beta_V \qquad \text{for shear waves.} \tag{3.19}$$

The α and β represent the compressional and shear velocities, respectively, and the subscripts H and V denote horizontal and vertical. For a fluid layer, the differential operator A is

$$A^{12} \;=\; \begin{pmatrix} \frac{1}{\omega^2}\frac{\partial}{\partial z}\left(\frac{1}{\rho}\frac{\partial}{\partial z}\right) + \eta & 0 & 0 \\ 0 & 0 & 0 \\ 0 & 0 & 0 \end{pmatrix} \tag{3.20}$$

$$A^{21} \;=\; \begin{pmatrix} -\omega^2\rho & 0 & 0 \\ 0 & 0 & 0 \\ 0 & 0 & 0 \end{pmatrix} \tag{3.21}$$

$$A^{11} \;=\; A^{22} = 0, \tag{3.22}$$

where ρ is the density and η is the compressibility such that the sound speed $c = \left(\frac{1}{\eta\rho}\right)^{\frac{1}{2}}$. In 1-D range-independent and 2-D range dependent media, the matrix differential operator A can be written in block diagonal form indicating the separation of the P-SV terms from the SH. This block diagonal form is also possible for TI media.

We represent the solution of the equation of motion (3.3) as the superposition of forward($+$) and backward($-$) propagating local modes $u^r(z; x, \pm k^r)$ multiplied by the range dependent mode amplitude $c_r(x)$, where a set of local modes at $x = x'$ are computed from the locally equivalent depth-dependent but range *independent* structure:

$$\mathbf{u} = \left\{ \begin{array}{c} \mathbf{w} \\ \mathbf{t} \end{array} \right\} = \sum_r c_r^{\pm}(x) \; \exp\left(\mp i \int_{x_s}^{x} k^r(\xi)\,d\xi \right) \left\{ \begin{array}{c} \mathbf{w}^r(z; x) \\ \mathbf{t}^r(z; x) \end{array} \right\}, \tag{3.23}$$

where $k(\zeta)$ is the local horizontal wave number, and x_s denotes the source point.

By substituting eq. (3.23) into the equation of motion (3.3), the evolution equation for the range-dependent mode amplitudes is expressed in terms of both forward($+$)

and backward(-) propagating modes (Marquering & Snieder, 1995):

$$\frac{\partial}{\partial x}\begin{pmatrix} \mathbf{c}^+(x) \\ \mathbf{c}^-(x) \end{pmatrix} = \begin{pmatrix} \mathbf{B}^{++}(x) & \mathbf{B}^{+-}(x) \\ \mathbf{B}^{-+}(x) & \mathbf{B}^{--}(x) \end{pmatrix}\begin{pmatrix} \mathbf{c}^+(x) \\ \mathbf{c}^-(x) \end{pmatrix}. \qquad (3.24)$$

with the boundary conditions

$$\mathbf{c}^+ = \mathbf{c}^0 \qquad \text{at} \qquad x = x_L \qquad\qquad (3.25)$$

$$\mathbf{c}^- = 0 \qquad \text{at} \qquad x = x_R. \qquad\qquad (3.26)$$

The matrices $\mathbf{B}^{++}$, $\mathbf{B}^{+-}$, $\mathbf{B}^{-+}$ & $\mathbf{B}^{--}$ are the $n \times n$ matrices of complex values and describe forward-to-forward, forward-to-backward, backward-to-forward and backward-to-backward coupling, respectively. The vectors $\mathbf{c}^+$ and $\mathbf{c}^-$ are $n \times 1$ column vectors, where n is the appropriate number of modes required to accurately model the signal.

3.1.2 Invariant imbedding

If we specify a geometry defined by a heterogeneous region sandwiched between two homogeneous (plane layered) regions, and assume a signal incident from the left onto the heterogeneous region, Eq.(3.24) defines a $2n \times 2n$ boundary value problem (BVP) for the amplitudes of the forward and backward propagating modes. A schematic of a range dependent medium is shown in Fig. 3.1. The boundary values are $\mathbf{c}^+(x_L)$, known at $x = x_L$ on the left side of the heterogeneous region, and $\mathbf{c}^-(x_R) = 0$ on the right side of the heterogeneous region at $x = x_R$. Stable numerical solution of the two point boundary value problem defined by eq.(3.24) and the two boundary values is problematic due to the presence of both growing and decaying mode amplitudes within the heterogeneous region. This situation is exacerbated if the heterogeneous region is extended in range. Kennett (1984) and Marquering & Snieder (1995) applied the invariant imbedding technique (IIT) to the evolution equation (3.24) and its boundary conditions (3.25) & (3.26). The main strategy of IIT is to reformulate the original BVP in terms of the associated initial value problems (IVP's) via the Riccati transformation (e.g. Dieci 1992).

The procedure (Marquering & Snieder, 1995) is to define a transmission matrix $\mathbf{T}(x_R, x_L)$ that connects the $\mathbf{c}^+(x_L)$ on the left side of the heterogeneous region with the $\mathbf{c}^+(x_R)$ on the right side of the heterogeneous region

$$\mathbf{c}^+(x_R) = \mathbf{T}(x_R, x_L)\mathbf{c}^+(x_L). \tag{3.27}$$

In addition a reflection matrix $\mathbf{R}(x_R, x_L)$ is defined that relates the backscattered component $\mathbf{c}^-(x_L)$ from the heterogeneous region to the forward propagating component $\mathbf{c}^+(x_L)$ at the left side of the heterogeneous region

$$\mathbf{c}^-(x_L) = \mathbf{R}(x_R, x_L)\mathbf{c}^+(x_L). \tag{3.28}$$

We differentiate eqs.(3.27) and (3.28) with respect to x_L

$$\frac{\partial}{\partial x_L}\mathbf{c}^+(x_L) = \frac{\partial}{\partial x_L}\mathbf{T}\mathbf{c}^+(x_L) + \mathbf{T}\frac{\partial}{\partial x_L}\mathbf{c}^+(x_L) = 0 \tag{3.29}$$

$$\frac{\partial}{\partial x_L}\mathbf{c}^-(x_L) = \frac{\partial}{\partial x_L}\mathbf{R}\mathbf{c}^+(x_L) + \mathbf{R}\frac{\partial}{\partial x_L}\mathbf{c}^+(x_L) \tag{3.30}$$

The derivatives of the amplitude vectors are replaced with their expressions from Eq.(3.24), and $\mathbf{c}^-(x_L)$ can be removed from the equation using Eq.(3.28). After removing a common factor of $\mathbf{c}^+(x_R)$, we arrive at coupled matrix differential Riccati equations (DRE) for the reflection and transmission matrices for the heterogeneous region:

$$\frac{\partial}{\partial x_L}\mathbf{R} = \mathbf{B}^{-+} + \mathbf{B}^{--}\mathbf{R} - \mathbf{R}\mathbf{B}^{++} - \mathbf{R}\mathbf{B}^{+-}\mathbf{R} \tag{3.31}$$

and

$$\frac{\partial}{\partial x_L}\mathbf{T} = -\mathbf{T}\mathbf{B}^{++} - \mathbf{T}\mathbf{B}^{+-}\mathbf{R}. \tag{3.32}$$

with the initial conditions

$$\mathbf{T}(x_R, x_R) = \mathbf{I} \quad \text{and} \quad \mathbf{R}(x_R, x_R) = \mathbf{0}. \tag{3.33}$$

$\mathbf{I}$ is the $n \times n$ identity matrix.

Now we investigate the existence and the stability of the solutions of coupled matrix DRE's (3.31) & (3.32) from the properties of the coupling matrix **B**. We can decompose the coupling matrix into the amplitude and the phase:

$$B_{qr}^{++} = \frac{1}{k^q - k^r}\hat{B}_{qr}^{++}\exp\left\{i\int_{x_s}^{x}(k^q(\xi) - k^r(\xi))\,d\xi\right\}, \tag{3.34}$$

$$B_{qr}^{+-} = \frac{1}{k^q + k^r}\hat{B}_{qr}^{+-}\exp\left\{i\int_{x_s}^{x}(k^q(\xi) + k^r(\xi))\,d\xi\right\}, \tag{3.35}$$

$$B_{qr}^{-+} = \frac{1}{-k^q - k^r}\hat{B}_{qr}^{-+}\exp\left\{i\int_{x_s}^{x}(-k^q(\xi) - k^r(\xi))\,d\xi\right\}, \tag{3.36}$$

$$B_{qr}^{--} = \frac{1}{-k^q + k^r}\hat{B}_{qr}^{--}\exp\left\{i\int_{x_s}^{x}(-k^q(\xi) + k^r(\xi))\,d\xi\right\}. \tag{3.37}$$

The amplitude $\hat{B}_{qr}$ is a function of material properties and the eigenfunctions of qth and r^{th} modes. Since the eigenfunctions of qth backward propagating mode equals that of the forward propagating mode, and the eigenwavenumber k_q is merely replaced with $-k_q$ for the backward propagating mode, the amplitude $\hat{B}$ becomes

$$\hat{B}_{qr}^{++} = \hat{B}_{qr}^{+-} = \hat{B}_{qr}^{-+} = \hat{B}_{qr}^{--} \equiv \hat{B}_{qr}, \tag{3.38}$$

From the anti-Hermicity of the coupling matrix $\hat{\mathbf{B}}$ (Maupin, 1988),

$$\left\{\mathbf{B}^{++}\right\}^{\dagger} = -\mathbf{B}^{++}, \tag{3.39}$$

$$\left\{\mathbf{B}^{+-}\right\}^{\dagger} = \mathbf{B}^{-+}, \tag{3.40}$$

$$\left\{\mathbf{B}^{--}\right\}^{\dagger} = -\mathbf{B}^{--}, \tag{3.41}$$

it can be proved that the amplitude $\hat{\mathbf{B}}$ is also anti-Hermitian, e.g.,

$$\left\{B_{qr}^{++}\right\}^{\dagger} = -\frac{1}{k^q - k^r}\hat{B}_{qr}^{\dagger}\exp\left(i\int_{x_s}^{x}(k^q(\xi) - k^r(\xi))\,d\xi\right) \tag{3.42}$$

$$-B_{qr}^{++} = \frac{1}{k^q - k^r}\hat{B}_{qr}\exp\left(i\int_{x_s}^{x}(k^q(\xi) - k^r(\xi))\,d\xi\right), \tag{3.43}$$

where $\dagger$ represents the adjoint. Therefore, by equating eq. (3.42) and eq. (3.43),

$$\hat{\mathbf{B}}^{\dagger} = -\hat{\mathbf{B}}. \tag{3.44}$$

If we assume that there is no wave propagation in the y-direction, i.e., the wavenumber $k_y = 0$, and there is no mode coupling between Rayleigh waves (P-SV) and Love waves (SH), then the elements of $\hat{\mathbf{B}}$ become pure real (see eq. (25) of Maupin, 1988) and the amplitude matrix $\hat{\mathbf{B}}$ becomes antisymmetric:

$$\hat{\mathbf{B}}^T = -\hat{\mathbf{B}}, \tag{3.45}$$

where T is the transpose. From the antisymmetry of $\mathbf{B}$, the following properties can be derived:

$$\left\{ \mathbf{B}^{--} \right\}^T = -\mathbf{B}^{++}, \tag{3.46}$$

$$\left\{ \mathbf{B}^{+-} \right\}^T = \mathbf{B}^{+-}, \tag{3.47}$$

$$\left\{ \mathbf{B}^{-+} \right\}^T = \mathbf{B}^{-+}, \tag{3.48}$$

i.e., the coupling matrix $\mathbf{B}(x)$ is the particular (pointwise) Hamiltonian (Dieci, 1992):

$$\hat{\mathbf{B}}(x) = \begin{pmatrix} \mathbf{B}^{++} & \mathbf{B}^{+-} \\ \mathbf{B}^{-+} & -\mathbf{B}^{++T} \end{pmatrix}, \tag{3.49}$$

and $\mathbf{B}^{+-T} = \mathbf{B}^{+-}$, $\mathbf{B}^{-+T} = \mathbf{B}^{-+}$. When the coupling matrix $\mathbf{B}(x)$ is the particular Hamiltonian, the DRE for the reflection matrix (3.31) becomes the *symmetric* DRE. Under the condition (3.49), all solutions of (3.31) are symmetric (Dieci 1992):

$$\left\{ \mathbf{R}(x_R, x_L) \right\}^T = \mathbf{R}(x_R, x_L), \tag{3.50}$$

and existence and monotonicity properties are guaranteed, which do not generally hold for other DRE's. The symmetry of the reflection matrix reduces the number of matrix elements to be numerically solved from N^2 to $N(N + 1)/2$. It also provides a useful check on the accuracy of computation for the test.

For numerical computation of the transmission and the reflection matrices, the DRE for the transmission matrix eq. (3.32) must be solved after the DRE for the reflection matrix eq. (3.31) is numerically integrated backward from the point X_R.

One advantage of the invariant imbedding approach is that there are built in checks on the accuracy. The reflection matrix **R** can be checked for symmetry. In addition, energy conservation demands that

$$|\mathbf{R}|^2 + |\mathbf{T}|^2 = \mathbf{I}. \tag{3.51}$$

Other numerically stable techniques for solving the coupled mode evolution equation (3.24) are Mattheij's (1985) continuous decoupling transform, employed by Evans (1986) for a range dependent fluid medium, and the very powerful Lanczos method used by Knobles (1994).

Mattheij's continuous decoupling transformation was used by Evans (1986a) to stabilize the Thomson (1950)-Haskell (1953) propagator matrix technique. The dependent variables in the Thomson-Haskell method are usually the stress and displacement, whereas the IIT takes **R** and **T** as the dependent variables. Because the two methods are solving the same boundary value problem, it is of course possible to transform one method to the other (Buchen & Ben-Hador, 1996). There are, however, significant algorithmic differences between Mattheij's stabilized Thomson-Haskell method and the IIT (Evans, 1986b). Knobles (1994) found Lanczos' method to converge rapidly, and it appear to have numerical advantages for very large problems. Although we have found the computation of the local mode bases to be the most time consuming aspect of the problem.

We have adopted the IIT because of the built in numerical checks stated above, and physical relevance of the reflection and transmission matrices **R** and **T**. These matrices are easily accessible as intermediate products at any point in the solution of the matrix Riccati equations (3.31) and (3.32).

3.1.3 Mode amplitude initial values and source representation

For our 2-D range-dependent model, a unit line source is used to represent the wave excitation. Its normal mode decomposition will be derived from the product of the

Green's function and the sources in this subsection. The general solution for a range-dependent medium is represented as an integral of a product of the Green's function for a local depth-dependent structure and the external source and the effective source excited by range-dependence. The dyadic form of the Green's function for a six-dimensional displacement-stress vector is (Park, & Odom, 1997b)

$$G_{ij}(\mathbf{r}, \mathbf{r}') = \sum_{\alpha} u_i^r(z; x, \omega) u_j^{r*}(z'; x', \omega) e^{i\left(\phi_r(x) + \frac{\pi}{2}\right)}, \tag{3.52}$$

where

$$\phi_r(x) = \int_{x_s}^{x} k^r(\xi) d\xi. \tag{3.53}$$

Following Park & Odom (1997b), the integral of the product of the Green's function (3.52) and the sources $\mathbf{F}^S$ of (3.5) and $\mathbf{F}^0$ (3.6) yields the solution for a range-dependent medium:

$$\begin{aligned}
\mathbf{u}(x, z; \omega) &= \int \sum_j G_{ij}(\mathbf{r}, \mathbf{r}') \left(F_j^S + F_j^0\right) dV', \\
&= \sum_{\alpha} c_r(x) \mathbf{u}^r(z; x, \omega) e^{i\phi_r(x)}, \tag{3.54}
\end{aligned}$$

where the range-dependent modal coefficient c_α is

$$c_\alpha(x) = \int_{x_s}^{x} < \mathbf{u}^r(z'; x'), \mathbf{F}^s > dx' + \int_{x_L}^{x} < \mathbf{u}^r(z'; x'), \mathbf{F}^0 > dx', \tag{3.55}$$

the Hermitian inner product is defined as (Maupin, 1988)

$$< \mathbf{u}, \mathbf{v} > \equiv \int_0^{\infty} \mathbf{u}^\dagger \mathbf{X} \mathbf{v} dz, \tag{3.56}$$

and the matrix $\mathbf{X}$ is

$$\mathbf{X} = \begin{pmatrix} 0 & -i \\ i & 0 \end{pmatrix} \otimes \begin{pmatrix} 1 & 0 & 0 \\ 0 & 1 & 0 \\ 0 & 0 & 1 \end{pmatrix} = \begin{pmatrix} \mathbf{0} & -i\mathbf{I} \\ i\mathbf{I} & \mathbf{0} \end{pmatrix}. \tag{3.57}$$

The initial condition on c_α is

$$
\begin{aligned}
c_r^0 &\equiv c_r(x = x_L) \\
&= \int_{x_s}^{x_L} <\mathbf{u}^r(z';x'),\mathbf{F}^s> dx' \\
&= \int_{x_s}^{x_L} \left\{ \int_0^\infty \mathbf{u}^r(z';x')\mathbf{X}\mathbf{F}^s\, dz \right\} dx' \\
&= \int_{x_s}^{x_L} \left\{ \int_0^\infty \mathbf{w}^{r*}(z';x') \cdot \mathbf{f}^s e^{i\frac{x}{2}}\, dz \right\} dx',
\end{aligned}
\tag{3.58}
$$

The initial condition on c_α (3.58) is a representation of the source in terms of the modal decomposition. For a unit line source in the spectral domain,

$$
\mathbf{f}^s(x,z,\omega) \equiv \left\{ \begin{array}{c} \mathbf{f}_x \\ \mathbf{f}_y \\ \mathbf{f}_z \end{array} \right\} \tilde{g}(\omega)\delta(x - x_s)\delta(z - z_s)
\tag{3.59}
$$

where the source time function is Fourier transformed:

$$
\tilde{g}(\omega) = \int_{-\infty}^{+\infty} g(t)exp(-i\omega t)\, dt.
\tag{3.60}
$$

The representation of the source becomes

$$
c_r^0 = i\left\{w_x^r(z_s;x_s,\omega)f_x + w_z^r(z_s;x_s,\omega)f_z\right\}\tilde{g}(\omega) \qquad \text{for Rayleigh waves,} \tag{3.61}
$$

$$
c_r^0 = iw_y^r(z_s;x_s,\omega)f_y\,\tilde{g}(\omega) \qquad \text{for Love waves,} \tag{3.62}
$$

$$
c_r^0 = \frac{1}{\omega}V_x^r(z_s;x_s,\omega)f_x\,\tilde{g}(\omega) \qquad \text{for acoustic waves,} \tag{3.63}
$$

3.1.4 Stochastic mode coupling due to boundary roughness

In this subsection, we consider the problem of acoustic and elastic wave scattering from a stochastic rough boundary like the seabed. We assume a rough surface to be described in terms of its deviation from a smooth reference surface (see Fig. 3.2). The interface depth $h(x)$ is partitioned into a deterministic part and a small stochastic part (DeSanto & Brown, 1985):

$$
h(x) \equiv \langle h(x)\rangle_E + \varepsilon\gamma(x),
\tag{3.64}
$$

Figure 3.2: Schematic representation of the true boundary and the mean boundary. $\hat{N}$ is the normal vector to the true boundary and $\hat{N}_0$ is the normal vector to the mean boundary.
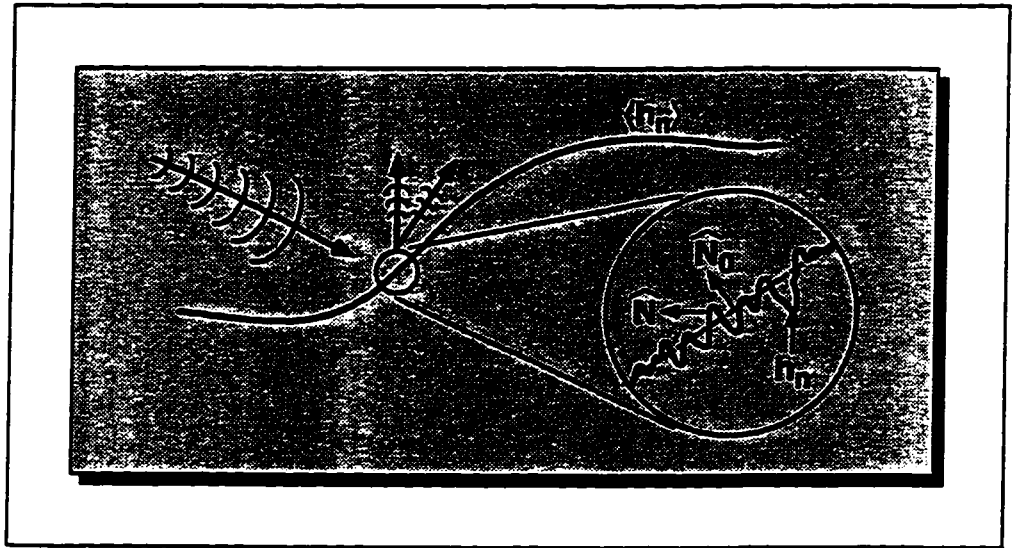
where $\langle...\rangle_E$ indicates the ensemble average over all possible realizations and $\varepsilon(\ll 1)$ is a relative amplitude. The stochastic process, $\gamma(x)$, are defined as a zero-mean process:

$$\langle\gamma\rangle_E = 0, \tag{3.65}$$

and the normalized autocorrelation function is defined as

$$N(|\xi - \eta|) = \frac{\langle\gamma(\xi)\gamma(\eta)\rangle_E}{\langle\gamma^2\rangle_E} \tag{3.66}$$

where $\langle\gamma(\xi)\gamma(\eta)\rangle_E$ is the covariance function and $<\gamma^2>_E$ is the variance of $\gamma(x)$.

We look for a solution of the equations of motion in the form of an expansion in power of ε (Sobczyk, 1984):

$$\mathbf{u}(x,z) = \mathbf{u}_0(x,z) + \varepsilon\mathbf{u}_1(x,z) + \varepsilon^2\mathbf{u}_2(x,z) + ... \tag{3.67}$$

We employ the 1st order perturbation of the coupled mode method of Park & Odom (1997b). Substituting eq. (3.67) into the equation of motion (3.3) and the boundary condition (3.4) and applying 1st order perturbation theory to both the equations of motion and the effective source converted from the jump in the boundary condition yields

$$\mathcal{O}(1) \quad : \quad \frac{\partial\mathbf{u}_0}{\partial x} = \mathbf{A}\mathbf{u}_0 + \mathbf{F}^s + \mathbf{F}^0, \tag{3.68}$$
$$[\mathbf{T}_0(\hat{z})]_n = 0,$$

$$\mathcal{O}(\varepsilon) \quad : \quad \frac{\partial\mathbf{u}_1}{\partial x} = \mathbf{A}\mathbf{u}_1 + \mathbf{F}^1, \tag{3.69}$$
$$[\mathbf{T}_1(\hat{z})]_n = 0,$$

where the sources $\mathbf{F}^0 = (0, \mathbf{f}^0)^T$ and $\mathbf{F}^1 = (0, \mathbf{f}^1)^T$ are

$$\mathbf{f}^0 = \sum_n \langle\dot{h}_n\rangle_E [\mathbf{T}_0(\dot{x})]_n \delta(z - \langle h_n\rangle_E), \tag{3.70}$$

$$\mathbf{f}^1 = \sum_n \langle\dot{h}_n\rangle_E [\mathbf{T}_1(\dot{x})]_n + \gamma_n\frac{\partial}{\partial N_o}\left[\mathbf{T}_0(\hat{\mathbf{N}}_o)\right]_n \delta(z - \langle h_n\rangle_E). \tag{3.71}$$

The 0th order system (3.68) describes propagation in a deterministic range-dependent medium with the mean structure. We refer to the 0th order solution u_0 as *the primary field*, i.e., the field when there is no random boundary perturbation in the reference medium. The effective source $\mathbf{F}^1$ in the 1st order system (3.69) consists of two terms. The first term represents the effect of the slope of the mean boundary on the 1st order solution u_1, and the second term describes the excitation of the 1st order solution of the wavefield due to the scattering of the the primary field by rough surfaces. We refer to the 1st order solution u_1 as *the scattered field*.

The equations of motion for the primary field (3.68) and for the scattered field (3.69) have the same form but the source terms are different. We can express the solution of the scattered field as an integration of a product of the 1st order body-force equivalent $\mathbf{F}^1$ and the Green's function for the primary field. Therefore, as in eq. (3.23), the displacement vector for the scattered field u_1 is also represented as a sum of local modes with stochastic mode amplitude $d_r(x)$ (Park & Odom, 1997b):

$$\mathbf{u}_1(x,z) = \sum_r d_r^{\pm}(x) \, \exp\left(\mp i \int_{x_s}^{x} k^r(\xi)d\xi\right) \left\{ \begin{array}{c} \mathbf{w}^r(z;x) \\ \mathbf{t}^r(z;x) \end{array} \right\}. \qquad (3.72)$$

The evolution equation for the stochastic mode amplitude $d_r(x)$ can be derived in the same fashion as the deterministic mode amplitude $c_r(x)$:

$$\frac{\partial d_q}{\partial x} = \sum_r B_{qr}d_r + \sum_r S_{qr}c_r, \qquad (3.73)$$

where the matrix S_{qr} is defined as

$$S_{qr} = D_{qr} + \sum_s E_{qs}B_{sr}. \qquad (3.74)$$

The coupling matrix B_{qr} in the eq. (3.73) has the same form as eq. (3.24), and similarly, it governs the mode coupling between the scattered field due to the deterministic range-dependence. The matrix S_{qr} describes the mode coupling from the primary field u_0 to the scattered field u_1 due to the boundary roughness, i.e., surface

scattering from u_0 to u_1. We refer to S_{qr} as the 1st order stochastic coupling matrix. To more clearly illustrate the origin of the stochastic (incoherent) part of the wavefield, we rewrite the evolution equation (3.73) as

$$\frac{\partial d_q}{\partial x} - \sum_r B_{qr} d_r = \sum_r S_{qr} c_r. \tag{3.75}$$

The term on the r.h.s. of eq. (3.75) is the source of the stochastic part of the field. We can therefore interpret the term $\sum_r S_{qr} c_r$ as the stochastic effective source. The matrices D and E for Rayleigh waves in a transversely isotropic medium are calculated in the Appendix.

3.2 Numerical Results

In this section we study the effect of the transverse isotropy, and the range dependence on the coupling matrix, the transmission matrix, the reflection matrix, the forward propagating and the backward propagating wavefields in the frequency domain, and the synthetic signals for a range-dependent shallow model. We also examine the effect of the boundary roughness on the stochastic coupling matrix. The code DISPER80 (Saito, 1988) is used to generate the eigenfunctions of the local modes, from which the coupling matrix B_{qr} is computed. By numerically integrating the coupled DRE eqs. (3.31) and (3.32), the transmission matrix T and the reflection matrix R are computed for a given frequency. The forward propagating and the backward propagating wavefields in the frequency domain are generated from the the matrices T and R. Signals in the time domain are synthesized from the inverse Fourier transformation of the spectral wavefield. The stochastic coupling matrix is also computed.

The computation were carried out on a Sun SPARC station LX. The numerical process consists of four steps. The first step is calculating the eigenfunctions of the local modes for each point in range at one fixed frequency. The eigenfunctions for a set of local modes for our test problem require 2.6 Mbyte disk storage when only the first four modes are computed. A disk space problem may be encountered when generating

multiple modes at multiple frequencies. This problem can be overcome because the eigenfunctions are no longer necessary after computing the transmission/reflection matrices at a particular frequency. That is, all local normal modes, except at the receiver point and the source point, can be deleted at the end of the first step. For our computational model (Fig. 3.3), it takes 20 seconds of cpu time to compute a set of four eigenfunctions at a single range point for one frequency using double precision. We found that at higher frequencies (20 Hz) for our low shear speed model, quadruple precision was necessary to generate accurate eigenfunctions. This significantly increased the computation time. At the second step, the coupling matrix B is computed from the eigenfunctions. The reflection/transmission matrices R & T are computed by numerical integration of the coupled DRE, which takes 143 seconds cpu time for one frequency for our test model. Next, the wavefields in the frequency domain are generated from the matrices R and T. As the last step, the signals in the time domain are synthesized by inverse Fourier transforming the wavefields generated for multiple frequency points. The third and the fourth steps take relatively less cpu time than the first and the second steps.

3.2.1 Computational model

Our computational model consists of a heterogeneous region ($0 \text{ m} \leq x \leq 76 \text{ m}$) and two homogeneous (plane layered) regions ($x < 0 \text{ m}$) and ($x > 76 \text{ m}$). The slope of the interfaces in the heterogeneous region varies up to $45°$, and the material properties in each layer are assumed constant. All of the numerical results are computed from the deterministic model except the stochastic coupling matrix in the last subsection. The material properties of the homogeneous region ($x > 76 \text{ m}$) are the same as the model of Odom et al. (1996) which was taken from Berge et al. (1991). The model structure, the velocity and the density profiles are illustrated in Fig. 3.3. The model consists of an isovelocity water layer over sediment layers followed by the hard bottom. The thickness of a water layer varies from 44 m to 20 m as x increases from 0 m to 76

m. The sediment layers are made of 12.5 m thick TI upper layers, followed by 12.5 m thick isotropic lower layers. There is a large contrast in the velocities and the density between the sediments and a hard bottom. The TI layer is characterized by $\eta' = 0.012$ and $\phi' = 0$, where the dimensionless parameters (Takeuchi & Saito 1972) are:

$$\eta' = 1 - \eta = 1 - \frac{F}{A - 2L}, \tag{3.76}$$

and

$$\phi' = 1 - \phi = 1 - \frac{C}{A}, \tag{3.77}$$

Values of

$$\eta' = 0 \quad \text{and} \quad \phi' = 0 \tag{3.78}$$

indicate isotropy. The departure from isotropy increases as η' and/or ϕ' change from 0. In Fig. 3.3, the vertical displacement eigenfunction of the first four local modes are plotted against depth at 10 Hz. The first mode, whose phase velocity is 145.6 m/s, propagates along the water/sediment interface, i.e., a Stoneley wave (Scholte wave). The energy of the second and the third modes are mainly confined within the sediment layers, while the fourth mode radiates into the hard bottom.

The coupling matrix **B** is computed from the eigenwavenumbers and eigenfunctions of the local modes. These coupling matrices become the coefficient matrices of the coupled matrix DRE which will be solved in the following subsection. The plots of **B** are presented in Odom et al. (1996).

3.2.2 Reflection and transmission matrices and forward and backward propagating wavefields

In this subsection, we describe the numerical solution of the matrix DRE's eqs. (3.31) and (3.32). We solved for the reflection and transmission matrices with FORTRAN code written for the direct numerical integration of complex matrix DRE's. The code

Figure 3.3: The range-dependent shallow water model with transversely isotropic sediments (based on the data of Berge et al. (1991) **Table 1.**). (a) Normal modes of an isotropic medium (solid lines) and a TI medium (dotted lines) at $x = 0$ m. (b) Density (solid line), compressional wave velocity (broken line), and shear wave velocity (dotted line) at $x = 0$ m. (c) Two-dimensional shallow water structure. ◇ indicates the point where local normal modes are computed. (d) Normal modes of an isotropic medium at $x = 76$ m.

(d)

(c)

(b)

(a)
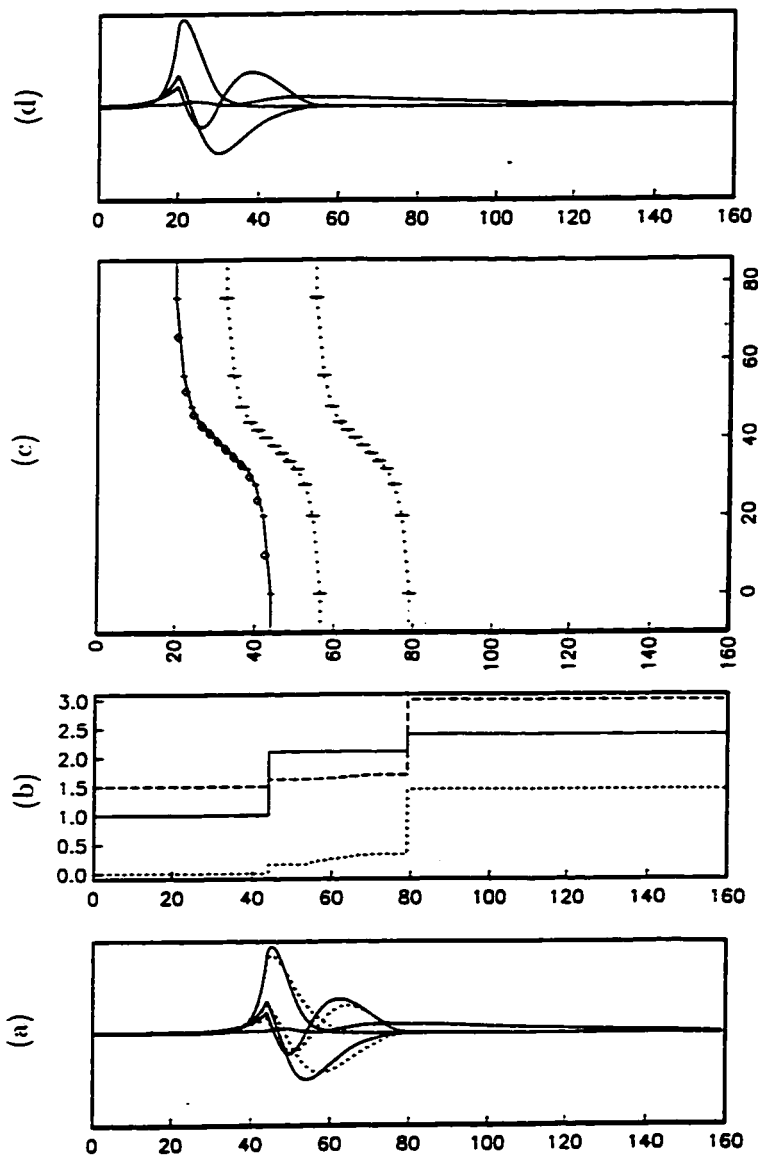
is built around a module CDRIV2 from the SLATEC library, which solves the initial value problem for systems of first order ordinary differential equations (Gear, 1971).

First, the matrix DRE (3.31) for the reflection matrix **R** is numerically integrated backward from $x_R = 76\,m$ to $x_L = 0\,m$ with the initial value (3.33) at x_R. From the computed coupling matrices and reflection matrix, the matrix DRE (3.32) is similarly solved for the transmission matrix **T**.

From the transmission and the reflection matrices, the range-dependent mode amplitudes $c_q^+(x_r)$ and $c_q^-(x_r)$ at the receiver point ($\mathbf{r} = \mathbf{r}_r$) are computed by the relations (3.27) & (3.28) and the initial values c_q^0 of (3.58):

$$c_q^+(x_r) = \sum_r T_{qr}(x_R, x_L) c_r^0 = \sum_r T_{qr}(x_R, x_L) \left\{ i\mathbf{w}^{r*}(z_s; x_s) \cdot \mathbf{f}^s \right\}, \qquad (3.79)$$

$$c_q^-(x_r) = \sum_r R_{qr}(x_R, x_L) c_r^0 = \sum_r R_{qr}(x_R, x_L) \left\{ i\mathbf{w}^{r*}(z_s; x_s) \cdot \mathbf{f}^s \right\}, \qquad (3.80)$$

where the source $\mathbf{f}^s$ is assumed to be located at the point $\mathbf{r} = \mathbf{r}_s = (x_s, 0, z_s)$ and the receiver point and the source point are assumed to be placed outside the heterogeneous region, i.e., $x_s \le x_R < x_L \le x_r$. Then the spectral wavefields at the receiver point are generated as a function of depth with a given frequency:

$$\mathbf{u}^+(z; x_r, \omega) = \sum_q g(k_q R) c_q^+(x_r) \mathbf{u}^q(z) \exp\left(-i \int_{x_s}^{x_r} k^q(\xi)\, d\xi \right)$$

$$= \sum_{q,r} g(k_q R) T_{qr}(x_R, x_L) \left\{ i\mathbf{w}^{r*}(z_s; x_s) \cdot \mathbf{f}^s \right\} \mathbf{u}^q(z)$$

$$\times \exp\left(-i \int_{x_s}^{x_r} k^q(\xi)\, d\xi \right), \qquad (3.81)$$

$$\mathbf{u}^-(z; x_r, \omega) = \sum_q g(k_q R) c_q^-(x_r) \mathbf{u}^q(z) \exp\left(i \int_{x_s}^{x_r} k^q(\xi)\, d\xi \right)$$

$$= \sum_{q,r} g(k_q R) R_{qr}(x_R, x_L) \left\{ i\mathbf{w}^{r*}(z_s; x_s) \cdot \mathbf{f}^s \right\} \mathbf{u}^q(z)$$

$$\times \exp\left(i \int_{x_s}^{x_r} k^q(\xi)\, d\xi \right), \qquad (3.82)$$

where $g(R)$ represents geometric spreading function (Aki & Richards 1980):

$$g(k_q R) = \sqrt{\frac{2}{\pi k_q R}} = \sqrt{\frac{2}{\pi k_q (x_r - x_s)}}. \qquad (3.83)$$

The computed reflection matrices are shown in Fig. 3.4 for both an isotropic model and a TI model. In the case of an isotropic model, the most prominent elements are R_{23} or R_{32}, which describe mode coupling from c_2^+ to c_3^- or from c_3^+ to c_2^-. Those two modes, the 2nd and the 3rd modes, propagate just above the sediment-basement boundary, which has a large impedance contrast. The large impedance contrast, and relatively high amplitude of the 2nd and 3rd modes at the sediment-basement interface result in the strong coupling produced by the rising basement.

Addition of transverse isotropy to sediments suppresses the reflected energy of all the elements R_{qr} for $q \, \& \, r = 1, 2, 3, 4$. The greater material stiffness for horizontally propagating waves in the TI medium generally reduces the amplitude of the low-order TI modes, $\{c_1^+, c_2^+, c_3^+, c_4^+\}$, whose energy mostly propagates in the sediments, more than the higher modes (Odom et al. 1996). The element R_{44} therefore becomes relatively stronger. As the fractional amount of modal energy in sediments decreases, the reflection from the range dependence in sediment layers also decreases.

Fig. 3.5 shows the transmission matrices for both an isotropic and a TI model. The diagonal terms of the transmission matrices, which describe the self-coupling of modes, are much stronger than the off-diagonal terms. Especially T_{44} (coupling from c_4^+ to c_4^+) is stronger, which means that the fourth mode is transmitted through the heterogeneous region almost without disturbance. That is because the fourth mode mostly propagates in the homogeneous hard bottom, which is placed below the heterogeneous sediments. The T_{23} and T_{32} elements indicate coupling between c_2^+ and c_3^+ for the same reason that R_{23} or R_{32} are strong.

The computed reflection matrix $\mathbf{R}$ is symmetric to machine precision as demanded by eq. (3.51). In addition, the off-diagonal terms of $|\mathbf{R}|^2 + |\mathbf{T}|^2$ are on the order of 10^{-5} as required by energy conservation.

The generated wavefields at 10 Hz are presented for the two cases when the incident wave is a fundamental mode (Fig. 3.6) and when the excitation is a unit line force (Fig. 3.7) for both an isotropic model and a TI model. In Fig. 3.6, the shape

Figure 3.4: The reflection matrices computed at 10 Hz for (a) an isotropic model and (b) a TI model. The real parts are plotted. Columns and rows represent incident modes and outgoing modes respectively.

(a) R, ISO
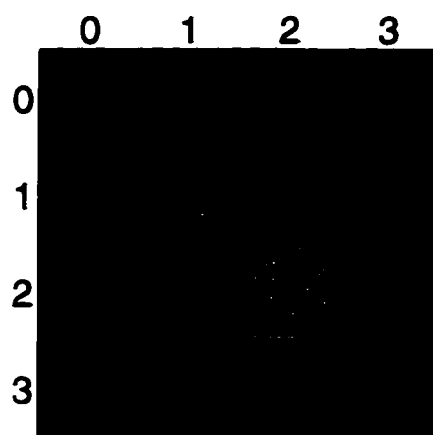
(b) R, TI

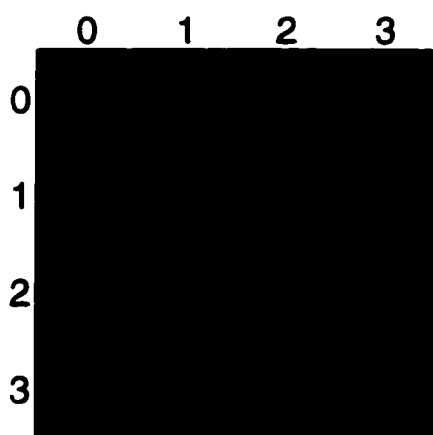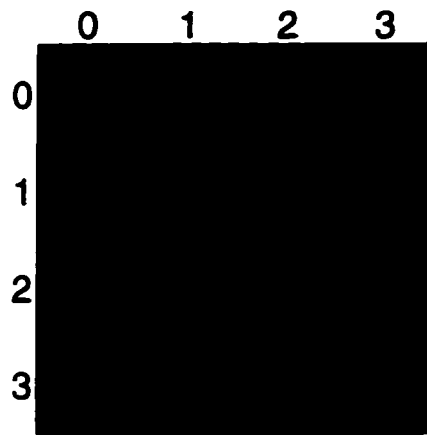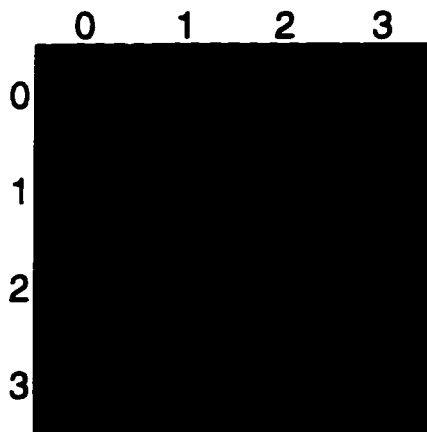Figure 3.5: The transmission matrices computed at 10 Hz for (a) an isotropic model and (b) a TI model. The real parts are plotted. Columns and rows represent incident modes and outgoing modes respectively.

(a) T, ISO

(b) T, TI

of the wavefield in an isotropic model is changed from the fundamental mode form to the oscillating form indicative of mixed modes after the transmission. This indicates that some amount of the fundamental mode energy is converted to the higher modes after transmission. The energy is spread over a greater depth range. The incident Stoneley wave along the water sediment interface is partly converted to higher order modes propagating in the sediment. For a TI model the effect of the lateral heterogeneity on the transmitted wavefield is less than for the equivalent isotropic model. For both cases the conversion to backward propagating waves is quite small. (Note that the backward propagating wavefield in Fig. 3.6 (a) and (b) have been multiplied by a factor of 10.)

The spectral wavefields are also generated for the excitation by a unit line force, which shows more complicated coupling among all four modes (Fig. 3.7)

3.2.3 Synthetic signals

Signals in the time domain are synthesized by inverse Fourier transforming the spectral wavefields

$$\mathbf{u}^+(t; x_r, z_r) = \int_{-\infty}^{\infty} \mathbf{u}^+(z; x_r, \omega)\, \delta(z - z_r) \exp(i\omega t)\, d\omega. \tag{3.84}$$

For that purpose, the spectral wavefields are generated at from 10 Hz to 12 Hz with 0.2 Hz increments. The time domain signals are 5 seconds long with a 2-Hz bandwidth between 10 Hz and 12 Hz.

Spectra with such a narrow bandwidth exhibit significant sidelobs in the time domain. To suppress the sidelobs and to generate realistic signals, a Hanning window is applied to the spectra before the transformation.

In Fig. 3.8, the arrival preceding the fundamental mode appears after transmission through the range-dependent region, which clearly indicates the mode coupling from the fundamental mode to higher modes with higher group velocities. Synthetic signals for the excitation by a unit line force show both mode coupling and dispersion of

Figure 3.6: The vertical components of the displacement wavefield are generated for an isotropic model and for a TI model when incident wave is a fundamental mode. The solid line is used for the incident wave $w_z^+(z; x = x_L, f = 10\,Hz)$, the broken line for the forward-propagating wave $w_z^+(z; x = x_R, f = 10\,Hz)$, and the dotted line the backward-propagating wave $w_z^-(z; x = x_L, f = 10\,Hz)$. The backward-propagating waves are ten times magnified for comparison.

(a) Isotropic Model
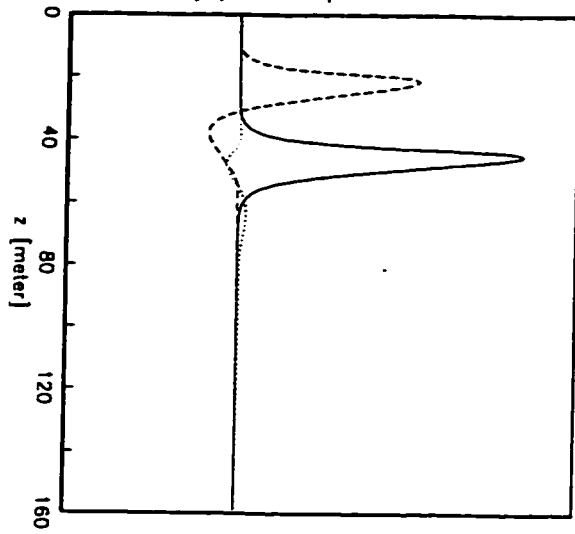
(b) TI Model
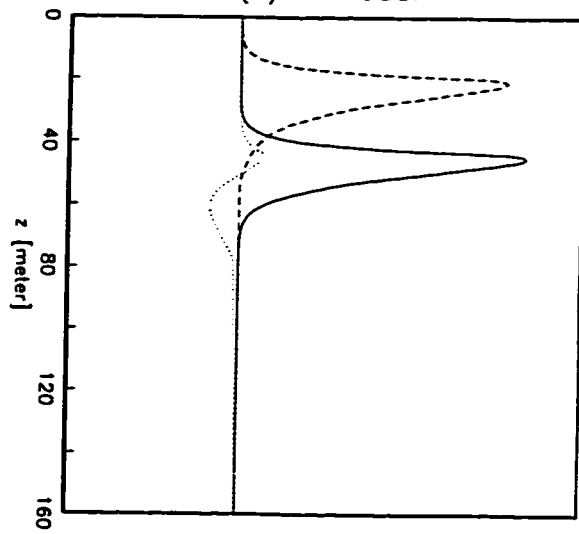
Figure 3.7: Same as Fig. 3.6 except that excitation is a unit line force.

(a) Isotropic Model

z [meter]

(b) TI Model

z [meter]
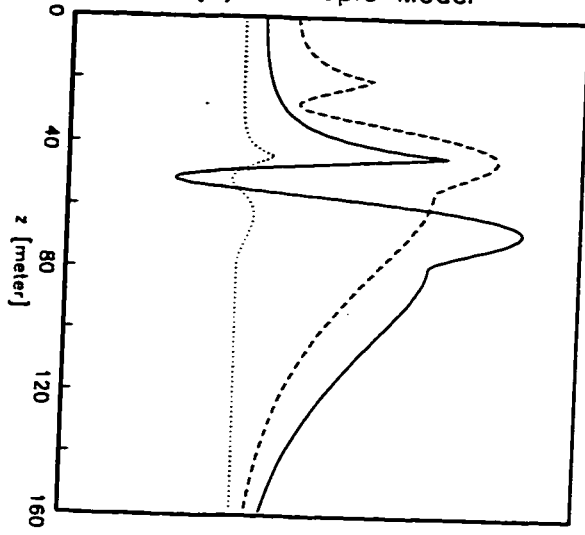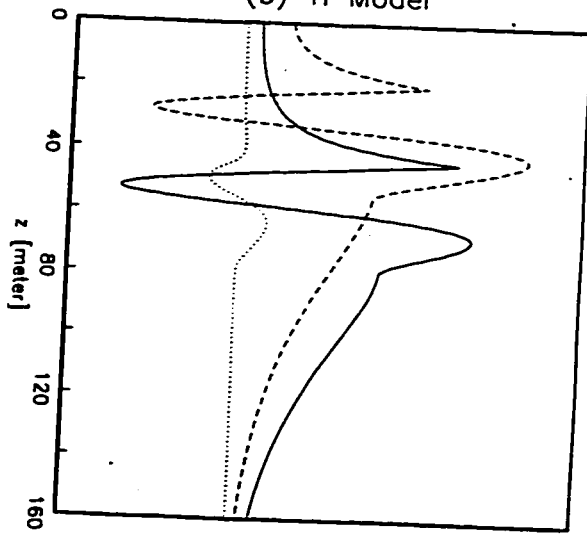
modes (Fig. 3.9). Due to mode coupling among the multiple local modes, the shape of the signals becomes very complicated after transmission through the range-dependent zone and the presence of propagation induced dispersion, and it is much more difficult to interpret those signals.

3.2.4 Stochastic coupling matrix

To illustrate the effects of randomly rough interfaces on the mode coupling, we assume that the stochastic coupling matrix S can be decomposed into a product of the deterministic part $\hat{S}$ and the stochastic process $\gamma(x)$:

$$S = \gamma(x)\hat{S} \qquad (3.85)$$

By adopting this decomposition, we have assumed that all boundaries have the same statistics. If this were not the case, the decomposition given by eq.(3.85) could not be carried out. We should compute the mean square of the stochastic coupling matrix $\langle S^2 \rangle_E$ to include the effect of multiple rough boundaries with different statistics. The matrix $\hat{S}$ is deterministic and contains the effects of the material properties and the local normal modes.

The deterministic part $\hat{S}$ of the stochastic coupling matrices S for rough surface scattering are presented in Fig. 3.10. The columns and the rows of the plot of the matrix $\hat{S}$ represent the primary field modes and the scattered field modes, respectively. The first column, $\hat{S}_{1r}$ for $r = 1, \cdots, 4$, is much stronger than the other columns. The elements $\hat{S}_{1r}$ describe the stochastic mode coupling from c_1^+ to d_1, d_2, d_3 & d_4. The Stoneley wave (the first mode c_1^+) is particularly strongly affected by rough boundaries because it is confined to the vicinity of the interface. There is significant scattering from the Stoneley wave to higher order modes due to interaction with the rough surface.

Figure 3.8: Synthetic signals (a) at $(x, z) = (0\,\text{m}, 40\,\text{m})$ and (b) at $(x, z) =$ $(800\,\text{m}, 20\,\text{m})$ with a 2 Hz bandwidth between 10 Hz and 12 Hz when incident wave is fundamental mode.

(a) Signals at x = 0 m

t [second]

(b) Signals at x = 800 m

t [second]
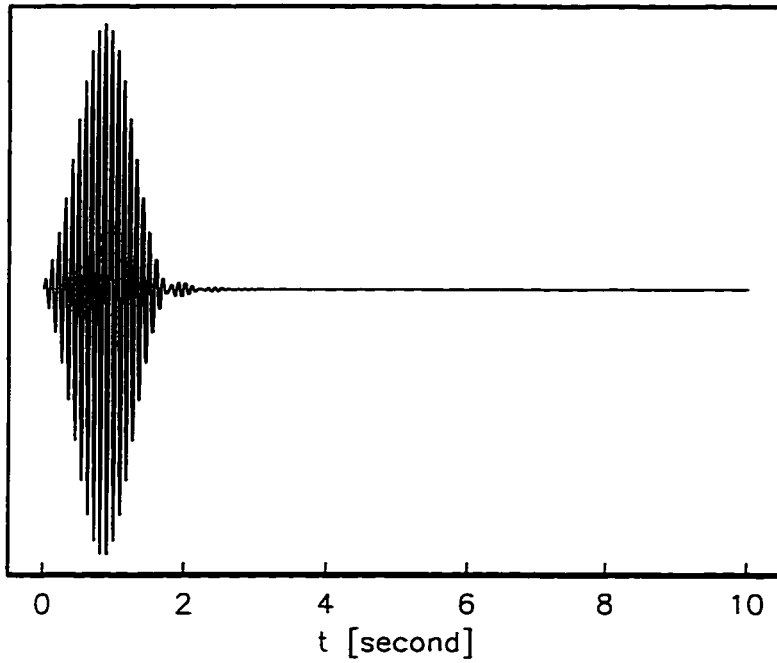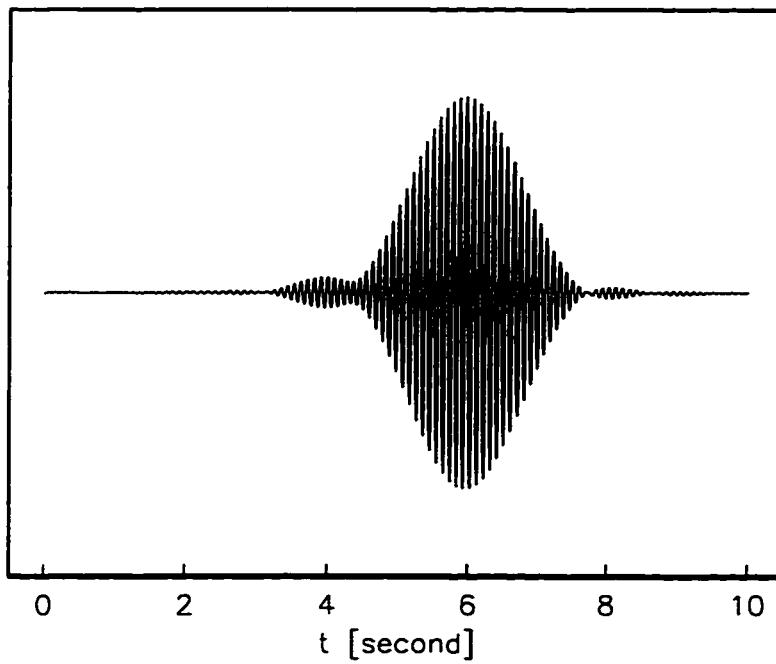
Figure 3.9: Synthetic signals (a) at $(x, z) = (0\,\mathrm{m}, 40\,\mathrm{m})$ and (b) at $(x, z) = (500\,\mathrm{m}, 20\,\mathrm{m})$ with a 2 Hz bandwidth between 10 Hz and 12 Hz when a unit line force is excited at $(x, z) = (0\,\mathrm{m}, 20\,\mathrm{m})$ in water.

(a) Signals at x = 0 m

t [second]

(b) Signals at x = 500 m

t [second]
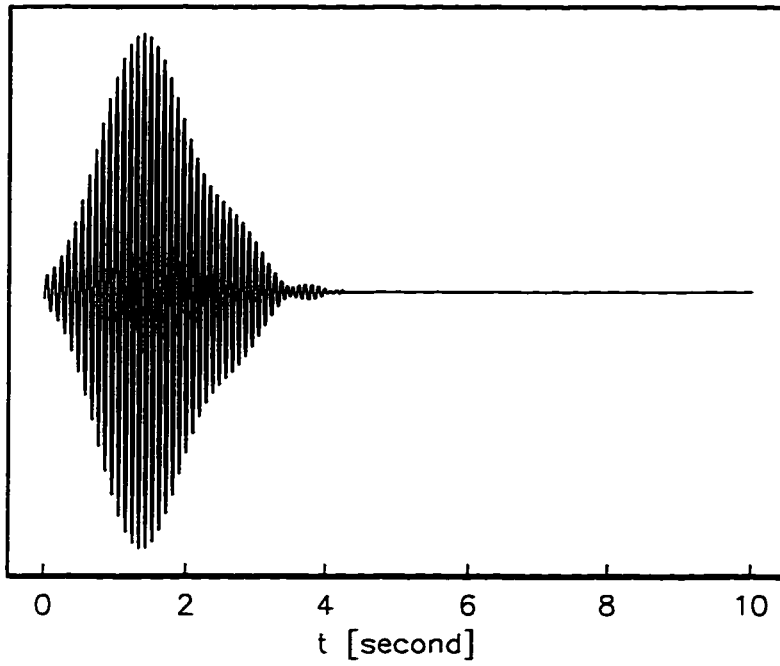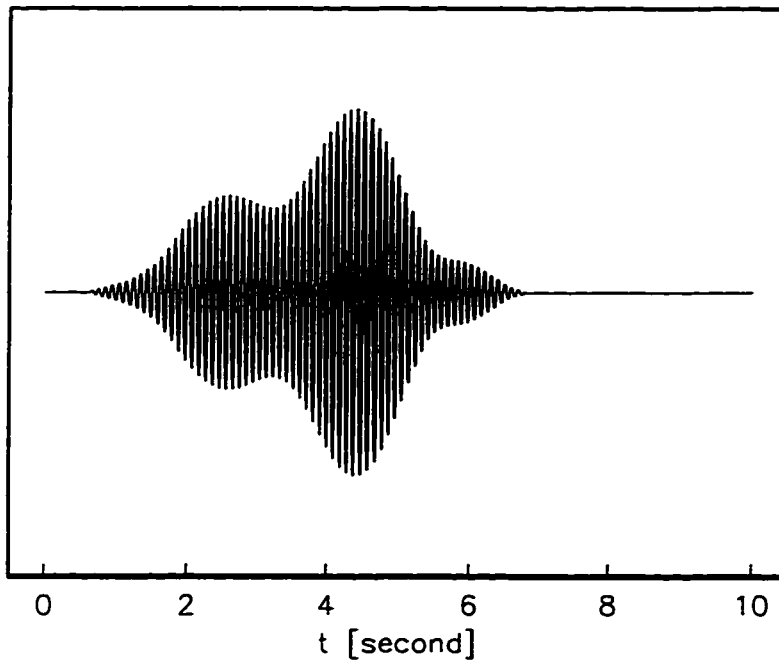
Figure 3.10: Stochastic coupling matrix $\hat{S}$ computed (a) for an isotropic model and (b) for a TI model. Columns and rows represent the modes of the primary field and the modes of the scattered field, respectively.
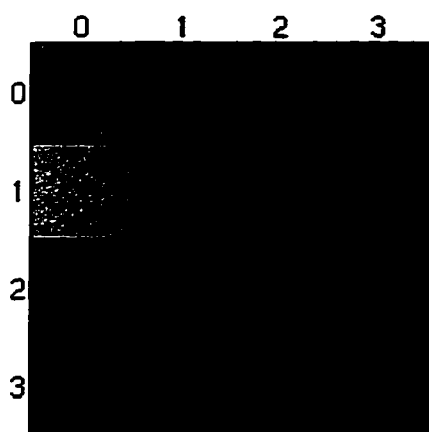
(a) S, ISO   (b) S, TI
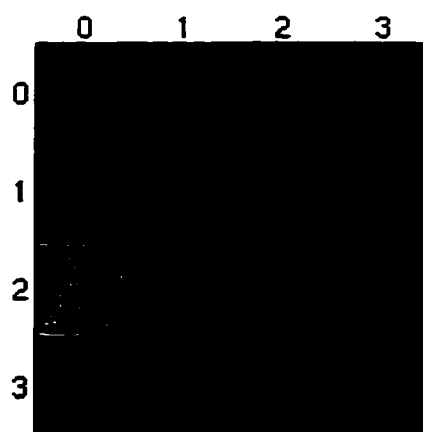
3.3 Summary and Conclusions

We have developed a numerical code for simulation in range-dependent media from the coupled mode theory for fluid-elastic media. A realistic range-dependent shallow water model, which may also include transversely isotropic sediment layers, is introduced. We have computed the transmission and the reflection matrices, the forward/backward propagating wavefields, and the time domain signals for a realistic deterministic range dependent model. The numerical results reveal the various and complicated effects of the range-dependence and transverse isotropy on the shape of the wavefield in the frequency domain and the signals in the time domain. The effects are caused by the energy conversion to different modes due to coupling, broadening of the energy propagation channel (waveguide) and the change in geometry of the propagation channel.

The stochastic coupling matrices are also computed for random rough boundaries. The results show that stochastic boundary roughness plays an important role in scattering of the fluid/solid interface waves.

Probably the greatest advantage to employing coupled modes for investigating range dependent wave propagation is the physical insight provided. There are five different computational products that can be examined: 1. The coupling matrices B and S describe how much of mode r is mixed into mode q; 2. The reflection and transmission matrices R and T give information on which modes have been transmitted or reflected by the structure essentially defining the spatial pass bands and the stop bands of the structure; 3. Single mode results in transform (mode) space; 4. Multi-mode results in transform space; 5. Time domain signals.

Chapter 4

THE EFFECT OF STOCHASTIC ROUGH INTERFACES ON COUPLED-MODE ELASTIC WAVES

The effect of stochastic fluctuations of the interface boundaries has been incorporated into the elastic coupled mode equations for 2-D range dependent media. We assume the medium to be characterized by some deterministic range-dependent layered structure superposed with stochastic boundary fluctuations. The deterministic range-dependent structure defines the reference structure, and the reference structure with superposed stochastic fluctuations defines the true layer boundaries in the medium. The boundary conditions on the true boundary are expanded about the reference boundary, and 1st order perturbation theory is applied to the boundary conditions as well as to the equation of motion. The 0th order system and the 1st order system represent wave propagation in the deterministic model and in the stochastic model with the first order perturbation of roughness, respectively. The solution of the $\mathcal{O}(1)$ system is referred to the primary field. The solutions to the first order system ($\mathcal{O}(\varepsilon)$) relate the coherent field and the scattered field. The two wavefields of the $\mathcal{O}(\varepsilon)$ system, the coherent field and the scattered field, are represented as vectors in an abstract local mode space, i.e., as the superposition of local modes multiplied by the stochastic modal amplitudes. Propagation of coupled mode elastic waves in a 2-D deterministic range-dependent medium is represented by a unitary coupled-mode propagator. The evolution equation for the stochastic medium and the stochastic coupling matrices, which acts to convert the coherent field to the scattered field, is derived. Enforcing energy conservation on the $\mathcal{O}(\varepsilon)$ system leads

to the requirement that the propagator for the stochastic medium must satisfy a Lippmann-Schwinger type integral equation, whose solution can be represented by a formal perturbation series for the multiply scattered wavefields. The Dyson equation for the mean propagator and the Bethe-Salpeter equation for the covariance of the propagator are derived using diagram methods. These formal theoretical results are valid to all orders of multiple scattering. In the second part of the paper the Born approximation to the Lippmann-Schwinger integral equation is used to extract information about attenuation due to rough surface scattering and in the design of an inverse problem for the boundary roughness variance and correlation length. By defining the modal scattering cross section, the formula for the scattering Q_s^{-1} from the Born approximation for the scattered field is derived. The modal scattering cross section and scattering Q_s for a range dependent model with stochastic roughness are computed for both exponential and Gaussian correlation functions. Finally, a formula for the power spectrum of the coherent field is derived from the Born approximation, and an inversion for the roughness variance and correlation length is designed by power spectrum fitting.

4.1   Statistical Description of Rough Surfaces

To characterize the medium, we define the boundary roughness function $\gamma(x)$ as the deviation of the boundary function of the exact structure $h(x)$ from the boundary function of the reference structure $h^0(x)$:

$$h(x) \equiv h^0(x) + \varepsilon\gamma(x), \tag{4.1}$$

where $\varepsilon(\ll 1)$ is a relative amplitude of the RMS height of roughness compared with the overall variation of the reference boundary. The function $h^0(x)$ is deterministic and assumed to be known. A schematic of the relation between the exact boundary $h(x)$ and the reference boundary $h^0(x)$ is presented in Fig. 4.1.

Figure 4.1: Schematic representation of the exact boundary and the reference boundary. $\hat{\mathbf{N}}$ is the normal vector to the exact boundary and $\hat{\mathbf{N}}_0$ is the normal vector to reference boundary.
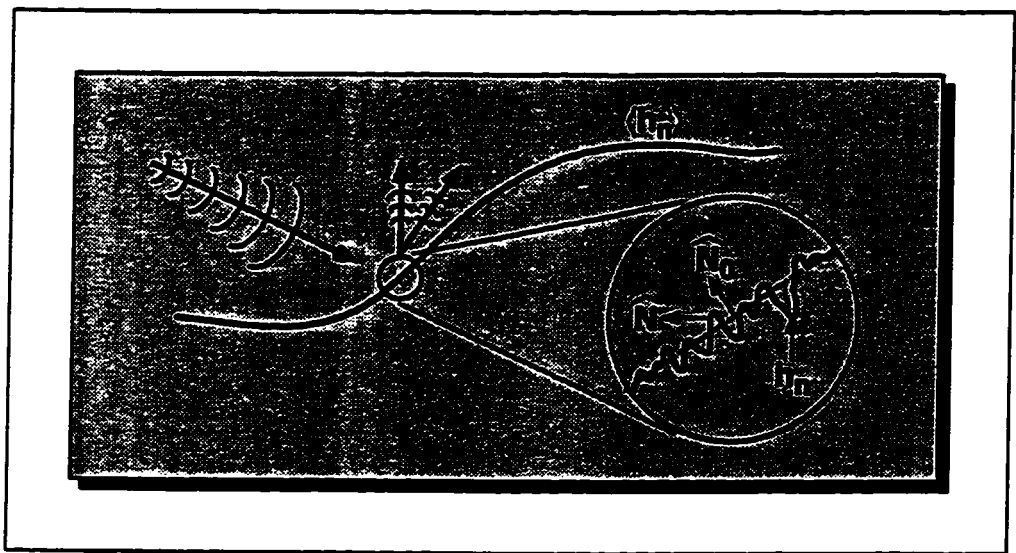
The statistical moments and parameters of the random roughness function $\gamma(x)$ relate directly to those of the boundary function $h(x)$ because the reference boundary function $h^0(x)$ is deterministic. Hereafter, we will use the roughness function to study the effect of the exact boundaries on scattering and their statistical characteristics.

We assume the reference stucture is already known from either direct measurement or indirectly, e.g., by solution of some inverse problem. We allow it to be any deterministic range dependent structure, e.g., a shallowing ocean, a thinning or thickening crust, or a mountain root.

We summarize the statistical properties of the stochastic process $\gamma(x)$. Most of the properties are quite standard. However, we include them here for later use.

1. $\gamma(x)$ is assumed a *zero-mean* (or *centered*) process:

$$\langle \gamma \rangle_E = 0, \tag{4.2}$$

where $\langle ... \rangle_E$ indicates ensenble average over all possible realization.

2. The averaged quantities $\langle \gamma(x_1)\gamma(x_2) \cdots \gamma(x_l) \rangle_E$ depend on the configuration of the points $x_1, x_2, \ldots, x_l$ because for most random media there exists a correlation length (a scale length of heterogeniety) a, i.e., the values of γ at points of separation larger than the correlation length a are uncorrelated. To express the dependence of the averaged quantity on the correlation length, we introduce the *l-point correlation functions* $\Gamma_l(x_1, x_2, \ldots, x_l)$ and we expand these averaged quantities in the following cluster expansions in terms of the l-point correlation functions (Frisch 1968; Nayfeh 1973):

$$\langle \gamma(x_1)\gamma(x_2) \rangle_E = \Gamma_2(x_1, x_2)$$

$$\langle \gamma(x_1)\gamma(x_2)\gamma(x_3) \rangle_E = \Gamma_3(x_1, x_2, x_3)$$

$$\langle \gamma(x_1)\gamma(x_2)\gamma(x_3)\gamma(x_4) \rangle_E = \Gamma_2(x_1, x_2)\Gamma_2(x_3, x_4) + \Gamma_2(x_1, x_3)\Gamma_2(x_2, x_4)$$

$$+ \Gamma_2(x_1, x_4)\Gamma_2(x_2, x_3) + \Gamma_4(x_1, x_2, x_3, x_4) \tag{4.3}$$

$$\vdots$$

$$\langle \gamma(x_1)\gamma(x_2)\cdots\gamma(x_l)\rangle_E \;=\; \sum_{l_1+\cdots+l_s=l} \Gamma_{l_1}(x_1,\ldots,x_{l_1})\Gamma_{l_2}(x_1,\ldots,x_{l_2})\cdots$$
$$\times \Gamma_{l_s}(x_1,\ldots,x_{l_s})$$

where $l_i \geq 2$. Thus the summation in the last equation is extended over all possible partitions of the set $x_1, x_2, \ldots, x_l$ into clusters of at least two points. In the case of a centered Gaussian stochastic function, only the two-point correlation function $\Gamma_2(x_1, x_2)$ is nonvanishing; moments of $2l$, $\langle \gamma(x_1)\cdots\gamma(x_{2l})\rangle_E$, can be written as sums of $\frac{(2l)!}{2^l p!}$ terms, each of which is a product of two-point correlation functions; moments of odd order vanish.

3. The l-point correlation function has the following property (Frisch 1968): $\Gamma_l(x_1, x_2, \ldots, x_l)$ vanishes whenever the points $x_1, \ldots, l$ are not inside a common sphere whose diameter equals the correlation length a. Observe that the moment,

$$\langle \gamma(x_1)\gamma(x_2)\gamma(x_3)\gamma(x_4)\rangle_E \;=\; \Gamma_2(x_1, x_2)\Gamma_2(x_3, x_4) + \Gamma_2(x_1, x_3)\Gamma_2(x_2, x_4)$$
$$+ \Gamma_2(x_1, x_4)\Gamma_2(x_2, x_3) + \Gamma_4(x_1, x_2, x_3, x_4) \quad (4.4)$$

do not satisfy this condition. If, for example,

$$|x_1 - x_2| < a; \quad |x_3 - x_4| < a; \quad |x_1 - x_3| \gg a, \quad (4.5)$$

then

$$\langle \gamma(x_1)\gamma(x_2)\gamma(x_3)\gamma(x_4)\rangle_E = \Gamma_2(x_1, x_2)\Gamma_2(x_3, x_4) \neq 0, \quad (4.6)$$

or if

$$|x_1 - x_3| < a; \quad |x_2 - x_4| < a; \quad |x_1 - x_2| \gg a, \quad (4.7)$$

then

$$\langle \gamma(x_1)\gamma(x_2)\gamma(x_3)\gamma(x_4)\rangle_E = \Gamma_2(x_1, x_3)\Gamma_2(x_2, x_4) \neq 0. \quad (4.8)$$

4. Especially, the 2-point correlation functions $\Gamma_2(x_1, x_2)$ is defined as a product of the variance of $\gamma(x)$, $\langle \gamma^2 \rangle_E$, and the normalized autocorrelation function $N(|x_1 - x_2|)$:

$$\Gamma_2(x_1, x_2) \equiv \left\langle \gamma^2 \right\rangle_E N(|x_1 - x_2|). \qquad (4.9)$$

The autocorrelation function $N(|x_1 - x_2|)$ has the property that $N(r) = 1$ for $r = |x_1 - x_2| = 0$. As r increase $N(r)$ will usually decay to zero, with the shape of this decay being dependent on the type of surface and with the rate of decay being dependent on the distance over which points become uncorrelated (Ogilvy 1991).

5. $\gamma(x)$ is assumed to be a spatially stationary process. The definition of a stationary process is that any statistical properties do not depend on their absolute position, i.e., the statistics of one section of the surface will be the same as the statistics determined from a different section of the same surface.

6. $\gamma(x)$ is assumed to be ergodic. A stochastic process is ergodic if any statistical average taken over many different parts of one surface realization (spatial averaging) is the same as an average over many realizations (ensemble averaging) as long as the area over which the averaging takes place is sufficiently large for a statistical description to be meaningful.

The fifth and the sixth properties may be assumed only for local wave propagation, i.e., wave propagation through the media where the lateral change of the reference boundary is smooth and continuous, the environment and the history of the material evolution are similar, dynamic process on the interfaces are ignorable, and drastic variations of material properties (types) do not occur over the propagation path. For the global wave propagation, the fifth and the sixth properties may be assumed as local concepts, i.e., $\gamma(x)$ may be assumed locally stationary and locally ergodic.

Rough surfaces can be characterized by their statistical moments. The first-order moment, the mean value, of $\gamma(x)$ is always zero in our case. The second-order moment, the covariance, is the most frequently used among those statistical moments for studying the characteristics of a stochastic process. The second moment provides information on the dispersion, or spread, about the center of gravity of a distribution (Rytov, Kravtsov & Tatarskii 1987). The covariance function can be determined by the autocorrelation function and two statistical parameters, i.e., the variance $\langle \gamma^2 \rangle_E$ (or RMS height $\sqrt{\langle \gamma^2 \rangle_E}$) and the correlation length a.

The extent to which this roughness affects wave scattering behavior is the main subject of this paper. Such effects can be studied by comparing the profile of the surface with different autocorrelation functions as well as changing the statistical parameters. Two convenient choices for the correlation function are Gaussian and exponential. The Gaussian autocorrelation function is

$$N(r) = \exp\left(-\frac{r^2}{a^2}\right) \quad \text{the Gaussian autocorrelation function,} \quad (4.10)$$

where a is a correlation length.

An alternative form of correlation function is exponential:

$$N(r) = \exp\left(-\frac{r}{a}\right) \quad \text{the exponential autocorrelation function.} \quad (4.11)$$

Fig. 4.2 shows two surfaces of the same correlation length. The upper surface has a Gaussian correlation function, and the correlation function of the lower surface is exponential (Ogilvy 1991). We use both the Gaussian autocorrelation function and the exponential autocorrelation function for the numerical computation and compare them.

Another important factor affecting wave scattering are two statistical parameters, the variance and the correlation length. Each surface in Fig. 4.3 has a Gaussian height distribution and the same RMS height. However, the surface profiles are very different because of the different correlation lengths (Ogilvy 1991)

Figure 4.2: Rough surfaces of the same correlation length (0.3 mm) but different autocorrelation functions. (a) Gaussian autocorrelation function, (b) exponential autocorrelation function (permission for use has been requested from IOP Publishing Ltd.).
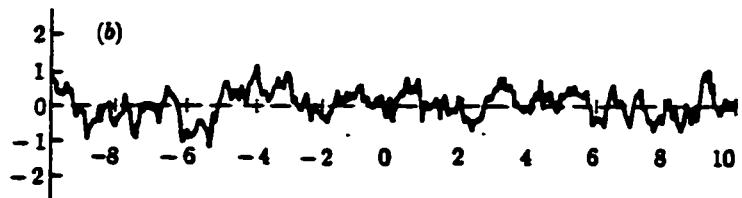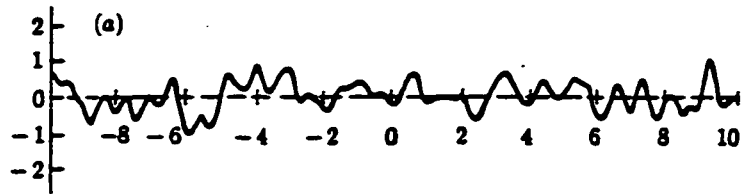
Figure 4.3: Gaussian rough surfaces of the same RMS height (0.5 mm) but different correlation lengths. The correlation length a controls the rate of change of surface height with distance along the surface (permission for use has been requested from IOP Publishing Ltd.).

(a) a = 0.3

(b) a = 0.1

(c) a = 1.0
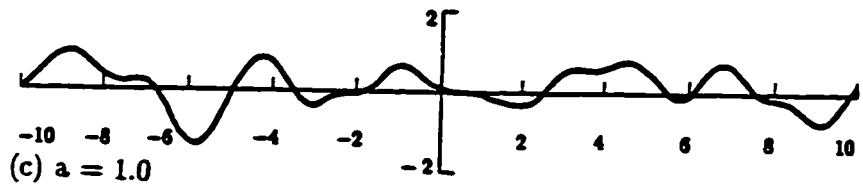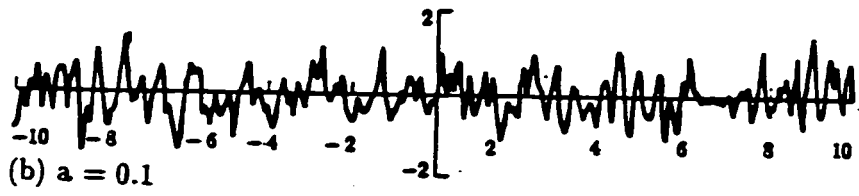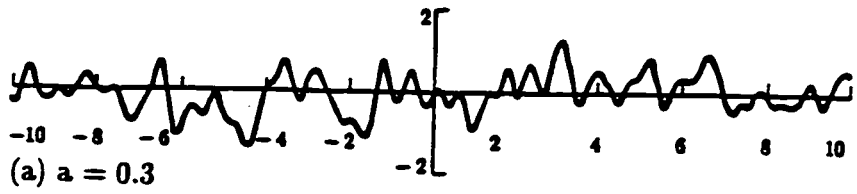
4.2 1st Order Perturbation Theory Applied to Coupled Equation of Motion and Boundary Conditions

The effect of stochastic boundary fluctuations from the reference structure has been incorporated into the elastic coupled mode equations for 2-D range dependent media by applying first order perturbation theory. The first order perturbation gives fairly good results as long as the ratio between the RMS height of the roughness and the overall variation of the reference boundary is small.

The equation of motion for an elastic medium can be written as a set of first-order coupled equations for the 6-component displacement-stress vector, $v = (u, T(\hat{x}))^t$ (Maupin 1988):

$$\frac{\partial v}{\partial x} = Av + F^s. \tag{4.12}$$

The boundary condition on the exact boundary is

$$\left[T(\hat{N})\right]_n = 0 \quad \text{for the } n^{th} \text{ interface,} \tag{4.13}$$

where

$$v = \begin{pmatrix} u \\ T(\hat{x}) \end{pmatrix} = \begin{pmatrix} u & v & w & \tau_{xx} & \tau_{xy} & \tau_{xz} \end{pmatrix}^t, \tag{4.14}$$

$$F^s = \begin{pmatrix} 0 \\ -f^s \end{pmatrix} \delta(r - r_s), \tag{4.15}$$

and the square brackets $[...]_n$ denote a jump in the enclosed quantity at the nth interface. The external line force f^s is applied at $r = r_s$, and the matrix A for a general anisotropic elastic medium is derived in Maupin (1988). The superscript $(...)^t$ represents the transpose of a vector or matrix. Here the displacement-stress vector v is assumed time-harmonic:

$$v(x, z, k_y, \omega) = \int_{-\infty}^{\infty} \int_{-\infty}^{\infty} v(x, z, y, t) \exp(-i\omega t) \exp(ik_y y) \, dy \, dt. \tag{4.16}$$

In Fig. 4.1, the exact boundary $h(x)$, and the reference boundary $h^0(x)$, are described schematically. A unit vector $\hat{N}$ is the vector normal to the true boundary

$h(x)$, and $\hat{\mathbf{N}}_o$ is the vector normal to the reference boundary. We will expand the boundary conditions on the exact boundary about the reference boundary $h^0(x)$, and apply perturbation theory to the boundary conditions as well as to the equation of motion. The $\mathcal{O}(\varepsilon)$ perturbation of the boundary roughness will be included in the $\mathcal{O}(\varepsilon)$ order system of equations.

Now we look for a solution of the equation of motion (4.12) along with the boundary condition (4.13) in the form of an expansion in powers of ε (Bass & Fuks 1979; Sobczyk 1984):

$$\mathbf{v}(x,z) = \mathbf{v}_0(x,z) + \varepsilon\mathbf{v}_1(x,z) + \varepsilon^2\mathbf{v}_2(x,z) + \ldots \qquad (4.17)$$

Substituting eq. (4.17) into the equation of motion (4.12), and collecting terms by their order in ε yields

$$\mathcal{O}(1): \frac{\partial\mathbf{v}_0}{\partial x} = \mathbf{A}\mathbf{v}_0 + \mathbf{F}^s, \qquad (4.18)$$

$$\mathcal{O}(\varepsilon): \frac{\partial\mathbf{v}_1}{\partial x} = \mathbf{A}\mathbf{v}_1. \qquad (4.19)$$

We also apply the same perturbation procedure to the boundary condition eq. (4.13). Expanding the boundary condition eq. (4.13) about the reference boundary $h_n^0(x)$ yields

$$\left[\mathbf{T}(\hat{\mathbf{N}}_o)\right]_n + (\varepsilon\gamma_n)\frac{\partial}{\partial N_o}\left[\mathbf{T}(\hat{\mathbf{N}})\right]_n\Big|_{z=h_n^0} + \frac{1}{2!}(\varepsilon\gamma_n)^2\frac{\partial^2}{\partial N_o^2}\left[\mathbf{T}(\hat{\mathbf{N}})\right]_n\Big|_{z=h_n^0} + \ldots = 0, \quad (4.20)$$

where

$$\frac{\partial}{\partial N_o} \equiv \hat{\mathbf{N}}_o\cdot\nabla$$
$$= \frac{1}{\sqrt{1+\left(h_n^0\right)^2}}\left(-h_n^0,0,1\right)\cdot\left(\frac{\partial}{\partial x},\frac{\partial}{\partial y},\frac{\partial}{\partial z}\right)$$
$$= \frac{1}{\sqrt{1+\left(h_n^0\right)^2}}\left(\frac{\partial}{\partial z}-h_n^0\frac{\partial}{\partial x}\right), \qquad (4.21)$$

and

$$\dot{h}_n^0 \equiv \frac{\partial}{\partial x} h_n^0.$$

(4.22)

We also express the traction as a power series in ε:

$$\mathbf{T}(\hat{\mathbf{N}}) = \mathbf{T}_0(\hat{\mathbf{N}}) + \varepsilon\mathbf{T}_1(\hat{\mathbf{N}}) + \varepsilon^2\mathbf{T}_2(\hat{\mathbf{N}}) + ...$$

(4.23)

Substituting eq. (4.23) into the boundary condition eq. (4.20) gives

$$\left[\mathbf{T}_0(\hat{\mathbf{N}}_o)\right]_n + \varepsilon\left[\mathbf{T}_1(\hat{\mathbf{N}}_o)\right]_n + (\varepsilon\gamma_n)\frac{\partial}{\partial N_o}\left[\mathbf{T}_0(\hat{\mathbf{N}})\right]_n\Big|_{z=h_n^0} + \mathcal{O}(\varepsilon^2) = 0$$

(4.24)

Now the $\mathcal{O}(1)$ and the $\mathcal{O}(\varepsilon)$ boundary conditions are

$$\mathcal{O}(1) \quad : \quad \left[\mathbf{T}_0(\hat{\mathbf{N}}_o)\right]_n = 0$$

$$\Longrightarrow \quad [\mathbf{T}_0(\hat{z})]_n = \dot{h}_n^0\,[\mathbf{T}_0(\hat{x})]_n\,,$$

(4.25)

$$\mathcal{O}(\varepsilon) \quad : \quad \left[\mathbf{T}_1(\hat{\mathbf{N}}_o)\right]_n + \gamma_n\frac{\partial}{\partial N_o}\left[\mathbf{T}_0(\hat{\mathbf{N}})\right]_n\Big|_{z=h_n^0} = 0$$

$$\Longrightarrow \quad [\mathbf{T}_1(\hat{z})]_n = \dot{h}_n^0\,[\mathbf{T}_1(\hat{x})]_n + \gamma_n\frac{\partial}{\partial N_o}\left[\mathbf{T}_0(\hat{\mathbf{N}}_o)\right]_n\,.$$

(4.26)

By converting the traction discontinuities in the boundary conditions eqs. (4.25) & (4.26) into the body-force equivalents (Burridge & Knopoff 1964; Maupin 1988), the $\mathcal{O}(1)$ and the $\mathcal{O}(\varepsilon)$ equations of motion and boundary conditions can be written as:

$$\mathcal{O}(1) \quad : \quad \frac{\partial v_0^{(0)}}{\partial x} = \mathbf{A}v_0^{(0)} + \mathbf{F}^s + \mathbf{F}^0(v_0^{(0)}),$$

(4.27)

$$\left[\mathbf{T}_0^{(0)}(\hat{z})\right]_n = 0,$$

$$\mathcal{O}(\varepsilon) \quad : \quad \frac{\partial v_1^{(1)}}{\partial x} = \mathbf{A}v_1^{(1)} + \mathbf{F}^1(v_0^{(1)}, v_1^{(1)}),$$

(4.28)

$$\left[\mathbf{T}_1^{(1)}(\hat{z})\right]_n = 0,$$

where

$$\mathbf{F}^0(v_0^{(0)}) \quad = \begin{pmatrix} 0 \\ \mathbf{f}^0 \end{pmatrix} = \sum_n \dot{h}_n^0 \begin{pmatrix} 0 \\ \left[\mathbf{T}_0^{(0)}(\hat{x})\right]_n \end{pmatrix} \delta(z - h_n^0),$$

(4.29)

$$\mathbf{F}^1(\mathbf{v}_0^{(1)}, \mathbf{v}_1^{(1)}) = \begin{pmatrix} 0 \\ \mathbf{f}^1 \end{pmatrix}$$

$$= \sum_n \begin{pmatrix} 0 \\ h_n^0 \left[\mathbf{T}_1^{(1)}(\hat{\mathbf{x}}) \right]_n + \gamma_n \frac{\partial}{\partial N_o} \left[\mathbf{T}_0^{(1)}(\hat{\mathbf{N}}_o) \right]_n \end{pmatrix} \delta(z - h_n^0). \quad (4.30)$$

The superscripts of the wavefields have been introduced for bookkeeping. They represent the systems that they belong to, i.e., the superscript (0) for the zeroth order system and the superscript (1) for the $\mathcal{O}(\varepsilon)$ system. Note that the boundary conditions are now homogeneous. The inhomogeneous terms in eq. (4.25) and eq. (4.26) have been mapped to equivalent body force terms in the equations of motion, eq. (4.27) and eq. (4.28). The body-force equivalent $\mathbf{F}^0$ in the $\mathcal{O}(1)$ system (4.27) represents the effect of the slope of the reference structure, so the $\mathcal{O}(1)$ system describes wave propagation in deterministic range dependent media with the reference structure. Hereafter, we will refer to the wavefield $\mathbf{v}_0^{(0)}$ as *the primary field*, i.e., the field when there is no boundary fluctuation from the reference structure.

The body-force equivalent $\mathbf{F}^1$ in the $\mathcal{O}(\varepsilon)$ system (4.28) consists of two terms. The first term represents the effect of the slope of the reference boundary on the wavefield $\mathbf{v}_1^{(1)}$, and the second term describes the excitation of the wavefield $\mathbf{v}_1^{(1)}$ due to the scattering of the the other wavefield $\mathbf{v}_0^{(1)}$ by rough surfaces. The $\mathcal{O}(\varepsilon)$ system, therefore, means that the energy loss of the wavefield $\mathbf{v}_0^{(1)}$ during scattering corresponds to the generation of the other wavefield $\mathbf{v}_1^{(1)}$ as waves propagate through the range dependent media with randomly rough boundaries. We will refer to the wavefield $\mathbf{v}_0^{(1)}$ as the *coherent field* and the wavefield $\mathbf{v}_1^{(1)}$ as the *scattered field*.

Note that the $\mathcal{O}(\varepsilon)$ system includes the roughness function $\gamma_n(x)$, but not its derivative. So we are not required to introduce another independent stochastic process for the derivative of $\gamma_n(x)$.

Replacing the coherent field $\mathbf{v}_0^{(1)}$ with the primary field $\mathbf{v}_0^{(0)}$ in the $\mathcal{O}(\varepsilon)$ system

gives the Born approximation which does not satisfy energy conservation. The Born approximation makes algebra much easier, but it can be used only with the assumption that the scattered energy is ignorable as compared with the total energy. The Born approximation is used to derive the formula for scattering Q^{-1} and the power spectrum of the mean squared signals in the last two sections of this paper.

The Green's functions for the equations (4.27) and (4.28) have the same form but the source terms are different. Therefore, we can express the solution of the scattered field as a product of the body-force equivalent for the $\mathcal{O}(\varepsilon)$ system, $\mathbf{F}^1$ and the Green's function for the primary field. In section 5, we expand the Green's function in terms of the depth-dependent normal mode solution, which is equivalent to the solution of the homogeneous forms of differential equations (4.27) and (4.28).

4.3 Unitary Local Mode Spaces

The wavefield in a deterministic range-dependent medium is represented as a sum of reference modes (Kennett 1984) or local modes (Odom 1986; Maupin 1988) with laterally varying modal amplitude coefficients. Here we construct the abstract vector space spanned by the normal modes for a local deterministic depth-dependent medium, the local mode space, and we show that the wavefield scattered by stochastic heterogeneities can also be represented as a vector defined in the local mode space, i.e., a sum of local modes with stochastic modal amplitude coefficients. The abstract vector representation provides the foundation with which we can express the algebraic functions describing propagation in terms of operators defined in the local mode space.

Normal mode vectors of the displacement-stress vector in depth-dependent media $\mathbf{v}^\alpha$ satisfy the homogeneous equation of motion:

$$\frac{\partial}{\partial x}\mathbf{v}^\alpha = \mathbf{A}\mathbf{v}^\alpha = ik_\alpha \mathbf{v}^\alpha \qquad \text{with} \qquad [\mathbf{T}^\alpha(\hat{z})]_n = 0, \qquad (4.31)$$

and they can be written as (Aki & Richards, 1980):

$$\mathbf{v}^\alpha(z, k_\alpha) = \begin{pmatrix} 0 & l_1^\alpha & 0 & 0 & il_3^\alpha & 0 \end{pmatrix}^t \quad \text{for Love waves,} \tag{4.32}$$

$$\mathbf{v}^\alpha(z, k_\alpha) = \begin{pmatrix} r_1^\alpha & 0 & ir_2^\alpha & ir_5^\alpha & 0 & r_3^\alpha \end{pmatrix}^t \quad \text{for Rayleigh waves.} \tag{4.33}$$

Note that Greek indices are used to represent mode numbers throughout this paper. For convenience, new eigenfunctions l_3^α and r_5^α are defined :

$$l_3^\alpha \equiv k_\alpha \mu l_1^\alpha, \tag{4.34}$$

$$r_5^\alpha \equiv \lambda \frac{dr_2^\alpha}{dz} + k_\alpha(\lambda + 2\mu)r_1^\alpha. \tag{4.35}$$

Using those normal modes $\mathbf{v}^\alpha(z, k_\alpha)$, we can define local-mode vectors $\mathbf{v}^\alpha(z, k_\alpha; x)$ for range-dependent media. These are the local depth-dependent eigenfunctions whose boundary depth functions are equivalent to those of a range-*independent* medium at a local point x.

Next we will define a *local mode space* $\mathcal{W}$, which is an abstract vector space whose element vectors are linear combinations of the local modes, i.e., $\sum_\alpha c_\alpha \mathbf{v}^\alpha$, where c_α is a complex number.

For every vector pair $\mathbf{v}$ and $\mathbf{w}$ such that $\mathbf{v}, \mathbf{w} \in \mathcal{W}$, we introduce the Hermitian inner product (Maupin 1988):

$$< \mathbf{v}, \mathbf{w} > \equiv \int_0^\infty \mathbf{v}^\dagger \mathbf{X} \mathbf{w} dz, \tag{4.36}$$

where

$$\mathbf{X} = \sigma_2 \bigotimes \mathbf{I} = \begin{pmatrix} 0 & -i \\ i & 0 \end{pmatrix} \bigotimes \begin{pmatrix} 1 & 0 & 0 \\ 0 & 1 & 0 \\ 0 & 0 & 1 \end{pmatrix} = \begin{pmatrix} \mathbf{0} & -i\mathbf{I} \\ i\mathbf{I} & \mathbf{0} \end{pmatrix}. \tag{4.37}$$

Here † represents the Hermitian conjugate, i.e., the complex conjugate transpose. The matrix σ_2 is the 2nd Pauli matrix and $\mathbf{I}$ is an identity matrix. The complex linear space $\mathcal{W}$ consisting of the local mode vector $\mathbf{v}^\alpha$ with the Hermitian inner product

(4.36) defines a *unitary space* (Shilov, 1977). We also introduce the *norm* (or *length*) of the vector in the local mode space using the Hermitian inner product:

$$\|\mathbf{v}\| \equiv < \mathbf{v}, \mathbf{v} >^{\frac{1}{2}} \tag{4.38}$$

A set of linearly independent local modes form the orthonormal basis of the local mode space W. The orthogonality of the local-mode vectors is proved in Maupin (1988):

$$< \mathbf{v}^{\alpha}, \mathbf{v}^{\beta} > = \delta_{\alpha\beta}. \tag{4.39}$$

The local mode vectors should be normalized such that they have unit length in the local mode space W. Therefore the normalization factor for the αth mode is its norm:

$$\|\mathbf{v}^{\alpha}\| = < \mathbf{v}^{\alpha}, \mathbf{v}^{\alpha} >^{\frac{1}{2}}. \tag{4.40}$$

The normalization factor for Love waves in 2-D media can be derived by applying the Hermitian inner product to the local mode vector for Love waves (4.32):

$$
\begin{aligned}
\|\mathbf{v}^{\alpha}\| &= \left\{ \int_0^{\infty} \begin{pmatrix} 0 & l_1^{\alpha} & 0 & 0 & -il_3^{\alpha} & 0 \end{pmatrix} \begin{pmatrix} 0 & -i\mathbf{I} \\ i\mathbf{I} & 0 \end{pmatrix} \right. \\
&\quad \left. \times \begin{pmatrix} 0 & l_1^{\alpha} & 0 & 0 & il_3^{\alpha} & 0 \end{pmatrix}^t dz \right\}^{\frac{1}{2}} \\
&= \sqrt{\int_0^{\infty} 2 l_1^{\alpha} l_3^{\alpha} dz} \\
&= \sqrt{4k_{\alpha} \left(\frac{1}{2} \int_0^{\infty} \mu \left(l_1^{\alpha} \right)^2 dz \right)} \\
&= \sqrt{4k_{\alpha} I_2^{\alpha}} \\
&= \sqrt{4k_{\alpha} c_{\alpha} U_{\alpha} I_1^{\alpha}} \qquad \text{for Love waves in 2-D media.} \tag{4.41}
\end{aligned}
$$

Here c_{α} and U_{α} are the phase velocity and group velocity of the αth mode respectively. I_1^{α} and I_2^{α} are the first type and the second type of kinetic energy integral, and they are defined in eq. (7.66) and eq. (7.74) of Aki & Richards (1980). The normalization

factor for Rayleigh waves in 2-D media can be derived in the same way:

$$\|\mathbf{v}^\alpha\| = \sqrt{4k_\alpha c_\alpha U_\alpha I_1^\alpha} \qquad \text{for Rayleigh waves in 2-D media.} \qquad (4.42)$$

From a practical standpoint, an appropriate number of discrete modes must be chosen to achieve an acceptable degree of numerical accuracy. Maupin and Kennett (1987) studied the effect of the truncation of the modal expansion, and they suggest that the proper number of discrete modes must be chosen to cover the desired range of phase velocities. Harvey (1981) and Nolet, et. al. (1989) suggest using a locked mode approximation by introduction of a perfect reflector which is placed deep enough to exclude the reflection outside of the time window of interest. This approximation locks the energy into the medium between the free surface and the perfect reflector, and forces eigenvalues to be real if there is no attenuation. Maupin (1996) has recently derived an elegant dyadic representation for the radiation component of the elastic wave Green's function which would allow the locked mode approximation to be dispensed with. In this paper, we consider the discrete modes only.

In the following section, we show how the solution of elastic waves in a deterministic or stochastic range-dependent medium can be represented by the basis of the local mode space W by analytical derivation of the Green's function.

4.4 Local Mode Decompositions of General Solutions and Their Modal Amplitude Coefficients

In what follows, we derive the propagating solutions for the primary field and the scattered field from the Green's function, and represent them by local mode vectors with range-dependent modal amplitude coefficients. The 6-dimensional coupled equation of motion for depth-dependent media with the arbitrary external source $\mathbf{f}^s$ applied at $r = r_s$ is

$$\frac{\partial \mathbf{v}}{\partial x} = \mathbf{A}\mathbf{v} + \mathbf{F}^s \qquad \text{with} \qquad [\mathbf{T}^\alpha(\hat{z})]_n = 0, \qquad (4.43)$$

which can be written in terms of its 3-dimensional element vectors:

$$\frac{\partial}{\partial x}\begin{pmatrix} \mathbf{u} \\ \mathbf{T}(\hat{x}) \end{pmatrix} - \begin{pmatrix} \mathbf{A}_{uu} & \mathbf{A}_{uT} \\ \mathbf{A}_{Tu} & \mathbf{A}_{TT} \end{pmatrix}\begin{pmatrix} \mathbf{u} \\ \mathbf{T}(\hat{x}) \end{pmatrix} = \begin{pmatrix} 0 \\ -\mathbf{f}^s \end{pmatrix}\delta(\mathbf{r}-\mathbf{r}_s)$$

$$\Longrightarrow \begin{pmatrix} \mathbf{I}\frac{\partial}{\partial x}-\mathbf{A}_{uu} & \mathbf{A}_{uT} \\ \mathbf{A}_{Tu} & \mathbf{I}\frac{\partial}{\partial x}-\mathbf{A}_{TT} \end{pmatrix}\begin{pmatrix} \mathbf{u} \\ \mathbf{T}(\hat{x}) \end{pmatrix} = \begin{pmatrix} 0 \\ -\mathbf{f}^s \end{pmatrix}\delta(\mathbf{r}-\mathbf{r}_s), \quad (4.44)$$

where the 3×3 element matrices of $\mathbf{A}$ are derived in Maupin (1988). Employing Gauss elimination, eq. (4.44) can be written in block diagonal form:

$$\begin{pmatrix} \mathbf{L}^u & 0 \\ 0 & \mathbf{L}^T \end{pmatrix}\begin{pmatrix} \mathbf{u} \\ \mathbf{T}(\hat{x}) \end{pmatrix} = \begin{pmatrix} \mathbf{f}_u^s \\ \mathbf{f}_T^s \end{pmatrix}, \quad (4.45)$$

where

$$\mathbf{L}^u = \left(\mathbf{I}\frac{\partial}{\partial x}-\mathbf{A}_{TT}\right)\mathbf{A}_{uT}^{-1}\left(\mathbf{I}\frac{\partial}{\partial x}-\mathbf{A}_{uu}\right)-\mathbf{A}_{Tu}, \quad (4.46)$$

$$\mathbf{L}^T = \left(\mathbf{I}\frac{\partial}{\partial x}-\mathbf{A}_{uu}\right)\left(\mathbf{I}\frac{\partial}{\partial x}-\mathbf{A}_{TT}\right)-\mathbf{A}_{uT}\mathbf{A}_{Tu}, \quad (4.47)$$

$$\mathbf{f}_u^s = \mathbf{f}^s\delta(\mathbf{r}-\mathbf{r}_s), \quad (4.48)$$

$$\mathbf{f}_T^s = -\left(\mathbf{I}\frac{\partial}{\partial x}-\mathbf{A}_{uu}\right)\mathbf{f}^s\delta(\mathbf{r}-\mathbf{r}_s). \quad (4.49)$$

The operators $\mathbf{L}^u$ & $\mathbf{L}^T$ are 2nd order differential operators. The block diagonal form of eq. (4.45) is the matrix representation of decoupled 2nd order equations for the displacement $\mathbf{u}$ and the stress $\mathbf{T}$. Note that an additional source $\mathbf{f}_T^s$ appears for the stress. This is because the equation for stress and displacement have been decoupled. The source $\mathbf{f}^s$ has been transformed into the traction source $\mathbf{f}_T^s$ while $\mathbf{f}_u^s$ is the form appropriate to the displacement. Now we have two independent and completely equivalent representations. We can choose either one to solve, and must use the form of the source appropriate to the representation, i.e., the displacement or the stress (traction). Its solution can be represented by an integration of the product of the source and the 3-dimensional Green's function.

We would like to solve the coupled equations (4.44) for the 6-dimensional vector $\mathbf{v}$ $(= (\mathbf{u}, \mathbf{T}(\hat{\mathbf{x}}))^t)$, which means that the displacement and the traction must be solved simultaneously. To accomplish this, we introduce the 6-dimensional dyadic form of the Green's function $\underline{\mathbf{G}}(\mathbf{r}, \mathbf{r}')$ for the displacement-stress vector which is similar to the 3-dimensional dyadic form of the Green's function for the displacement alone (Snieder 1986):

$$G_{ij}(\mathbf{r}, \mathbf{r}') = \sum_\alpha v_i^\alpha(z, k_\alpha; x) v_j^{\alpha*}(z', k_\alpha; x') e^{i(\phi_\alpha(x) + \frac{\pi}{2})}, \quad \text{or}$$

$$\underline{\mathbf{G}}(\mathbf{r}, \mathbf{r}') = \sum_\alpha i e^{i\phi_\alpha(x)} \mathbf{v}^\alpha(z; x) \mathbf{v}^{\alpha\dagger}(z'; x')$$

$$= \sum_\alpha i e^{i\phi_\alpha(x)} \begin{pmatrix} \mathbf{u}^\alpha \mathbf{u}^{\alpha\dagger} & \mathbf{u}^\alpha \mathbf{T}^{\alpha\dagger} \\ \mathbf{T}^\alpha \mathbf{u}^{\alpha\dagger} & \mathbf{T}^\alpha \mathbf{T}^{\alpha\dagger} \end{pmatrix}, \tag{4.50}$$

where

$$\phi_\alpha(x) = \int_{x_s}^x k_\alpha(\xi) d\xi. \tag{4.51}$$

Note that either source can be used for the coupled equation unlike the decoupled case, and that our dyadic form of the Green's function eq. (4.50) is appropriate to either source: For the displacement source,

$$\sum_\alpha \int i e^{i\phi_\alpha(x)} \begin{pmatrix} \mathbf{u}^\alpha \mathbf{u}^{\alpha\dagger} & \mathbf{u}^\alpha \mathbf{T}^{\alpha\dagger} \\ \mathbf{T}^\alpha \mathbf{u}^{\alpha\dagger} & \mathbf{T}^\alpha \mathbf{T}^{\alpha\dagger} \end{pmatrix} \begin{pmatrix} \mathbf{f}_u^s \\ \mathbf{0} \end{pmatrix} dV'$$

$$= \sum_\alpha \int i e^{i\phi_\alpha(x)} \begin{pmatrix} \mathbf{u}^\alpha \\ \mathbf{T}^\alpha \end{pmatrix} \left\{ \mathbf{u}^{\alpha\dagger} \cdot \mathbf{f}_u^s \right\} dV'. \tag{4.52}$$

For the stress source,

$$\sum_\alpha \int i e^{i\phi_\alpha(x)} \begin{pmatrix} \mathbf{u}^\alpha \mathbf{u}^{\alpha\dagger} & \mathbf{u}^\alpha \mathbf{T}^{\alpha\dagger} \\ \mathbf{T}^\alpha \mathbf{u}^{\alpha\dagger} & \mathbf{T}^\alpha \mathbf{T}^{\alpha\dagger} \end{pmatrix} \begin{pmatrix} \mathbf{0} \\ \mathbf{f}_T^s \end{pmatrix} dV'$$

$$= \sum_\alpha \int i e^{i\phi_\alpha(x)} \begin{pmatrix} \mathbf{u}^\alpha \\ \mathbf{T}^\alpha \end{pmatrix} \left\{ \mathbf{T}^{\alpha\dagger} \cdot \mathbf{f}_T^s \right\} dV'. \tag{4.53}$$

Though either source can be used to represent the solutions of the coupled equation, we choose to use the displacement source $\mathbf{f}_u^s$ throughout this paper. The solutions are rewritten in terms of the Hermitian inner product (4.36):

$$
\begin{aligned}
\mathbf{v}(x, z; \omega) &= \sum_\alpha \mathbf{v}^\alpha(z; x) e^{i\phi_\alpha(x)} \int_{x_s}^x dx' \left\{ \int_{-\infty}^0 \mathbf{v}^{\alpha\dagger}(z'; x') i \begin{pmatrix} \mathbf{f}^s \\ 0 \end{pmatrix} \delta(\mathbf{r} - \mathbf{r}_s) dz' \right\} \\
&= \sum_\alpha \mathbf{v}^\alpha(z; x) e^{i\phi_\alpha(x)} \int_{x_s}^x dx' \\
&\quad \times \left\{ \int_{-\infty}^0 \mathbf{v}^{\alpha\dagger}(z'; x') \begin{pmatrix} 0 & -i\mathbf{I} \\ i\mathbf{I} & 0 \end{pmatrix} \begin{pmatrix} 0 \\ -\mathbf{f}^s \end{pmatrix} \delta(\mathbf{r} - \mathbf{r}_s) dz' \right\} \\
&= \sum_\alpha \mathbf{v}^\alpha(z; x) e^{i\phi_\alpha(x)} \int_{x_s}^x < \mathbf{v}^\alpha(z'; x'), \mathbf{F}^s > dx'.
\end{aligned}
\tag{4.54}
$$

Here, $\mathbf{F}^s$ is defined in eq. (4.15). According to eq. (4.54), we can represent the primary field of the $\mathcal{O}(1)$ system $\mathbf{v}_0^{(0)}$ and the scattered field of the $\mathcal{O}(\varepsilon)$ system $\mathbf{v}_1^{(1)}$ as the Hermitian inner products of the Green's function (4.50) and the source terms $\mathbf{F}^s$, $\mathbf{F}^0$ and $\mathbf{F}^1$ in eq. (4.29) and eq. (4.30):

$$
\begin{aligned}
\mathbf{v}_0^{(0)}(x, z; \omega) &= \sum_\alpha \mathbf{v}^\alpha(z; x) e^{i\phi_\alpha(x)} \\
&\quad \times \int_{x_s}^x \left(< \mathbf{v}^\alpha(z'; x'), \mathbf{F}^s > + < \mathbf{v}^\alpha(z'; x'), \mathbf{F}^0 > \right) dx',
\end{aligned}
\tag{4.55}
$$

$$
\mathbf{v}_1^{(1)}(x, z; \omega) = \sum_\alpha \mathbf{v}^\alpha(z; x) e^{i\phi_\alpha(x)} \int_{x_s}^x < \mathbf{v}^\alpha(z'; x'), \mathbf{F}^1 > dx'.
\tag{4.56}
$$

Eqs. (4.55) and (4.56) can be rewritten as sums of local modes with the range-dependent modal coefficients, $c_\alpha^{(0)}$ and d_α:

$$
\mathbf{v}_0^{(0)}(x, z; \omega) = \sum_\alpha c_\alpha^{(0)}(x) \mathbf{v}^\alpha(z, k_\alpha; x) e^{i\phi_\alpha(x)},
\tag{4.57}
$$

$$
\mathbf{v}_1^{(1)}(x, z; \omega) = \sum_\alpha d_\alpha(x) \mathbf{v}^\alpha(z, k_\alpha; x) e^{i\phi_\alpha(x)},
\tag{4.58}
$$

where the modal coefficients c_α and d_α are

$$
c_\alpha^{(0)}(x) = \int_{x_s}^x < \mathbf{v}^\alpha(z'; x'), \mathbf{F}^s > dx' + \int_{x_s}^x < \mathbf{v}^\alpha(z'; x'), \mathbf{F}^0 > dx',
\tag{4.59}
$$

$$
d_\alpha(x) = \int_{x_s}^x < \mathbf{v}^\alpha(z'; x'), \mathbf{F}^1 > dx'.
\tag{4.60}
$$

The first integration on the r.h.s. of eq. (4.59) is the modal decomposion of the external source $\mathbf{f}^s$, and it can be rewritten by the Hermitian inner product (4.36) and the external source (4.15)

$$
\begin{aligned}
\int_{x_s}^{x} < \mathbf{v}^\alpha(z';x'), \mathbf{F}^s > dx' &= \int_{x_s}^{x} dx' \left\{ \int_0^\infty \mathbf{v}^\alpha(z';x') \mathbf{X} \mathbf{F}^s dz \right\} \\
&= \mathbf{u}^{\alpha*}(z_s, k_\alpha; x_s) \cdot \mathbf{f}^s e^{i\frac{x}{2}},
\end{aligned}
\tag{4.61}
$$

and the initial conditions on c_α and d_α are

$$
c_\alpha^{(0)}(x = x_s) = \mathbf{u}^{\alpha*}(z_s, k_\alpha; x_s) \cdot \mathbf{f}^s e^{i\frac{x}{2}},
\tag{4.62}
$$

$$
d_\alpha(x = x_s) = 0.
\tag{4.63}
$$

We shall show that the coherent field $\mathbf{v}_0^{(1)}$ is also represented by the local modes from the total energy conservation condition for the $\mathcal{O}(\varepsilon)$ system. The norm of the wavefield defined in the local mode space represents the energy it carries. The norm of the sum of the coherent field $\mathbf{v}_0^{(1)}$ and the scattered field $\mathbf{v}_1^{(1)}$ should be a propagation invariant, and should be equal to the initial norm of the primary field for energy conservation, which enables us to represent the coherent field as a vector in the local mode space. More discussion on this topic is detailed in section 8. The coherent field, therefore, is represented as

$$
\mathbf{v}_0^{(1)}(x, z; \omega) = \sum_\alpha c_\alpha(x) \mathbf{v}^\alpha(z, k_\alpha; x) e^{i\phi_\alpha(x)},
\tag{4.64}
$$

The point here is that the solution for the coherent field and the scattered field, as well as the primary field, can be decomposed into the local mode basis with the range-dependent modal amplitude coefficients. The modal amplitude coefficients $(c_1, c_2, \ldots, c_\nu)^t$ are the coordinates of $\mathbf{v}_0^{(1)}$ in the local mode space while the coordinates of $\mathbf{v}_0^{(1)}$ in the configuration space are $(u_x, u_y, u_z, \tau_{xx}, \tau_{xy}, \tau_{zz})^t$. Therefore, the column vectors $\mathbf{c}^{(0)}$, $\mathbf{c}$ and $\mathbf{d}$ represent the abstract vectors of the wavefields $\mathbf{v}_0^{(0)}$, $\mathbf{v}_0^{(1)}$ and $\mathbf{v}_1^{(1)}$ in the local mode space, respectively.

From the exact formula for the modal amplitudes eqs. (4.59) & (4.60), we discuss the physical meaning of each coefficient. First equation (4.60) means that $d_\alpha(x)$ is the projection of the effective source due to the $\mathcal{O}(\varepsilon)$ perturbation of the boundary roughness in the range (x_s, x) onto the local-mode space. We also see that $d_\alpha(x)$ is a stochastic modal amplitude coefficient because the body-force equivalent $\mathbf{F}^1$ in eq. (4.60) includes the stochastic process $\gamma(x)$.

The amplitude coefficient $c_\alpha^{(0)}(x)$ of eq. (4.59), on the other hand, is the projection of the external source and the effective source due to the slope of the reference boundaries in the range (x_s, x) onto the local-mode space, and is deterministic.

Therefore, the dyadic form of the eigenfunction expansion of the Green's function eq. (4.50) can be interpreted as a projector of the source onto the local-mode space. The range varying modal amplitude coefficients can be interpreted as the local mode space projection of the effective source due to the deterministic and stochastic boundary heterogeneities.

4.5 Spatial Evolution Equations and Coupling Matrices

The spatial evolution equation for the deterministic laterally heterogeneous medium was derived in the earlier works (Kennett 1984; Odom 1986; Maupin 1988). Their equations and boundary conditions are exactly same as the $\mathcal{O}(1)$ system of ours, eq. (4.27), i.e. their spatial evolution equation is equal to the evolution equation for the primary field in this paper. Then, following Maupin (1988), the spatial evolution equation of the primary field can be written as

$$
\begin{aligned}
\frac{\partial c_\alpha^{(0)}}{\partial x} &= \sum_\beta \left\{ \left(<\mathbf{v}^\alpha, \frac{\partial \mathbf{v}^\beta}{\partial x} > + i \sum_n h_n^0 \left[\mathbf{u}^{\alpha*} \cdot \mathbf{T}^\beta(\hat{x}) \right]_n \right) e^{i(\phi_\beta - \phi_\alpha)} \right\} c_\beta^{(0)} \\
&= \sum_\beta B_{\alpha\beta} c_\beta^{(0)}.
\end{aligned}
\tag{4.65}
$$

The evolution equation for the primary field is the same as that of the earlier works. The evolution equation for the stochastic modal amplitude coefficients can be derived

in a similar manner for the wavefield scattered by the stochastic boundary roughness. Substituting the local mode representation of the scattered field eq. (4.58) into the equation of motion (4.28) for the $\mathcal{O}(\varepsilon)$ system gives

$$\frac{\partial d_\beta}{\partial x}\mathbf{v}^\beta e^{i\phi_\beta} + d_\beta \frac{\partial \mathbf{v}^\beta}{\partial x}e^{i\phi_\beta} + ik_\beta d_\beta \mathbf{v}^\beta e^{i\phi_\beta} = d_\beta \mathbf{A}\mathbf{v}^\beta e^{i\phi_\beta} + \mathbf{F}^1. \tag{4.66}$$

Note that the summation convention is used in eq. (4.66). Taking the inner product with $\mathbf{v}^\alpha$ and eq. (4.66), and applying the orthogonality of the local modes and the relation $< \mathbf{v}^\alpha, \mathbf{A}\mathbf{v}^\beta >= ik_\beta < \mathbf{v}^\alpha, \mathbf{v}^\beta >$ yields

$$\frac{\partial d_\alpha}{\partial x} = \sum_\beta \left(< \mathbf{v}^\alpha, \frac{\partial \mathbf{v}^\beta}{\partial x} > e^{i(\phi_\beta - \phi_\alpha)} \right) d_\beta + < \mathbf{v}^\alpha, \mathbf{F}^1 > e^{-i\phi_\alpha}. \tag{4.67}$$

The second term on the r.h.s. of eq. (4.67) is

$$< \mathbf{v}^\alpha, \mathbf{F}^1 > e^{-i\phi_\alpha} = i\mathbf{u}^{\alpha*} \cdot \mathbf{f}^1 e^{-i\phi_\alpha}, \tag{4.68}$$

where the body-force equivalent for the $\mathcal{O}(\varepsilon)$ system is

$$\mathbf{f}^1 = \sum_n \left(h_n^0 \left[\mathbf{T}_1^{(0)}(\hat{\mathbf{x}}) \right]_n + \gamma_n \frac{\partial}{\partial N_o} \left[\mathbf{T}_0^{(0)}(\hat{\mathbf{N}}_o) \right]_n \right) \delta(z - h_n^0). \tag{4.69}$$

We also substitute the local mode representation of the coherent field eq. (4.64) and the scattered field eq. (4.58) into $\mathbf{f}^1$. Then eq. (4.68) becomes

$$< \mathbf{v}^\alpha, \mathbf{F}^1 > e^{-i\phi_\alpha} = \sum_\beta \left(i \sum_n h_n^0 \left[\mathbf{u}^{\alpha*} \cdot \mathbf{T}^\beta(\hat{\mathbf{x}}) \right]_n e^{-i\phi_\alpha} \right) d_\beta$$

$$+ \sum_\beta D_{\alpha\beta} c_\beta + \sum_\beta E_{\alpha\beta} \frac{\partial c_\beta}{\partial x}, \tag{4.70}$$

where the matrices $D_{\alpha\beta}$ and $E_{\alpha\beta}$ are

$$D_{\alpha\beta} = i\sum_n \gamma_n \frac{1}{\sqrt{1 + \left(h_n^0\right)^2}} \left\{ \left[\mathbf{u}^{\alpha*} \cdot \frac{\partial \mathbf{T}^\beta(\hat{\mathbf{N}}_o)}{\partial z} \right]_n - ik_\beta h_n^0 \left[\mathbf{u}^{\alpha*} \cdot \mathbf{T}^\beta(\hat{\mathbf{N}}_o) \right]_n \right.$$

$$\left. - h_n^0 \left[\mathbf{u}^{\alpha*} \cdot \frac{\partial \mathbf{T}^\beta(\hat{\mathbf{N}}_o)}{\partial x} \right]_n \right\} e^{i(\phi_\beta - \phi_\alpha)}$$

$$= i \sum_n \gamma_n \frac{1}{\sqrt{1 + \left(\dot{h}_n^0\right)^2}} \left\{ \left[\mathbf{u}^{\alpha *} \cdot \frac{\partial \mathbf{T}^\beta(\hat{\mathbf{N}}_o)}{\partial z} \right]_n - i k_\beta \dot{h}_n^0 \left[\mathbf{u}^{\alpha *} \cdot \mathbf{T}^\beta(\hat{\mathbf{N}}_o) \right]_n \right.$$

$$+ \left(\dot{h}_n^0\right)^2 \left[\mathbf{u}^{\alpha *} \cdot \frac{\partial \mathbf{T}^\beta(\hat{\mathbf{N}}_o)}{\partial z} \right]_n - \frac{\dot{h}_n^0 \ddot{h}_n^0}{1 + \left(\dot{h}_n^0\right)^2} \left[\mathbf{u}^{\alpha *} \cdot \mathbf{T}^\beta(\hat{\mathbf{N}}_o) \right]_n$$

$$\left. + \frac{\dot{h}_n^0 \ddot{h}_n^0}{\sqrt{1 + \left(\dot{h}_n^0\right)^2}} \left[\mathbf{u}^{\alpha *} \cdot \mathbf{T}^\beta(\hat{\mathbf{x}}) \right]_n \right\} e^{i(\phi_\beta - \phi_\alpha)}, \tag{4.71}$$

$$E_{\alpha\beta} = -i \sum_n \gamma_n \frac{\ddot{h}_n^0}{\sqrt{1 + \left(\dot{h}_n^0\right)^2}} \left[\mathbf{u}^{\alpha *} \cdot \mathbf{T}^\beta(\hat{\mathbf{N}}_o) \right]_n e^{i(\phi_\beta - \phi_\alpha)}. \tag{4.72}$$

Here the matrices $D_{\alpha\beta}$ and $E_{\alpha\beta}$ contain the stochastic process γ_n as well as the deterministic slope of the reference boundary $\dot{h}_n^0$, while $B_{\alpha\beta}$ includes only deterministic slope $\dot{h}_n^0$. Note that while deriving the final form of $D_{\alpha\beta}$ in eq. (4.71), the transformation, $\left[\frac{\partial a}{\partial x}\right]_n = -\dot{h}_n^0 \left[\frac{\partial a}{\partial z}\right]_n$ for a continuous quantity a along the interfaces, and the following relations are used:

$$\left[\frac{\partial \mathbf{T}^\beta(\hat{\mathbf{N}}_o)}{\partial x} \right]_n = \frac{\partial}{\partial x} \left[\frac{1}{\sqrt{1 + \left(\dot{h}_n^0\right)^2}} \left(\mathbf{T}^\beta(\hat{\mathbf{z}}) - \dot{h}_n^0 \mathbf{T}^\beta(\hat{\mathbf{x}}) \right) \right]_n$$

$$= \frac{\ddot{h}_n^0}{1 + \left(\dot{h}_n^0\right)^2} \left[\mathbf{T}^\beta(\hat{\mathbf{N}}_o) \right]_n + \dot{h}_n^0 \left[\frac{\partial \mathbf{T}^\beta(\hat{\mathbf{N}}_o)}{\partial z} \right]_n$$

$$- \frac{\ddot{h}_n^0}{\sqrt{1 + \left(\dot{h}_n^0\right)^2}} \left[\mathbf{T}^\beta(\hat{\mathbf{x}}) \right]_n. \tag{4.73}$$

By substituting eq. (4.70) into eq. (4.67) and using the evoution equation for the primary field eq. (4.65), the spatial evolution equation for the coherent field and the

scattered field becomes

$$\frac{\partial d_\alpha}{\partial x} = \sum_\beta \left\{ \left(< \mathbf{v}^\alpha, \frac{\partial \mathbf{v}^\beta}{\partial x} > + i \sum_n h_n^0 \left[\mathbf{u}^{\alpha*} \cdot \mathbf{T}^\beta(\hat{\mathbf{x}}) \right]_n \right) e^{i(\phi_\beta - \phi_\alpha)} \right\} d_\beta$$

$$+ \sum_\beta D_{\alpha\beta} c_\beta + \sum_\beta E_{\alpha\beta} \frac{\partial c_\beta}{\partial x} \qquad (4.74)$$

or

$$\boxed{\frac{\partial d_\alpha}{\partial x} = \sum_\beta B_{\alpha\beta} d_\beta + \sum_\beta D_{\alpha\beta} c_\beta + \sum_{\beta,\gamma} E_{\alpha\gamma} B_{\gamma\beta} c_\beta.} \qquad (4.75)$$

The first term on the r.h.s. of eq. (4.75) has the same matrix $B_{\alpha\beta}$ as the evolution equation of the primary field with d_β substituted for $c_\beta^{(0)}$. It can be interpreted as the coupling between the modes of the scattered field due to the deterministic heterogeneities (the range dependence of the reference structure). We will call it the *deterministic mode coupling* of the scattered field. The second term of eq. (4.75), on the other hand, has a new stochastic coupling matrix $D_{\alpha\beta}$ which relates d_α to c_β. It describes the coupling from the coherent field modes to the scattered field modes due to the stochastic boundary roughness, which will be called the *stochastic mode coupling* from the coherent field to the scattered field. The third term has both a stochastic coupling matrix $E_{\alpha\beta}$ and a deterministic coupling matrix $B_{\alpha\beta}$, which can be interpreted as the mixed interaction of the stochastic mode coupling after the deterministic mode coupling to the coherent field, i.e., the *mixed mode coupling* to the coherent field. The meaning of each term in eq. (4.75) and eq. (4.65) is illustrated by the diagrams in Fig. 4.4. Even though the matrices $D_{\alpha\beta}$ and $E_{\alpha\beta}$ are not the same, they are represented by the same symbol in Fig. 4.4 because they have similar interactions with the wavefield, i.e. converting the coherent field to the scattered field. The derivations of matrices $D_{\alpha\beta}$ and $E_{\alpha\beta}$ for Rayleigh waves in a 2-D isotropic medium are given in the appendix.

Also note that matrix $D_{\alpha\beta}$ will still contribute even in plane layered media if the

Figure 4.4: Schematic diagram notation for coupling matrices.

Diagram Notation

$\longrightarrow$ $\sim\!\!\sim\!\!\sim\!\!\sim\!\!\sim$

Deterministic
mode

Stochastically
scattered mode

●   □

$B_{\alpha\beta}$ $D_{\alpha\beta}, E_{\alpha\beta}$

Deterministic
interaction

Stochastic
interaction

- - - - - - - - - - - - - - - - - - - -

$\mathcal{O}(1)$:

c_β c_α

$B_{\alpha\beta}$

$\mathcal{O}(\varepsilon)$:

d_β d_α

$B_{\alpha\beta}$

c_β d_α $E_{\alpha\gamma}$

$D_{\alpha\beta}$ c_β c_γ d_α

$B_{\gamma\beta}$
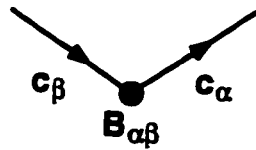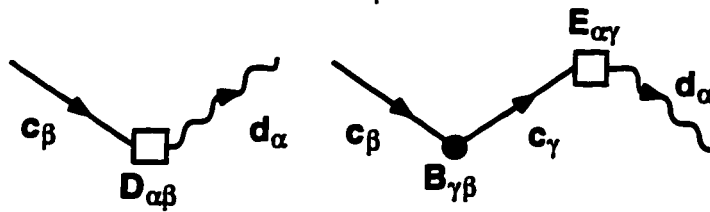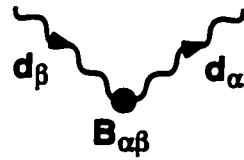
layer boundaries are rough:

$$\frac{\partial d_\alpha}{\partial x} = \sum_\beta D_{\alpha\beta} c_\beta, \tag{4.76}$$

where $h_n^0 = 0$ and

$$D_{\alpha\beta} = i \sum_n \gamma_n \left[\mathbf{u}^{\alpha*} \cdot \frac{\partial \mathbf{T}^\beta(\hat{\mathbf{z}})}{\partial z} \right]_n e^{i(k_\beta - k_\alpha)x} \quad \text{for plane layered media.} \tag{4.77}$$

The phase term for the range-independent medium replaces the phase integral in eq. (4.77). For rough but plane layered media, there is no coupling between the coherent field modes, or between the scattered field modes. There can be only coupling from the coherent field to the scattered field, i.e., stochastic coupling.

We have derived the spatial evolution equation for the coherent field and the scattered field from the $\mathcal{O}(\varepsilon)$ equation, and also show that the result from the $\mathcal{O}(1)$ equation is equivalent to the evolution equation for a deterministic range-dependent medium. The evolution equation (4.65) for the primary field and the evolution equation (4.75) for the coherent field and the scattered field are rewritten in matrix form:

$$\frac{\partial \mathbf{c}^{(0)}}{\partial x} = \mathbf{B}\mathbf{c}^{(0)}, \tag{4.78}$$

$$\frac{\partial \mathbf{d}}{\partial x} = \mathbf{B}\mathbf{d} + (\mathbf{D} + \mathbf{E}\mathbf{B})\mathbf{c}. \tag{4.79}$$

The matrices $\mathbf{B}$, $\mathbf{D}$ & $\mathbf{E}$ are $\nu \times \nu$ matrices of complex values, and $\mathbf{c}^{(0)}(x)$, $\mathbf{c}(x)$ & $\mathbf{d}(x)$ are $\nu \times 1$ column vectors in the local mode space, where ν is the appropriate number of modes required to accurately model the signal.

4.6 Coupled-Mode Propagator for the Deterministic Media

In earlier work, the invariant imbedding technique is employed to solve the evolution equation (4.78) for the primary field (Kennett 1984). It results in a set of coupled nonlinear differential equations (Riccati equations) containing the coefficient matrix $B_{\alpha\beta}$ which consists of the slowly varying amplitude and the rapidly varying phase. For numerical integration of coupled Riccati equations, the coefficient matrix must

be computed frequently because $B_{\alpha\beta}$ is rapidly varying. Especially when we use many sets of local modes for a strongly varying structure, the phase term will greatly decrease the efficiency and the stability of the computation (Park & Odom 1997a). In this section, we remove the phase factor and apply the product integral method of Gilbert & Backus (1966). This leads to a matrix form of the propagator that is numerically stable and computationally efficient.

4.6.1 Transformation of the evolution equation

To derive the propagator for the primary field, we proceed in the following manner. First, the matrix **B** is decomposed into the amplitude and the phase :

$$B_{\alpha\beta} \equiv i\hat{B}_{\alpha\beta}e^{i(\phi_\beta - \phi_\alpha)}, \tag{4.80}$$

where the matrix $\hat{B}_{\alpha\beta}$ is (eq. (17) of Maupin 1988)

$$\hat{B}_{\alpha\beta} = i < \mathbf{v}^\alpha, \frac{\partial \mathbf{v}^\beta}{\partial x} > + \sum_n h_n^0 \left[\mathbf{u}^{\alpha*} \mathbf{T}^\alpha(\hat{\mathbf{x}}) \right]_n. \tag{4.81}$$

The matrix $\hat{B}_{\alpha\beta}$ is Hermitian and contains only off-diagonal terms (eqs. (13) and (18) of Maupin 1988):

$$\hat{\mathbf{B}}^\dagger = \hat{\mathbf{B}}, \tag{4.82}$$

$$\hat{B}_{\alpha\beta} = 0 \quad \text{for} \quad \alpha = \beta. \tag{4.83}$$

Second, the modal amplitude coefficients $\mathbf{c}^{(0)}(x)$ can be transformed with the phase factor:

$$c_\alpha^{(0)} \equiv \hat{c}_\alpha^{(0)}e^{-i\phi_\alpha}. \tag{4.84}$$

Then the displacement-stress vector is rewritten as

$$\mathbf{v}_0^{(0)}(x;\omega) = \sum_\alpha \hat{c}_\alpha^{(0)}\mathbf{v}_\alpha^{(0)}(z;x,\omega). \tag{4.85}$$

In eq. (4.85), new coefficients $\hat{c}_\alpha^{(0)}$ implicitly include the phase varying factors. Substituting eqs. (4.80) & (4.84) into (4.78) yields a new transformed evolution equation

from which the rapidly varying phase factor has been excluded and the numerical computation can be made more stable:

$$\frac{\partial \hat{\mathbf{c}}^{(0)}}{\partial x} = i\mathbf{H}\hat{\mathbf{c}}^{(0)}, \tag{4.86}$$

where a new coupling matrix $\mathbf{H}$ is defined as

$$H_{\alpha\beta} \equiv i\left(K_{\alpha\beta} + \hat{B}_{\alpha\beta}\right) \quad \text{and} \quad K_{\alpha\beta} \equiv k_{\beta}\delta_{\alpha\beta}, \tag{4.87}$$

i.e.,

$$\mathbf{H} \equiv \begin{pmatrix} k_1 & \hat{B}_{12} & \cdots & \hat{B}_{1\nu} \\ \hat{B}_{21} & k_2 & \cdots & \hat{B}_{2\nu} \\ \vdots & \vdots & \ddots & \vdots \\ \hat{B}_{\nu 1} & \hat{B}_{\nu 2} & \cdots & k_\nu \end{pmatrix}. \tag{4.88}$$

Here, k_α denotes the wavenumber of the αth mode. The diagonal terms of the matrix $\mathbf{H}$ consist of the local wavenumbers and the off-diagonal terms are equal to the elements of the coupling matrix. The matrix $\mathbf{H}$ is a Hermitian matrix for the real eigenwavenumbers:

$$H_{\alpha\beta}^{\dagger} = (k_{\beta}\delta_{\alpha\beta} + \hat{B}_{\alpha\beta})^{\dagger} = k_{\beta}^{*}\delta_{\alpha\beta}^{\dagger} + \hat{B}_{\alpha\beta}^{\dagger} = k_{\beta}\delta_{\alpha\beta} + \hat{B}_{\alpha\beta} = H_{\alpha\beta}, \tag{4.89}$$

and the matrix $\hat{\mathbf{B}}$ is a function of the material properties, the slope, and the local modes without the phase:

$$H_{\alpha\beta} = H_{\alpha\beta}\left(\rho, v_P, v_S, \dot{h}_n^0, \mathbf{v}^\alpha, \mathbf{v}^\beta\right), \tag{4.90}$$

where dot represents $\frac{\partial}{\partial x}$, ρ is the density, v_P is the P wave speed, v_S is the S wave speed, h_n^0 is the boundary function of the nth reference boundary, and $\mathbf{v}^\alpha$ & $\mathbf{v}^\beta$ represent the local modes. The new transformed evolution equation (4.86), therefore, becomes a differential equation with slowly varying coefficient matrices.

4.6.2 Evolution operator for an infinitesimal interval

We seek an evolution operator, i.e., propagator which is defined as

$$\hat{c}^{(0)}(x) = U(x, x_0)\hat{c}^{(0)}(x_0). \tag{4.91}$$

Now let us calculate the evolution operator for eq. (4.86) between two points separated by dx. To do this, write eq. (4.86) in the form (Cohen-Tannoudji, Diu & Laloë 1977):

$$
\begin{aligned}
d\hat{c}^{(0)}(x) &= \hat{c}^{(0)}(x + dx) - \hat{c}^{(0)}(x) \\
&= i H \hat{c}^{(0)} \, dx
\end{aligned}
\tag{4.92}
$$

that is,

$$\hat{c}^{(0)}(x + dx) = \{I + iH(x)\,dx\}\,\hat{c}^{(0)}(x). \tag{4.93}$$

The evolution operator for the infinitesimal interval $[x, x + dx]$, *the infinitesimal evolution operator* can be obtained from eq. (4.93) and the definition (4.91):

$$U(x + dx, x) = I + iH(x)\,dx. \tag{4.94}$$

Since $H(x)$ is Hermitian, $U(x + dx, x)$ is unitary:

$$
\begin{aligned}
U^\dagger U &= (I + iH\,dx)^\dagger (I + iH\,dx) \\
&= I + i\left(H - H^\dagger\right) dx \\
&= I
\end{aligned}
\tag{4.95}
$$

It follows that $U(x, x_0)$ is also unitary since the interval $[x, x_0]$ can be divided into a very large number of infinitesimal intervals. A detailed proof will be given in Section 4.8.

4.6.3 Definition and properties of product integral

The product integral $\overset{\curlyvee}{\int}$, which was first introduced to the elastic wave propagation problem by Gilbert & Backus (1966), is used to represent the propagator of the local mode for the range-dependent medium. As the solution of the differential equation

$$\frac{\partial \tilde{\mathbf{P}}(x,a)}{\partial x} = i\mathbf{H}(x)\tilde{\mathbf{P}}(x,a),\tag{4.96}$$

the product integral is defined as

$$\begin{aligned}\tilde{\mathbf{P}}(x,a) &= \int_a^{\curlyvee x} \exp\{i\mathbf{H}(\xi)\}\,d\xi\\ &\equiv \lim_{L\to\infty} \prod_{l=1}^{L} \exp\{i\mathbf{H}(\xi_l)\,\zeta_l\}\end{aligned}\tag{4.97}$$

where the range interval (a,x) is divided into L parts, by introducing the mesh points $x_1 \le x_2 \le \cdots \le x_{L-1}$, $a \equiv x_0$ and $x \equiv x_L$. In the interval $x_{l-1} \le x \le x_l$, the intermediate point $\xi_l \equiv (x_{l-1}+x_l)/2$ and the length of the subinterval $\zeta_l \equiv x_l - x_{l-1}$, $l = 1, 2, \cdots, L$.

The product integral notation makes concise statements of rigorous results possible which otherwise would be cumbersome. We introduce some principal properties of the product integral (DeWitt-Morette, Maheshwari & Nelson 1979; Schulman 1981):

Property 1

$$\tilde{\mathbf{P}}(x,x) = \mathbf{I},\tag{4.98}$$

$$\tilde{\mathbf{P}}(x,y) = \left\{\tilde{\mathbf{P}}(y,x)\right\}^{-1}\tag{4.99}$$

Property 2

$$\frac{\partial \tilde{\mathbf{P}}(x,y)}{\partial x} = i\mathbf{H}(x)\tilde{\mathbf{P}}(x,y),\qquad \frac{\partial \tilde{\mathbf{P}}(x,y)}{\partial y} = -\tilde{\mathbf{P}}(x,y)i\mathbf{H}(y).\tag{4.100}$$

Property 3

$$\tilde{\mathbf{P}}(x,y) = \tilde{\mathbf{P}}(x,z)\tilde{\mathbf{P}}(z,y)\tag{4.101}$$

Property 4 In the case that $\mathbf{H}(x)$ and $\frac{\partial}{\partial x}\mathbf{H}(x)$ commute for every x such that $a < x < b$, then

$$\check{\mathbf{P}}(b,a) = \exp \int_a^b i\mathbf{H}(\xi)\, d\xi \qquad (4.102)$$

Property 5 (The sum rule). Let $\mathbf{P}_A(x,a) = \int_a^{\check{x}} \exp\{i\mathbf{A}(\xi)\}\, d\xi$, then

$$\int_a^{\check{x}} \exp\{i\mathbf{A}(\xi) + i\mathbf{B}(\xi)\}\, d\xi$$

$$= \mathbf{P}_A(x,a) \int_a^{\check{x}} \exp\left\{\mathbf{P}_A^{-1}(\xi,a)i\mathbf{B}(\xi)\mathbf{P}_A(\xi,a)\right\}\, d\xi, \qquad (4.103)$$

$$\int_a^{\check{x}} \exp\{i\mathbf{A}(\xi) + i\mathbf{B}(\xi)\}\, d\xi$$

$$= \int_a^{\check{x}} \exp\left\{\mathbf{P}_A(x,\xi)i\mathbf{B}(\xi)\mathbf{P}_A^{-1}(\xi,a)\right\}\, d\xi\, \mathbf{P}_A(x,a). \qquad (4.104)$$

From the definition and the properties of product integrals, several different forms of propagator can be defined. Each form emphasizes different aspects of propagation and allows different interpretation.

4.6.4 The first form of the propagator

We represent a propagator for a general range-dependent medium from the definition of the product integral following Gilbert & Backus (1966):

$$\check{\mathbf{P}}(x,x_s) \equiv \lim_{L \to \infty} \prod_{l=1}^{L} \{\mathbf{I} + i\mathbf{H}(\xi_l)\,\zeta_l\} \qquad \text{(the first form)}, \qquad (4.105)$$

where the range interval (x_s,x) is divided into L parts and $x_s \equiv x_0$ & $x \equiv x_L$. The coupling matrix $\mathbf{H}$ in eq. (4.105) consists of the matrices $\mathbf{K}$ and $\hat{\mathbf{B}}$. The off-diagonal matrix $\hat{\mathbf{B}}$ represents mode coupling between the different branches (i.e., intermode coupling) and the diagonal matrix $\mathbf{K}$ governs the phase variation of each mode. While the first form of the propagator allows only Born-approximation type first-order intermode coupling in each subinterval (see figure 3 of Marquering & Snieder 1995), it gives an exact solution with multiple coupling effects in total as the number of subintervals goes to infinity.

4.6.5 The second form of the propagator

According to our definition eq. (4.97), the propagator is written as

$$\tilde{\mathbf{P}}(x, x_s) = \lim_{L \to \infty} \prod_{l=1}^{L} \exp\left\{i\mathbf{H}(\xi_l)\zeta_l\right\} \tag{4.106}$$

Assuming that the slowly varying coefficient matrix $\mathbf{H}$ in a short subinterval is represented by the mean coefficient yields

$$\mathbf{H}(x) \simeq \mathbf{H}(\xi_l) \qquad \text{for} \qquad x_{l-1} \leq x \leq x_l, \tag{4.107}$$

Then, the $\prod$ approximant to the product integral (4.105) becomes (Gilbert & Backus 1966)

$$\tilde{\mathbf{P}}(x, x_s) \simeq \prod_{l=1}^{L} \exp\left\{i\mathbf{H}(\xi_l)\zeta_l\right\} \qquad \text{(the second form)}. \tag{4.108}$$

The propagator $\tilde{\mathbf{P}}$ in eq. (4.108) denotes all possible higher-order coupling along the same dispersion branch and between the different branches in each subinterval. Based on its properties, we call it the *coupled-mode propagator*. Also note that the coupled-mode propagator $\tilde{\mathbf{P}}$ governs both the amplitude and the phase of each mode.

4.6.6 The third form of the propagator

We can also express the coupled-mode propagator in another form by using the relation between the unitary operator and the Hermitian operator and the relation $\tan \frac{\theta}{2} = \frac{1}{i}\frac{e^{i\theta}-1}{e^{i\theta}+1}$ (Morse & Feshbach, 1953, Vol. I pp 84-85):

$$\tilde{\mathbf{P}}(x_r, x_s) = \frac{\mathbf{I} + i\mathbf{Z}}{\mathbf{I} - i\mathbf{Z}} \qquad \text{(the third form)}, \tag{4.109}$$

where the operator

$$\mathbf{Z}(x_r, x_s) = \tan\left\{\frac{1}{2}\sum_{l=1}^{L}(x_l - x_{l-1})\mathbf{H}(\xi_l)\right\}, \tag{4.110}$$

and $\mathbf{I}$ is the identity operator. If we consider the $\hat{c}(x_s)$ as an input and $\hat{c}(x_r)$ as an output, the operator $\mathbf{Z}$ can be interpreted as an impedance due to lateral heterogeneities located between x_s and x_r.

4.6.7 The fourth form of the propagator

From the definition eq. (4.97) and property 5. the sum rule eq. (4.103), the propagator is represented as

$$
\begin{aligned}
\tilde{\mathbf{P}}(x,x_s) &= \int_{x_s}^{\check{x}} \exp\{i\mathbf{H}(\xi)\}\,d\xi \\
&= \int_{x_s}^{\check{x}} \exp\{i\mathbf{K}(\xi) + i\hat{\mathbf{B}}(\xi)\}\,d\xi \\
&= \mathbf{P}_K(x,x_s)\int_{x_s}^{\check{x}} \exp\left\{\tilde{\mathbf{P}}_K^{-1}(\xi,x_s)i\hat{\mathbf{B}}(\xi)\tilde{\mathbf{P}}_K(\xi,x_s)\right\}\,d\xi, \quad (4.111)
\end{aligned}
$$

where

$$
\tilde{\mathbf{P}}_K(x,x_s) = \int_{x_s}^{\check{x}} \exp\{i\mathbf{K}(\xi)\}\,d\xi. \tag{4.112}
$$

Because the diagonal matrices $\mathbf{K}(x)$ and $\frac{\partial}{\partial x}\mathbf{K}(x)$ are commutative for every x, $\tilde{\mathbf{P}}_K$ can be rewritten by property 4 eq. (4.102):

$$
\tilde{\mathbf{P}}_K(x,x_s) = \exp\left\{i\int_{x_s}^{x}\mathbf{K}(\xi)\,d\xi\right\}, \tag{4.113}
$$

The propagator of eq. (4.111) becomes

$$
\tilde{\mathbf{P}}(x,x_s) = \exp\left\{i\int_{x_s}^{x}\mathbf{K}(\xi)\,d\xi\right\}\int_{x_s}^{\check{x}}\exp\{\mathbf{B}(\xi)\}\,d\xi \tag{4.114}
$$

where the following relation is used

$$
\begin{aligned}
&\left\{\tilde{\mathbf{P}}_K^{-1}(x,x_s)i\hat{\mathbf{B}}(x)\tilde{\mathbf{P}}_K(x,x_s)\right\}_{\alpha\beta} \\
&= \sum_{\gamma,\nu}\exp\left\{-i\int_{x_s}^{x}k_\alpha(\xi)\,d\xi\right\}\delta_{\alpha\gamma}\,i\hat{B}_{\gamma\nu}\exp\left\{i\int_{x_s}^{x}k_\nu(\xi)\,d\xi\right\}\delta_{\nu\beta} \\
&= i\hat{B}_{\alpha\beta}\exp\left\{i\int_{x_s}^{x}(k_\beta - k_\alpha(\xi))\,d\xi\right\} \\
&= B_{\alpha\beta}. \tag{4.115}
\end{aligned}
$$

By the definition of the product integral, the second term on the right hand side of eq. (4.115) is written as

$$
\int_{x_s}^{\check{x}}\exp\{\mathbf{B}(\xi)\}\,d\xi \approx \prod_{l=1}^{L}\exp\left\{\mathbf{B}(\xi_l)\,\zeta_l\right\}. \tag{4.116}
$$

Finally, the fourth form of the propagator becomes

$$\tilde{P}(x,x_s) \;=\; U^B(x_L,x_{L-1})U^K(x_L,x_{L-1}) \cdots$$

$$\times\, U^B(x_2,x_1)U^K(x_2,x_1)U^B(x_1,x_0)U^K(x_1,x_0)$$

(the fourth form),   (4.117)

where the operators U_K & U_K for the subinterval $[x_{l-1},x_l]$ are defined as

$$U^K(x_l,x_{l-1}) \;=\; \exp\left\{i\int_{x_{l-1}}^{x_l} K(\xi)\,d\xi\right\}$$ (4.118)

$$U^B(x_l,x_{l-1}) \;=\; \exp\left\{B(\xi_l)\,\zeta_l\right\}.$$ (4.119)

The operator $U^K(x_l,x_{l-1})$ represents the phase integral of each wavenumber in the subinterval, and the operator $U^B(x_l,x_{l-1})$ denotes the transition from one mode to another mode. It is computed from the lateral heterogeneities in the subinterval and applied at the end of each subinterval. The magnitude $U^B_{\alpha_1\alpha_2}(x_l,x_{l-1})$ is an amplitude for the transition from a mode α_1 to α_2, i.e., the transition amplitude. To interpret the product integral of the propagator we present a schematic figure showing two possible paths with fixed starting and ending point in wavenumber space in Fig. 4.5. The horizontal thick solid lines denote the phase integral and the vertical arrows represent the spectral transition.

The product integral representation for the propagator eq. (4.117) is very important, because it provides a clear physical picture of the mode coupling process when it is carefully interpreted. Mode coupling in a laterally heterogeneous medium is a continuous process. However, eq. (4.117) approximates the continuous process in the heterogeneous medium as a sequence of processes in homogeneous subintervals within which the infinitesimal evolution operators $U^{K,B}$ are defined. The evolution operator U^B allows for transitions (coupling) between modes with different local eigenwavenumbers (α say). The operator U^K is a diagonal operator of phase integrals of the form $\int_{x_{l-1}}^{x_l} ik_\alpha(\xi)\,d\xi$. Notice that the phase integral $\int_{x_s}^{x_r} ik(\xi)\,d\xi$ is a *functional* of the discrete wavenumber functions $k_\alpha(\xi)$, i.e., the value of the phase integral does

Figure 4.5: Two possible paths are shown with fixed starting and ending points in the discrete wavenumber space. The horizontal thick solid lines denote the phase integral $U^K(x_l, x_{l-1})$ and the vertical arrows represent the spectral transition $U^B(x_l, x_{l-1})$.

not depend on the intermediate variable ξ ($x_s < \xi < x_r$). Rather it dependends on the shape of the wavenumber function $k(\xi)$ and the endpoints (x_s, x_r). Because of the presence of mode coupling (transition) through the presence of the operator $\mathbf{U}^B$, the propagator $\tilde{\mathbf{P}}$ represents the phase integral computed along *all possible paths* in the discrete functional space of wavenumber $\int_{x_s}^{x_r} ik(\xi)\,d\xi$.

For a slowly varying structure, the coupling matrix $\hat{\mathbf{B}}$ may be disregarded, then the coupled-mode propagator becomes

$$
\begin{aligned}
\tilde{\mathbf{P}}(x, x_s) &= \lim_{L \to \infty} \prod_{l=1}^{L} \exp\left\{ \int_{x_{l-1}}^{x_l} i\mathbf{K}(\xi)\,d\xi \right\} \\
&= \exp\int_{x_s}^{x} \{ i\mathbf{K}(\xi)\,d\xi \}
\end{aligned}
\tag{4.120}
$$

The coupled-mode propagator of eq. (4.120) denotes the phase integral of each wavenumber from the source point to the receiver point without transition, i.e., the WKBJ approximation for surface waves (Woodhouse 1974):

4.6.8 The fifth form of the propagator

The improper eigenfunctions for the continuous spectrum have been derived for acoustic waves for a simple structure (Odom 1986) and for elastic waves for a general layered medium (Maupin 1996). In this subsection, we seek a form of the propagator appropriate for both discrete spectrum and continuous spectrum. The matrix multiplication of the coupled-mode propagator is done by summation over discrete eigenwavenumbers at each mesh point. The summation can be transformed to an integration, which will give an appropriate form of propagator for both discrete spectrum and continuous spectrum:

$$
\sum_{\alpha'} \left\{ \delta_{\alpha\alpha'} + i\delta_{\alpha\alpha'}k_{\alpha'}(\xi_l)\zeta_l + i\hat{B}_{\alpha\alpha'}(\xi_l)\zeta_l \right\}
$$

$$
\Longrightarrow \int \left\{ 1 + ik_l(x_l - x_{l-1}) + i\hat{B}(k_l, \frac{x_l + x_{l-1}}{2})(x_l - x_{l-1}) \right\} \, dk_l \delta(R(k_l)) ,
\tag{4.121}
$$

where the scalar function $\hat{B}(k_l)\, dk_l \equiv \hat{B}_{\alpha\alpha'}(\frac{x_l + x_{l-1}}{2})$, and $k_\alpha \equiv k_l$ & $k_{\alpha'} \equiv k_l + dk_l$. The term $\int dk_l\, \delta(R(k_l)) \cdot$ represents the integration over the discrete solutions of the dispersion equation. The matrix summation or integration in eq. (4.121) is non-vanishing only for wavenumbers k_l satisfying the dispersion relation $R(k_l)$. This is the reason for the presence of the δ function with $R(k_l)$ as its argument. The dispersion function $R(k_l)$ becomes the Rayleigh function for Rayleigh waves. Then, the first form of the propagator (4.105) is represented by integrations over continuous wavenumber space:

$$
\begin{aligned}
\tilde{\mathbf{P}}(x, x_s) &= \lim_{L \to \infty} \int \prod_{l=1}^{L} dk_l\, \delta(R(k_l)) \left\{ 1 + ik_l(x_l - x_{l-1}) + i\hat{B}(k_l)(x_l - x_{l-1}) \right\} \\
&= \lim_{L \to \infty} \int \prod_{l=1}^{L} dk_l\, \delta(R(k_l)) \exp\left\{ ik_l(x_l - x_{l-1}) + i\hat{B}(k_l)(x_l - x_{l-1}) \right\} \\
&= \lim_{L \to \infty} \int \prod_{l=1}^{L} dk_l\, \delta(R(k_l)) \\
&\quad \times \exp\left\{ \sum_{l=1}^{L} \left[ik_l(x_l - x_{l-1}) + i\hat{B}(k_l)(x_l - x_{l-1}) \right] \right\}.
\end{aligned}
\tag{4.122}
$$

To convert the propagator for both the continuous and discrete spectrum, first, the dispersion function is dropped. The continuous spectrum represents waves radiating away as body waves while the discrete spectrum represents waves trapped in the waveguide. The propagation direction of the discrete spectrum is horizontal. The continuous spectrum propagates along an arbitrary ray path (i.e., $z = z(x)$ in 2-D). Therefore, the propagator is a functional of the ray path (i.e., $z = z(x)$) as well as wavenumber (or horizontal slowness), i.e., $\tilde{\mathbf{P}} = \tilde{\mathbf{P}}[z(x), k(x)]$. The propagator $\tilde{\mathbf{P}}(x_r, x_s)$ does not depend on the variable x such that $x_s < x < x_r$, but it depends on the shape of the wavenumber function $k(x)$ and the shape of the ray path $z(x)$ in the interval $[x_s, x_r]$. While depth integration for $\hat{B}(k_l) = \int \hat{b}(k_l, z)\, dz$ is separately done for a discrete spectrum, path integral (functional integration) should be applied for a continuous spectrum in a range-dependent medium. Imagine that the points $z_s, z_1, \ldots, z_{L-1}, z$ are connected by lines, where $z_l = z(x_l)$. An integral along that

path can be represented as a Riemann integral, i.e.,

$$\exp\left\{\int \hat{b}(z)\,dz\right\}$$

$$\Rightarrow \exp\left\{\int_{x_s}^{x} \hat{b}(z)\left(\frac{dz}{dx}\right)dx\right\}$$

$$\sim \int \prod_{l=1}^{L-1} dz_l \, \exp\left\{\sum_{l=1}^{L}\left[\hat{b}(\frac{z_l+z_{l-1}}{2})\left(\frac{z_l-z_{l-1}}{x_l-x_{l-1}}\right)\right](x_l-x_{l-1})\right\}. \quad (4.123)$$

The propagator for both continuous and discrete spectrum becomes

$$\tilde{\mathbf{P}}(x,x_s) =$$

$$\lim_{L\to\infty}\int \prod_{l=1}^{L-1} dz_l \prod_{l=1}^{L} dk_l$$

$$\times \exp\left\{\sum_{l=1}^{L}\left[ik_l(x_l-x_{l-1})+i\hat{b}(k_l,\frac{z_l+z_{l-1}}{2})(z_l-z_{l-1})\right]\right\}$$

(the fifth form). $\quad\quad(4.124)$

The summation for the dz is done from 1 to $L-1$ with the assumption that the source point $z_s = z(x_0)$ and the receiver point $z_r = z(x_L)$ are fixed while only the initial value of the wavenumber function is assumed known. The propagator of eq. (4.124) has the form of a phase space path integral (Schulman 1981). While the wavenumber jumps at each mesh point with some transition amplitude, the ray path is stepwise continuous from subinterval to subinterval. For a weakly range-dependent medium, by applying the variational principle to

$$T = \int_{x_0}^{x} \mathbf{H}(k,z,x)\,dx, \quad\quad (4.125)$$

the phase term can be numerically integrated along the Fermat path (classical approximation).

4.6.9 The solution for the primary field

In terms of the coupled-mode propagator eq. (4.108), the solution of the evolution equation (4.78) is represented as

$$\hat{\mathbf{c}}^{(0)}(x) = \tilde{\mathbf{P}}(x,x_s)\hat{\mathbf{c}}^{(0)}(x_s), \quad\quad (4.126)$$

Hence, we obtain the solution of the displacement-stress vector of the primary field:

$$
\begin{aligned}
\mathbf{v}_0^{(0)}(x_r, z_r; \omega) &= \sum_\alpha \mathbf{v}^\alpha(z_r; x_r, \omega) \sum_\beta \tilde{P}_{\alpha\beta}(x_r, x_s) \hat{c}_\beta^{(0)}(x_s) \\
&= \sum_{\alpha,\beta} \mathbf{v}^\alpha(z_r; x_r, \omega) \left\{ \prod_{l=L}^{1} \exp[i\mathbf{H}(x_l - x_{l-1})] \right\}_{\alpha\beta} \\
&\quad \times \mathbf{u}^{\beta*}(z_s; x_s) \cdot \mathbf{f}^s e^{i\frac{\pi}{2}},
\end{aligned}
\tag{4.127}
$$

where the source point $x_s \equiv x_0$ and the receiver point $x_r \equiv x_L$. The initial condition for the transformed amplitude coefficients $\hat{c}(x_s)$ is also used:

$$
\hat{c}_\alpha^{(0)}(x_s) = c_\alpha^{(0)}(x_s) e^{i\phi_\alpha(x_s)} = c_\alpha^{(0)}(x_s) = \mathbf{u}^{\alpha*}(z_s; x_s) \cdot \mathbf{f}^s e^{i\frac{\pi}{2}}
\tag{4.128}
$$

4.6.10 Transformation of the evolution equation for the $\mathcal{O}(\varepsilon)$ system

The rapidly varying phase factor is excluded from the evolution equation for the $\mathcal{O}(\varepsilon)$ system eq. (4.79) by transforming the modal amplitudes of the coherent field and the scattered field:

$$
c_\alpha \equiv \hat{c}_\alpha e^{-i\phi_\alpha},
\tag{4.129}
$$

$$
d_\alpha \equiv \hat{d}_\alpha e^{-i\phi_\alpha},
\tag{4.130}
$$

and decomposing the matrices $\mathbf{D}$ and $\mathbf{E}$ into the amplitude factors and the phase factors:

$$
D_{\alpha\beta} \equiv \hat{D}_{\alpha\beta} e^{i(\phi_\beta - \phi_\alpha)}
\tag{4.131}
$$

$$
E_{\alpha\beta} \equiv \hat{E}_{\alpha\beta} e^{i(\phi_\beta - \phi_\alpha)}
\tag{4.132}
$$

The transformed evolution equation for the scattered field can be obtained by substituting eqs. (4.80), (4.84), (4.129), (4.130), (4.131) & (4.132) into eq. (4.79):

$$
\frac{\partial \hat{\mathbf{d}}}{\partial x} = i\mathbf{H}\hat{\mathbf{d}} + \left(\hat{\mathbf{D}} + i\hat{\mathbf{E}}\hat{\mathbf{B}} \right) \hat{\mathbf{c}}.
\tag{4.133}
$$

The second term on the r.h.s. of eq. (4.133) represents the excitation of the scattered field from scattering of the coherent field, i.e., eq. (4.133) is an inhomogeneous equation. The propagator can also be used to solve the system with a source:

$$\hat{\mathbf{d}}(x) = \tilde{\mathbf{P}}(x, x_0)\hat{\mathbf{d}}(x_0) + \int_{x_0}^{x} \tilde{\mathbf{P}}(x, \xi)\mathbf{g}(\xi)d\xi, \tag{4.134}$$

where the source term is

$$\begin{aligned} \mathbf{g}(x) &= \mathbf{S}(x)\,\hat{\mathbf{c}}(x) \\ &= \left(\hat{\mathbf{D}} + i\hat{\mathbf{E}}\hat{\mathbf{B}}\right)\hat{\mathbf{c}}(x). \end{aligned} \tag{4.135}$$

The source term $\mathbf{g}(x)$ in eq. (4.134) can be interpreted as the *stochastic effective source* of the scattered field, which represents the excitation of the scattered field due to the the coherent field scattered from the stochastic roughness located at x. The transformed evolution equation (4.134) for the $\mathcal{O}(\varepsilon)$ system will be used to derive the integral equation for the propagator in the $\mathcal{O}(\varepsilon)$ stochastic medium in section 9.

4.7 The Unitarity of the Coupled-mode Propagator and the Reciprocity Theorem

While $\mathbf{B}$ is anti-Hermitian, i.e., $\mathbf{B}^\dagger = -\mathbf{B}$ (Maupin 1988), $\mathbf{H}$ is Hermitian (eq. (4.89)). From the Hermiticity of $\mathbf{H}$, we show directly that the coupled-mode propagator $\tilde{\mathbf{P}}$ is unitary using the second form eq. (4.108):

$$\begin{aligned} \tilde{\mathbf{P}}^\dagger(x, x_s) &= \left\{ e^{i\mathbf{H}(x-x_{L-1})}e^{i\mathbf{H}(x_{L-1}-x_{L-2})}\cdots e^{i\mathbf{H}(x_2-x_1)}e^{i\mathbf{H}(x_1-x_0)} \right\}^\dagger \\ &= e^{-i\mathbf{H}^\dagger(x_1-x_0)}e^{-i\mathbf{H}^\dagger(x_2-x_1)}\cdots e^{-i\mathbf{H}^\dagger(x_{L-1}-x_{L-2})}e^{-i\mathbf{H}^\dagger(x-x_{L-1})} \\ &= e^{i\mathbf{H}(x_0-x_1)}e^{i\mathbf{H}(x_1-x_2)}\cdots e^{i\mathbf{H}(x_{L-2}-x_{L-1})}e^{i\mathbf{H}(x_{L-1}-x)} \\ &= \tilde{\mathbf{P}}(x_s, x) \\ &= \tilde{\mathbf{P}}^{-1}(x, x_s). \end{aligned} \tag{4.136}$$

The last step in eq.(4.136) follows from property 1 eq. (4.99) of the product integral. The definition of unitarity is that

$$\tilde{\mathbf{P}}^{\dagger}(x, x_s) = \tilde{\mathbf{P}}^{-1}(x, x_s).$$

(4.137)

A unitary transformation is a generalization of an orthogonal transformation to a complex space. Rotation matrices are well known examples of orthogonal transformations. When we consider the propagation from x_s to x in the deterministic range-dependent medium, the unitary propagator can be thought of as performing a rotation in the local mode space with the rotation operator $\tilde{\mathbf{P}}(x, x_s)$. The deterministic modal amplitude coefficient $c_{\alpha}^{(0)}(x)$ in eq. (4.126) after the propagation can be interpreted as a new coordinate component of the primary field vector $\mathbf{v}^{(0)}(x_s)$ after the rotation in the local mode space. The operator $\tilde{\mathbf{P}}(x, x_s)$ rotates the vector $c_{\alpha}^{(0)}(x_s)$ to $c_{\alpha}^{(0)}(x)$ in the local mode space, where $c_{\alpha}^{(0)}(x_s)$ and $c_{\alpha}^{(0)}(x)$ are the abstract vector representations of the primary field $\mathbf{v}^{(0)}(x_s)$ and $\mathbf{v}^{(0)}(x)$. Therefore, the norm of the primary field vector is a propagation invariant for the deterministic range dependent medium (i.e., the $\mathcal{O}(1)$ system, when $\gamma(x) = 0$).

$$
\begin{aligned}
\|\mathbf{v}_0^{(0)}(x)\|^2 &= \ <\mathbf{v}_0^{(0)}(x), \mathbf{v}_0^{(0)}(x)> \\
&= \sum_{\alpha,\beta} <\hat{c}_{\beta}^{(0)}(x)\mathbf{v}^{\beta}, \hat{c}_{\alpha}^{(0)}(x)\mathbf{v}^{\alpha}> \\
&= \sum_{\alpha,\beta} \hat{c}_{\beta}^{(0)\,*}(x)\hat{c}_{\alpha}^{(0)}(x) <\mathbf{v}^{\beta}, \mathbf{v}^{\alpha}> \\
&= \sum_{\alpha,\beta} \hat{c}_{\beta}^{(0)\,*}(x)\hat{c}_{\alpha}^{(0)}(x)\delta_{\alpha\beta} \\
&= \sum_{\alpha} |\hat{c}_{\alpha}^{(0)}(x)|^2 \\
&= \sum_{\alpha} |\hat{c}_{\alpha}^{(0)}(x_s)|^2 \\
&= \|\mathbf{v}_0(x_s)\|^2,
\end{aligned}
$$

(4.138)

where the orthogonality of the local modes and the unitarity of the coupled-mode

propagator are used:

$$
\begin{aligned}
\sum_\alpha |\hat{c}_\alpha^{(0)}(x)|^2 &= \hat{c}^{(0)\dagger}(x)\hat{c}^{(0)}(x) \\
&= \hat{c}^{(0)\dagger}(x_s)\tilde{\mathbf{P}}^\dagger(x,x_s)\tilde{\mathbf{P}}(x,x_s)\hat{c}^{(0)}(x_s) \\
&= \hat{c}^{(0)\dagger}(x_s)\tilde{\mathbf{P}}^{-1}(x,x_s)\tilde{\mathbf{P}}(x,x_s)\hat{c}^{(0)}(x_s) \\
&= \hat{c}^{(0)\dagger}(x_s)\hat{c}^{(0)}(x_s) \\
&= \sum_\alpha |\hat{c}_\alpha^{(0)}(x_s)|^2.
\end{aligned}
\tag{4.139}
$$

Eq. (4.139) represents the conservation of the total energy for the $\mathcal{O}(1)$ system (the deterministic model). The local modes are assumed to be normalized to carry the same unit energy. Note that the propagation invariant and the energy conservation are for the primary field of the deterministically range dependent elastic medium. For the stochastic model, the condition for the total energy conservation should include the effect of the energy conversion between the coherent field and the scattered field, i.e., the generation of the scattered field should be related to the loss of the coherent field. This problem is detailed in the following section.

For the case of the amplitude coefficients $\hat{d}_\alpha(x)$ of the scattered field from the rough-surface scattering, the situation is slightly different. The integral term in eq.(4.134) corresponds to a translation in the local mode space. The new $\hat{d}_\alpha(x)$ after propagation is a combination of a rotation and a translation. Therefore, the length of the scattered field vector is no longer invariant. Here, the rotation is due to the deterministic mode coupling and the translation is due to the rough-surface scattering, so the change of energy of the scattered field is governed by the rough-surface scattering (the stochastic mode coupling).

The reciprocity theorem for the deterministic range-dependent medium can be written in terms of the coupled-mode propagator from its unitarity (Morse & Feshbach 1953, Vol. I p 84):

$$
\tilde{\mathbf{P}}^\dagger(x_2, x_1) = \tilde{\mathbf{P}}(x_1, x_2),
\tag{4.140}
$$

Eq. (4.140) means that if a local-mode decomposion of the source c_α^0 applied at $x = x_1$ evolves to the modal amplitude c_α measured at $x = x_2$, then the same decomposion c_α^0 when applied at $x = x_2$ will evolve to the modal amplitude which is measured c_α at $x = x_1$. It is the reciprocity relation for surface waves including mode coupling. That reciprocity theorem does not imply that a source at x_2 yields the same response at x_1 as a source at x_1 produces at x_2 because of the difference between the local modes at x_1 and x_2.

Numerical operations with unitary matrices are particularly efficient and stable, because numerical inversion is accomplished merely by taking the adjoint.

4.8 Mean and Covariance of the Propagator for the $\mathcal{O}(\varepsilon)$ System

4.8.1 Energy conservation for the $\mathcal{O}(\varepsilon)$ system

In the preceding section, the energy consevation for the purely deterministic model is demonstrated from the unitarity of the coupled-mode propagator for the deterministic medium. In this subsection, we present the condition for total energy conservation for the first-order stochastic perturbation, $\mathcal{O}(\varepsilon)$ system (eq. (4.28)). The mode amplitude of the coherent field are derived in terms of the coupled-mode propagator from the energy conservation condition and the mode amplitude of the scattered field,

$$\mathbf{\hat{d}}(x) = \mathbf{\check{P}}(x, x_0)\mathbf{\hat{d}}(x_0) + \int_{x_0}^{x} \mathbf{\check{P}}(x, \xi)\mathbf{S}(\xi)\mathbf{\hat{c}}(\xi)\,d\xi. \tag{4.141}$$

The norm of the sum of the coherent field and the scattered field in the local mode space must be a propagation invariant in order that the total energy for the $\mathcal{O}(\varepsilon)$ system is conserved. Let $\mathbf{a}$ be a vector defined in the local mode space such that

$$\mathbf{a}(x) = \mathbf{\hat{c}}(x) + \mathbf{\hat{d}}(x). \tag{4.142}$$

Then, the condition for the total energy conservation of the $\mathcal{O}(\varepsilon)$ system is

$$\mathbf{a}(x_0) = \mathbf{\hat{c}}^{(0)}(x_0). \tag{4.143}$$

$$\mathbf{a}(x) = \mathbf{\check{P}}(x, x_0)\mathbf{a}(x_0). \tag{4.144}$$

The total energy conservation condition eqs. (4.143) & (4.144) for the $\mathcal{O}(\varepsilon)$ stochastic medium can be rewritten as

$$\hat{c}^{(0)}(x) = \hat{c}(x) + \hat{d}(x).$$ (4.145)

Substituting eqs. (4.141) & (4.142) into eq. (4.144) yields the formula for the coherent modal amplitude $\hat{c}(x)$:

$$\hat{c}(x) = \tilde{P}(x, x_0)\hat{c}(x_0) - \int_{x_0}^{x} \tilde{P}(x, \xi) S(\xi) \hat{c}(x) \, d\xi.$$ (4.146)

4.8.2   The Lippmann-Schwinger integral equation for the $\mathcal{O}(\varepsilon)$ propagator

First, we shall define the propagator for the stochastic medium with the $\mathcal{O}(\varepsilon)$ perturbation:

$$\hat{c}(x) = \tilde{\mathcal{P}}(x, x_0)\hat{c}(x_0) \qquad \text{for the } \mathcal{O}(\varepsilon) \text{ system,}$$ (4.147)

while the coupled-mode propagator for the deterministic medium is

$$\hat{c}^{(0)}(x) = \tilde{P}(x, x_0)\hat{c}^{(0)}(x_0) \qquad \text{for the } \mathcal{O}(1) \text{ system.}$$ (4.148)

Substituting the propagator for the $\mathcal{O}(\varepsilon)$ system eq. (4.147) into the evolution equation (4.144) yields

$$\boxed{\tilde{\mathcal{P}}(x, x_0) = \tilde{P}(x, x_0) - \int_{x_0}^{x} \tilde{P}(x, \xi) S(\xi) \tilde{\mathcal{P}}(\xi, x_0) \, d\xi}$$ (4.149)

The equation (4.149) is an integral equation for the $\mathcal{O}(\varepsilon)$ propagator $\tilde{\mathcal{P}}$. The integral equation is formally equivalent to *the Lippmann-Schwinger integral equation* used in quantum mechanics to describe scattering from a potential. For the case of rough surface scattering, DeSanto & Brown (1986) also arrived at a Lippmann-Schwinger type integral equation from the Fourier transformed integral equation for the scattered part of the Green's function. Note that eq. (4.149) includes a scattering operator $S(x)$ instead of the scalar function for random fluctuations commonly included in the Lippmann-Schwinger integral equation for scalar wave (or potential) scattering. To

solve the Lippmann-Schwinger equation by formal perturbation series (or successive approximation) (Frisch 1968; Morse & Feshbach 1953), Eq. (4.149) is rewritten as

$$\check{\mathcal{P}} = \check{\mathbf{P}} - \check{\mathbf{P}} L_1 \check{\mathcal{P}},$$ (4.150)

where L_1 is the random operator, defined such that

$$L_1 \check{\mathbf{P}} = \int_{x_0}^{x} \mathbf{S}(\xi)\, \check{\mathbf{P}}(\xi, x_0)\, d\xi.$$ (4.151)

Eq. (4.150) is solved for $\check{\mathcal{P}}$ by formal iteration:

$$\begin{aligned}
\check{\mathcal{P}} &= \left(I + \check{\mathbf{P}} L_1\right)^{-1} \check{\mathbf{P}} \\
&= \sum_{n=0}^{\infty} \left(-\check{\mathbf{P}} L_1\right)^{n} \check{\mathbf{P}}
\end{aligned}$$ (4.152)

The formal perturbation series solution of the propagator for the $\mathcal{O}(\varepsilon)$ system is written as

$$\begin{aligned}
\check{\mathcal{P}}(x, x_0) =& \\
& \check{\mathbf{P}}(x, x_0) - \int_{x_0}^{x} \check{\mathbf{P}}(x, \xi_1) \mathbf{S}(\xi_1) \check{\mathbf{P}}(\xi_1, x_0)\, d\xi_1 \\
& + (-1)^2 \int_{x_0}^{x} \check{\mathbf{P}}(x, \xi_2) \mathbf{S}(\xi_2) \check{\mathbf{P}}(\xi_2, \xi_1) \mathbf{S}(\xi_1) \check{\mathbf{P}}(\xi_1, x_0)\, d\xi_1\, d\xi_2 \\
& + (-1)^3 \int_{x_0}^{x} \check{\mathbf{P}}(x, \xi_3) \mathbf{S}(\xi_3) \check{\mathbf{P}}(\xi_3, \xi_2) \mathbf{S}(\xi_2) \check{\mathbf{P}}(\xi_2, \xi_1) \\
& \times \mathbf{S}(\xi_1) \check{\mathbf{P}}(\xi_1, x_0)\, d\xi_1\, d\xi_2\, d\xi_3
\end{aligned}$$ (4.153)

$$\cdots,$$

where $\check{\mathbf{P}}$ is the coupled-mode propagator for the range-dependent medium in the absence of the stochastic roughness ($\gamma(x) = 0$). The operator $\mathbf{S}$ represents rough surface scattering at x, i.e., it converts the coherent field $\hat{c}$ to the scattered field $\hat{d}$. The matrix representation of the scattering operator $\mathbf{S}$ is derived for Rayleigh waves in an isotropic medium in the appendix. Note that retaining the first two terms on the right hand side of eq. (4.153) is the Born approximation for $\check{\mathbf{P}}(x, x_0)$ (the single scattering approximation). The averaged quantity of the Born approximation

vanishes for the centered random fluctuation. On the other hand, averaging the formal perturbation series eq. (4.153) yields the nonvanishing mean propagator $\left\langle \tilde{\mathcal{P}} \right\rangle_E$, which can be related to the mean coherent field, i.e., the mean field:

$$
\begin{aligned}
\left\langle \mathsf{v}_0^{(1)}(x_r) \right\rangle_E &= \sum_\alpha \left\langle \mathsf{v}^\alpha \left\{ \hat{\mathsf{c}}(x) \right\}_\alpha \right\rangle_E \\
&= \sum_\alpha \mathsf{v}^\alpha \left\{ \left\langle \tilde{\mathcal{P}}(x_r, x_s) \hat{\mathsf{c}}(x_s) \right\rangle_E \right\}_\alpha \\
&= \sum_\alpha \mathsf{v}^\alpha \left\{ \left\langle \tilde{\mathcal{P}}(x_r, x_s) \right\rangle_E \hat{\mathsf{c}}(x_s) \right\}_\alpha
\end{aligned}
\tag{4.154}
$$

The mean field of eq. (4.154), including the effects of multiple scattering, enables us to generate signal spectra and to predict the amplitude and the phase fluctuations of each mode.

Frisch (1968) derived the Dyson equation for the ensemble averaged Green's function for scalar wave scattering by diagram methods. However, the formal series solution of the propagator, eq. (4.153) includes the scattering operator $\mathsf{S}(x)$ instead of a scalar random function. To derive the mean propagator, we need to express the explicit correlation relations between values of the scattering operator at different points. Because the scattering operator $\mathsf{S}(x)$ is linearly dependent on the random roughness function $\gamma(x)$, we can decompose the random operator $\mathsf{S}(x)$ into a product of the centered stochastic process $\gamma(x)$ and the deterministic operator $\hat{\mathsf{S}}$. The averaged quantities of the centered random operator S, $\left\langle \mathsf{S}(x_1)\mathsf{S}(x_2)\cdots\mathsf{S}(x_l) \right\rangle_E$, also depend on the configuration of the points $x_1, x_2, \ldots, x_l$ in the same way as the averaged quantities of the random function $\gamma(x)$. Then, by means of the cluster expansions of the stochastic process $\gamma(x)$ eq. (4.3), we can also expand the averaged quantities of the random operator $\mathsf{S}(x)$ in the following cluster expansions:

$$
\begin{aligned}
\left\langle \mathsf{S}(x_1)\mathsf{S}(x_2) \right\rangle_E &= \Gamma_2(x_1, x_2)\,\hat{\mathsf{S}}(x_1)\,\hat{\mathsf{S}}(x_2) \\
\left\langle \mathsf{S}(x_1)\mathsf{S}(x_2)\mathsf{S}(x_3) \right\rangle_E &= \Gamma_3(x_1, x_2, x_3)\,\hat{\mathsf{S}}(x_1)\,\hat{\mathsf{S}}(x_2)\,\hat{\mathsf{S}}(x_3) \\
\left\langle \mathsf{S}(x_1)\mathsf{S}(x_2)\mathsf{S}(x_3)\mathsf{S}(x_4) \right\rangle_E &= \{ \Gamma_2(x_1, x_2)\,\Gamma_2(x_3, x_4) + \Gamma_2(x_1, x_3)\,\Gamma_2(x_2, x_4) \\
&\quad + \Gamma_2(x_1, x_4)\,\Gamma_2(x_2, x_3) + \Gamma_4(x_1, x_2, x_3, x_4) \}
\end{aligned}
$$

$$\times \, \hat{S}(x_1) \, \hat{S}(x_2) \, \hat{S}(x_3) \, \hat{S}(x_4)$$

$$\vdots \tag{4.155}$$

The summation over interfaces should be done for the cluster expansion eq. (4.155) when the model includes multiple rough interfaces. Note that, unlike the random scalar function, the scattering operator $\hat{S}$ and the propagator $\tilde{P}$ must be ordered for the averaged quantity. Averaging the formal series eq. (4.153) yields the expression for the mean propagator $\left\langle \tilde{P} \right\rangle_E$ in terms of the cluster expansions of the random operator $S(x)$:

$$
\begin{aligned}
\left\langle \tilde{P}(x, x_0) \right\rangle_E = \, & \\
& \tilde{P}(x, x_0) \\
& + (-1)^2 \int_{x_0}^{x} \tilde{P}(x, \xi_2) \hat{S}(\xi_2) \tilde{P}(\xi_2, \xi_1) \hat{S}(\xi_1) \tilde{P}(\xi_1, x_0) \, \Gamma_2(\xi_1, \xi_2) d\xi_1 \, d\xi_2 \\
& + (-1)^3 \int_{x_0}^{x} \tilde{P}(x, \xi_3) \hat{S}(\xi_3) \tilde{P}(\xi_3, \xi_2) \hat{S}(\xi_2) \tilde{P}(\xi_2, \xi_1) \\
& \qquad \times \hat{S}(\xi_1) \tilde{P}(\xi_1, x_0) \, \Gamma_3(\xi_1, \xi_2, \xi_3) d\xi_1 \, d\xi_2 \, d\xi_3 \\
& + (-1)^4 \int_{x_0}^{x} \tilde{P}(x, \xi_4) \hat{S}(\xi_4) \tilde{P}(\xi_4, \xi_3) \hat{S}(\xi_3) \tilde{P}(\xi_3, \xi_2) \\
& \qquad \times \hat{S}(\xi_2) \tilde{P}(\xi_2, \xi_1) \, \hat{S}(\xi_1) \tilde{P}(\xi_1, x_0) \left\{ \Gamma_2(\xi_1, \xi_2) \Gamma_2(\xi_3, \xi_4) \right. \\
& \qquad \left. + \Gamma_2(\xi_1, \xi_3) \Gamma_2(\xi_2, \xi_4) + \Gamma_2(\xi_1, \xi_4) \Gamma_2(\xi_2, \xi_3) \Gamma_4(\xi_1, \xi_2, \xi_3, \xi_4) \right\} \\
& \qquad d\xi_1 \, d\xi_2 \, d\xi_3 \, d\xi_4
\end{aligned}
$$

$$\cdots, \tag{4.156}$$

Note that averaging the second term on the right hand side of eq. (4.153) vanishes for the centered random operator, i.e., $\langle S(x) \rangle_E = 0$. For the centered Gaussian stochastic process $\gamma(x)$, all statistical moments of odd order vanish, and statistical moments of order $2n$ can be written as sums of $\frac{(2n)!}{2^n n!}$ terms, each of which is a product of two-point correlation functions. Then the mean propagator becomes

$$\left\langle \tilde{P}(x, x_0) \right\rangle_E = $$

$$\tilde{\mathbf{P}}(x, x_0)$$

$$+ \int_{x_0}^{x} \tilde{\mathbf{P}}(x, \xi_2)\hat{\mathbf{S}}(\xi_2)\tilde{\mathbf{P}}(\xi_2, \xi_1)\hat{\mathbf{S}}(\xi_1)\tilde{\mathbf{P}}(\xi_1, x_0)\, \Gamma_2(\xi_1, \xi_2)d\xi_1\, d\xi_2$$

$$+ \int_{x_0}^{x} \tilde{\mathbf{P}}(x, \xi_4)\hat{\mathbf{S}}(\xi_4)\tilde{\mathbf{P}}(\xi_4, \xi_3)\hat{\mathbf{S}}(\xi_3)\tilde{\mathbf{P}}(\xi_3, \xi_2)$$

$$\times\, \hat{\mathbf{S}}(\xi_2)\tilde{\mathbf{P}}(\xi_2, \xi_1)\, \hat{\mathbf{S}}(\xi_1)\tilde{\mathbf{P}}(\xi_1, x_0)$$

$$\times\, \left\{\Gamma_2(\xi_1, \xi_2)\Gamma_2(\xi_3, \xi_4) + \Gamma_2(\xi_1, \xi_3)\Gamma_2(\xi_2, \xi_4) + \Gamma_2(\xi_1, \xi_4)\Gamma_2(\xi_2, \xi_3)\right\}$$

$$d\xi_1\, d\xi_2\, d\xi_3\, d\xi_4$$

$$\cdots, \tag{4.157}$$

4.8.3 The diagram method and the Dyson equation for the mean propagator

To give a graphic idea of the structure of the expansions eqs. (4.156) & (4.157), we represent their elements by Feynman diagrams. The diagram method was introduced by Feynman to quantum electrodynamics to provide a simple way for handling all-order formal perturbation series of the Green's function including the effect of the scattering potential. The method owes its success to its compact form as compared to the analytical representation. We will apply the diagram methods to our formal perturbation series of the propagator which is operating on the abstract vector representations of the wavefields defined in the local mode space.

We point out that the following diagram representation is a calculation tool, and not just a graphical representation of the equations. Diagrams can be manipulated by well defined rules based on their topology. The diagram method allows us to represent the terms in equations for the mean and covariance of the propagator in the form of an integral equation with a kernel, which would be extremely difficult to do using ordinary analytical methods.

The diagram method can be introduced in a very elementary way. Following Frisch (1968), Bass & Fuks (1979) and Rytov, Kravtsov & Tatarski (1989), the diagram method for the propagator $\tilde{\mathcal{P}}$ is developed. First, the following connection is introduced for the representation of bare diagrams (Frisch 1968; Rytov et al. 1989):

1. The propagator for the deterministic medium (the deterministic propagator) is represented by a thin solid line:

$$\tilde{\mathbf{P}}(x,x_0) = \quad x\overline{}x_0 \qquad (4.158)$$

2. The random operator $(-L_1)$ is represented by a dot:

$$-L_1 = \quad \bullet \qquad (4.159)$$

Then, the perturbation series solution of the propagator in eq. (4.153) is represented as

$$\tilde{\mathcal{P}}(x,x_0) = \quad \underline{} \quad + \quad \underline{\bullet} \quad + \quad \underline{\bullet\bullet} \quad +\ldots \qquad (4.160)$$

The series of eq. (4.160) has a multiple scattering physical interpretation. The nth term corresponds to a nth order (n times) scattered wave which propagates freely from x_0 to ξ_1, is scattered at ξ_1 by roughness, propagates freely to ξ_2, is scattered at ξ_2, and so on. Here, *the free propagation* must be interpreted as propagation without scattering.

We now turn back to the calculation of the mean propagator $\langle\tilde{\mathcal{P}}\rangle_E$. The cluster expansions of the mean propagator can be represented by a *dressed diagram* with the following conventions (Frisch 1968):

1. Points belong to a given cluster are connected by dotted lines.

2. To every bare diagram involving l factors $\mathbf{S}$, are associated as many dressed diagrams as there are different partitions of the set $x_1, x_2, \ldots, x_l$ into clusters of at least two points.

3. To calculate a dressed diagram, the solid lines are replaced by deterministic propagators, the cluster of dotted line ending at $\xi_1, \ldots, \xi_l$ by factors

$\hat{S}(\xi_1)\cdots\hat{S}(\xi_l)\Gamma_l(\xi_1,\ldots,\xi_l)$, and integration is performed over all intermediate points.

The expansion of the mean propagator eq. (4.156) can now be written in terms of dressed diagrams:

$$\tag{4.161}$$

The following are the examples of some simple dressed diagram representations used in eq. (4.161):

$$= \int \tilde{\mathbf{P}}(x,\xi_2)\hat{\mathbf{S}}(\xi_2)\tilde{\mathbf{P}}(\xi_2,\xi_1)$$
$$\times \hat{\mathbf{S}}(\xi_1)\tilde{\mathbf{P}}(\xi_1,x_0)\,\Gamma_2(\xi_1,\xi_2)\,d\xi_1\,d\xi_2 \tag{4.162}$$

$$= \int \tilde{\mathbf{P}}(x,\xi_4)\hat{\mathbf{S}}(\xi_4)\tilde{\mathbf{P}}(\xi_4,\xi_3)$$
$$\times \hat{\mathbf{S}}(\xi_3)\tilde{\mathbf{P}}(\xi_3,\xi_2)\hat{\mathbf{S}}(\xi_2)$$
$$\times \tilde{\mathbf{P}}(\xi_2,\xi_1)\hat{\mathbf{S}}(\xi_1)\tilde{\mathbf{P}}(\xi_1,x_0)$$
$$\times \Gamma_2(\xi_3,\xi_4)\,\Gamma_2(\xi_1,\xi_2)$$
$$d\xi_1\,d\xi_2\,d\xi_3\,d\xi_4 \tag{4.163}$$

For a centered Gaussian roughness $\gamma(x)$, there are no clusters of more than two points, hence diagrams (3) and (7) in eq. (4.161) disappear. Note that the number of terms of nth order series in eq. (4.161) increases very rapidly with n, at least as $\frac{(2n)!}{2^n n!}$. This is another reason for the divergence of the perturbation expansion of the mean propagator (Frisch 1968). A technique for making such expansions more uniformly valid will be briefly discussed at the end of this section.

For example, when considering the analytical expression in eq. (4.163) for a diagram such as ___⌒⌒___ , it can be written as the product of the following five diagrams:

$$ ----- \ , \ \overset{\frown}{\underset{\bullet ---- \bullet}{}} \ , \ ----- \ , \ \overset{\frown}{\underset{\bullet ---- \bullet}{}} \ , \ ----- \qquad (4.164) $$

It is obvious that this factorization property is related to the topological structure of the diagram. To obtain an integral equation for $\tilde{P}$ with a kernel consisting of an infinite series, we introduce the following definitions based on the topology of the diagrams:

1. A diagram without terminals is a diagram which has been stripped of its external solid lines, such as ⌒ of diagram 2 in eq. (4.161) or ⌒⌒ of diagram 5 in eq. (4.161).

2. A diagram without terminals is *connected* if it cannot be cut into two or more diagrams, without cutting any dashed lines, in other words if it is not factorizable. Diagrams 2, 3, 5, 6, 7, 12 and 13, after stripped of their external solid lines, are connected, while diagrams 4, 8, 9, 10 and 11 are not connected. Therefore, any unconnected diagram can be factored into some lower order connected diagrams.

3. The mass operator (the name was borrowed from the quantum field theory) is defined as the sum of all possible connected diagrams contributing to $\left\langle \tilde{P} \right\rangle_E$. It

is denoted by $\check{M}$ or the symbol $\check{\textbf{M}}$:

$$\check{\textbf{M}} = \text{⌢} + \text{⟋⫶⟍} + \text{⟋⌢⌢⟍} \quad \text{⟋⌢⌢⟍} + \cdots . \qquad (4.165)$$

4. The symbol for the mean propagator $\left\langle \tilde{P} \right\rangle_E$ is introduces as

$$\left\langle \tilde{P}(x, x_0) \right\rangle_E = \qquad x \underline{\hspace{3cm}} x_0 \qquad (4.166)$$

By those definitions, all unconnected diagrams are factored into connected diagrams and the diagramatic expansion of $\left\langle \tilde{P} \right\rangle_E$ in eq.(4.161) is represented by the sum of all possible connected diagram, the mass operator:

$$\underline{\hspace{3cm}} = \underline{\hspace{2cm}} + \underline{\hspace{1cm}}\check{\textbf{M}}\underline{\hspace{1cm}} \qquad (4.167)$$

Eq. (4.167) is an integral equation for $\left\langle \tilde{P} \right\rangle_E$ with the kernel of mass operator, which is called the *Dyson equation*. Note that the Dyson equation (4.167) is for the modal amplitude propagator *not* for the Green's function as in other areas, like quantum electrodynamics, many-body problems, statistical mechanics, etc. The analytical form of the Dyson equation is

$$\left| \left\langle \tilde{P}(x, x_0) \right\rangle_E = \check{P}(x, x_0) + \int_{x_0}^x \check{P}(x, \xi_1) \check{M}(\xi_1, \xi_2) \left\langle \tilde{P}(\xi_2, x_0) \right\rangle_E d\xi_1 d\xi_2. \right| \qquad (4.168)$$

4.8.4 The Bethe-Salpeter equation for the covariance of the propagator

We investigate the second statistical moment of the propagator $\left\langle \tilde{P}^\dagger \tilde{P} \right\rangle_E$, i.e., the covariance of two propagators (fields). The importance of the propagator covariance is that it enables us to synthesize the envelope of the mean squared signals (e.g., envelopes of bottom interacting seismo-acoustic signals, seismic coda envelope, etc.),

and analyze the effect of the multiple rough surface scattering on the envelope decay. First, the product of the propagator $\tilde{\mathcal{P}}$ and its Hermitian conjugate is written in terms of the bare double-diagrams (Frisch 1968):

$$\tilde{\mathcal{P}}^\dagger(x,x_0)\tilde{\mathcal{P}}(x',x_0') = \quad + \quad + \quad + \quad +$$

$$+ \quad + \quad + \quad + \cdots, \quad (4.169)$$

where we make the convention that each double-diagram is the product of the propagator corresponding to the lower line and of the Hermitian conjugate of the propagator corresponding to the upper line. For the propagator covariance, which is the mean double propagator, a similar expansion holds in terms of dressed double-diagram:

$$\left\langle \tilde{\mathcal{P}}^\dagger(x,x_0)\tilde{\mathcal{P}}(x',x_0') \right\rangle_E = \quad + \quad + \quad$$

$$+ \quad + \quad + \cdots, \quad (4.170)$$

We also give the examples of the analytical representation for some simple dressed double-diagram used in eq. (4.170):

$$= \int \tilde{\mathbf{P}}^\dagger(x,\xi_1)\hat{\mathbf{S}}^\dagger(\xi_1)\tilde{\mathbf{P}}^\dagger(\xi_1,x_0)$$
$$\times \tilde{\mathbf{P}}(x',\xi_2)\hat{\mathbf{S}}(\xi_2)\tilde{\mathbf{P}}(\xi_2,x_0')$$
$$\times \Gamma_2(\xi_1,\xi_2)\,d\xi_1\,d\xi_2 \quad (4.171)$$

$$= \int \tilde{\mathbf{P}}^\dagger(x,\xi_1)\hat{\mathbf{S}}^\dagger(\xi_1)\tilde{\mathbf{P}}^\dagger(\xi_1,\xi_2)$$
$$\times \hat{\mathbf{S}}^\dagger(\xi_2)\tilde{\mathbf{P}}^\dagger(\xi_2,x_0)$$
$$\times \tilde{\mathbf{P}}(x',\xi_3)\hat{\mathbf{S}}(\xi_3)\tilde{\mathbf{P}}(\xi_3,x_0')$$
$$\times \Gamma_2(\xi_1,\xi_3)\Gamma_2(\xi_2,\xi_3)\,d\xi_1\,d\xi_2\,d\xi_3. \quad (4.172)$$

Similarly, all unconnected double-diagrams are represented by the connected double-diagram by the factorization property, and all double-diagram which are not connected between the upper line and the lower line can be represented by the product $\left\langle \tilde{P}^\dagger \right\rangle_E \left\langle \tilde{P} \right\rangle_E$. By introducing the symbol for the propagator covariance,

$$\left\langle \tilde{P}^\dagger(x, x_0)\tilde{P}(x', x_0') \right\rangle_E = \quad \text{(4.173)}$$

the diagramatic expansion of the propagator covariance is written as the integral equation with a kernel which is the sum of all possible connected double-diagrams contributing to $\left\langle \tilde{P}^\dagger \tilde{P} \right\rangle_E$:

$$\text{(4.174)}$$

Eq. (4.174) is called *the Bethe-Salpeter equation* and its kernel is *the intensity operator* (Frisch 1968; Rytov et al. 1989) denoted by $\check{K}$ or the symbol $\boxed{\check{K}}$. The infinite series of $\check{K}$ represents the sum of all possible connected double diagrams. Its diagram representation is

$$\text{(4.175)}$$

The Dyson equation and the Bethe-Salpeter equation are a major result of this paper which enable us to analyze the phenomenon of elastic wave multiple scattering. However, the expansions obtained in this section were shown to be divergent by Frisch (1968). Moreover, he also showed that these expansions contain secular terms

$$= \frac{\Delta y I_\alpha^S}{\Delta S_z E^0}$$

$$= \frac{I_\alpha^S}{\Delta x E^0}, \tag{4.176}$$

where $\Delta S_z = \Delta x \Delta y$, and E^0 is the incident energy flux density. The relation between the energy flux across the unit strip I^0 and the energy flux density E^0 are:

$$E^0 = \frac{I^0}{D_z}, \tag{4.177}$$

where D_z is defined as the reference depth chosen such that all the energy crossing a vertically oriented rectangle of area $\Delta y\, D_z$. For the reference depth, a reasonable choice is to use the turning depth of the deepest turning mode. Note that eq. (4.176) is dimensionless unlike the scattering cross section for volume scattering. I_α^S is the energy flux density of scattered field of the αth mode across the plane $x = constant$ with unit width in y-direction, i.e., $\Delta y I_\alpha^S$ is the energy flux across the plane S_x. With the assumption that each mode is normalized to carry unit energy flux, I_α^S becomes

$$I_\alpha^S(x,\omega) = \left| \hat{d}_\alpha(x,\omega) \right|^2. \tag{4.178}$$

Applying the Born approximation to the evolution equation for the $\mathcal{O}(\varepsilon)$ system eq. (4.134) and the initial condition $\hat{d}_\alpha(x_s) = 0$ to the evolution equation eq. (4.134) yields

$$\hat{d}_\alpha(x,\omega) = \sum_\beta \tilde{P}_{\alpha\beta}(x, x_s)\hat{d}_\beta(x_s) + \sum_\beta \int_{x_s}^x \tilde{P}_{\alpha\beta}(x,\xi) g_\beta(\xi) d\xi$$

$$= \sum_n \sum_\beta \gamma_n \int_{x_s}^x \tilde{P}_{\alpha\beta}(x,\xi) g_\beta^n(\xi) d\xi, \tag{4.179}$$

where the stochastic effective source is rewritten as

$$\mathbf{g} = (\hat{\mathbf{D}} + i\hat{\mathbf{E}}\hat{\mathbf{B}})\hat{\mathbf{c}}$$

$$\approx (\hat{\mathbf{D}} + i\hat{\mathbf{E}}\hat{\mathbf{B}})\hat{\mathbf{c}}^{(0)}$$

$$= \sum_n \gamma_n(\hat{\mathbf{D}}^n + i\hat{\mathbf{E}}^n\hat{\mathbf{B}})\hat{\mathbf{c}}^{(0)}$$

$$\equiv \sum_n \gamma_n \mathbf{g}^n. \tag{4.180}$$

Figure 4.6: Model geometry for defining the scattering cross section per unit area of rough surface.
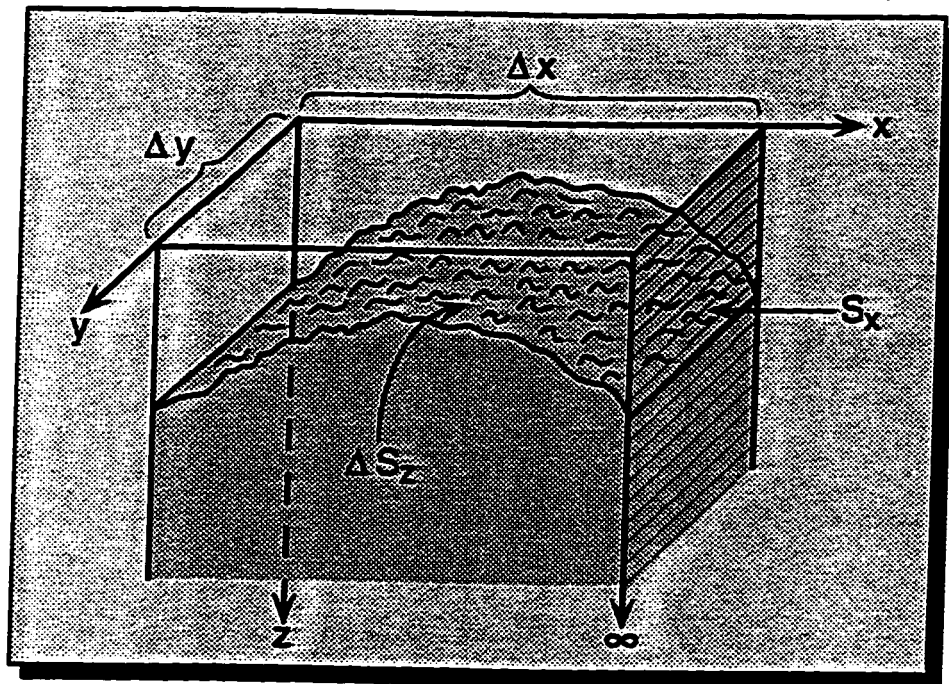
The summation is done over all rough surfaces. The modal amplitude of the coherent field for the stochastic medium $\hat{c}$ is approximated by the primary field $\hat{c}^{(0)}$ for the deterministic medium, i.e., the Born approximation. The matrices $\hat{D}^n$ and $\hat{E}^n$ in eq. (4.180) are the purely deterministic parts of $\hat{D}$ and $\hat{E}$, and γ_n is the stochastic roughness of the nth interface. Substituting eq. (4.179) into eq. (4.178), and taking the ensemble average yields the energy flux of the scattered field of the αth mode I_α^S:

$$
\begin{aligned}
I_\alpha^S(x,\omega) &= \sum_n \int_x^{x+\Delta x} \int_x^{x+\Delta x} \left\langle \gamma_n^2 \right\rangle_E \sum_{\beta,\nu} N_n(\xi_1,\xi_2) \\
&\quad \times g_\beta^{n\dagger}(\xi_2) \tilde{P}_{\beta\alpha}^\dagger(x+\Delta x,\xi_2)\tilde{P}_{\alpha\nu}(x+\Delta x,\xi_1)g_\nu^n(\xi_1)\,d\xi_1 d\xi_2 \\
&= \sum_n \int_x^{x+\Delta x} dx \left\langle \gamma_n^2 \right\rangle_E \int_0^\infty dr \\
&\quad \left\{ \sum_{\beta,\nu} N_n(r)g_\beta^{n\dagger}(x+r) \right. \\
&\quad \left. \times \tilde{P}_{\beta\alpha}(x+r,x+\Delta x)\tilde{P}_{\alpha\nu}(x+\Delta x,x)g_\nu^n(x) \right\},
\end{aligned}
\tag{4.181}
$$

where $N_n(r)$ is the normalized autocorrelation function of $\gamma_n(x)$ and $r \equiv |\xi_2 - \xi_1|$. Exponential or Gaussian autocorrelation functions are often chosen to model stochastic processes of physical interest (Chernov 1960). If we assume that the scale length of the heterogeneity is much smaller than the propagation distance, i.e., $a \ll R$, then the autocorrelation $N_n(r)$ will have small side lobes and the scattered energy flux can be written in a simpler form (Wang & Herrmann, 1988):

$$
\begin{aligned}
I_\alpha^S(x,\omega) &\approx \sum_n \int_x^{x+\Delta x} \left\langle \gamma_n^2 \right\rangle_E \sum_{\beta,\nu} g_\beta^{n\dagger}(x)g_\nu^n(x)\tilde{P}_{\alpha\nu}(x+\Delta x,x) \\
&\quad \left\{ \int_0^\infty N_n(r)\tilde{P}_{\beta\alpha}(x+r,x+\Delta x)dr \right\} dx
\end{aligned}
\tag{4.182}
$$

For a small segment Δx ($\ll 1$), I_α^S becomes

$$
\begin{aligned}
I_\alpha^S &\approx \Delta x \sum_n \sum_{\beta\nu} \left\langle \gamma_n^2 \right\rangle_E g_\beta^{n\dagger}(x)g_\nu^n(x)\tilde{P}_{\alpha\nu}(x,x) \int_0^\infty N_n(r)\tilde{P}_{\beta\alpha}(x+r,x)dr \\
&= \Delta x \sum_n \sum_\beta \left\langle \gamma_n^2 \right\rangle_E g_\beta^{n\dagger}(x)g_\alpha^n(x) \int_0^\infty N_n(r)\tilde{P}_{\beta\alpha}(x+r,x)dr,
\end{aligned}
\tag{4.183}
$$

where the relation $\tilde{P}_{\alpha\nu}(x,x) = \delta_{\alpha\nu}$ is used. Finally, the modal scattering cross section can be written as

$$\sigma_\alpha = \frac{1}{E^0}\sum_n\sum_\beta \left\langle\gamma_n^2\right\rangle_E g_\beta^{n\dagger}(x)g_\alpha^n(x)\int_0^\infty N_n(r)\tilde{P}_{\beta\alpha}(x+r,x)dr. \tag{4.184}$$

Using the modal scattering cross section, the *total scattering cross section* per unit area of the rough interfaces can be written as:

$$\sigma = \sum_\alpha \sigma_\alpha, \tag{4.185}$$

where the sum is over all modes. For the short distance Δx, the relation between the modal scattering cross section σ_α and the total energy flux I^S is

$$\begin{aligned} I^S &= \sum_\alpha I_\alpha^S \\ &= \Delta x E^0 \sum_\alpha \sigma_\alpha. \end{aligned} \tag{4.186}$$

The generation of the scattered field is interpreted as the energy loss of the coherent field. We assume here that the direction of maximum attenuation of amplitude is along the x-axis, which is also the direction of propagation. Then the spatial decay of power during the propagation through a wavelength-distance becomes (Aki & Richards 1980; Sato 1984)

$$\begin{aligned} \Delta I &= \frac{\lambda}{\Delta x}I^S, \\ &= E^0\sum_\alpha \lambda_\alpha\sigma_\alpha \end{aligned} \tag{4.187}$$

where λ is the wavelength given in terms of ω and phase velocity c by $\lambda = \frac{2\pi c}{\omega} = \frac{2\pi}{k}$, and $R = x_r - x_s$. Scattering Q_S can be derived from the definition of *spatial Q*: (Aki & Richards 1980):

$$\begin{aligned} spatial\ \ Q_S^{-1} &= \frac{\Delta I}{2\pi I^0} \\ &= \sum_\alpha \frac{\sigma_\alpha}{D_z k_\alpha}, \end{aligned} \tag{4.188}$$

From equation (7.92) of Aki & Richards (1980), the relation between the spatial and the temporal Q for surface waves is

$$\text{temporal} \quad Q^{-1} = \frac{U}{c} \times \quad \text{spatial} \quad Q^{-1}, \tag{4.189}$$

where c is the phase velocity and U is the group velocity. The $\text{temporal} \, Q_S^{-1}$ can also be written as

$$Q_S^{-1} = \sum_{\alpha} \frac{U_{\alpha}\sigma_{\alpha}}{\omega D_z}, \tag{4.190}$$

or

$$Q_S^{-1} = \sum_{\alpha,\beta}\sum_{n} \left\langle \gamma_n^2 \right\rangle_E \frac{U_{\alpha}}{\omega I^0} g_{\beta}^{n\dagger}(x) g_{\alpha}^{n}(x) \int_0^{\infty} N_n(r)\tilde{P}_{\beta\alpha}(x+r,x)\,dr, \tag{4.191}$$

where U_{α} is a group velocity of the αth mode. Hereafter, we employ the temporal Q_S^{-1} only and the word temporal is dropped for convenience. Hoshiba (1991) has summarized the functional form of Q_S^{-1} derived by previous workers. The results he summarized employed ray theory with a single or multiple scattering model, or radiative transfer theory, and were restricted to volume scattering. Note that eq. (4.190) for the modal Q_S^{-1} is functionally equivalent to the result obtained from the single scattering model, but it requires a summation over mode number to obtain the total contribution to Q_S^{-1} for scattering from rough interfaces.

Next, we derive the final forms of the scattering cross section and the scattering Q_S^{-1} analytically for a range-dependent medium with weakly varying reference structure. First, the integration in eq. (4.191) for a plane scalar wave becomes

$$\mathcal{I}(x) = \int_{-\infty}^{\infty} N_n(r)\,e^{ikr}\,dr. \tag{4.192}$$

For the exponential autocorrelation function, $\mathcal{I}(x)$ is

$$
\begin{aligned}
\mathcal{I}(x) &= \int_{-\infty}^{\infty} e^{-\frac{|r|}{a}}\,e^{ikr}\,dr \\
&= \frac{2a}{1+a^2k^2},
\end{aligned} \tag{4.193}
$$

and for the Gaussian autocorrelation function, $\mathcal{I}(x)$ is

$$
\begin{aligned}
\mathcal{I}(x) &= \int_{-\infty}^{\infty} e^{-\frac{r^2}{a^2}} e^{ikr} \, dr \\
&= \sqrt{\pi} \, a \, e^{-(\frac{ka}{2})^2},
\end{aligned}
\tag{4.194}
$$

where a is the roughness correlation length.

For the weakly varying reference structure, the off-diagonal terms of the transformed coupling matrix $\hat{\mathbf{B}}$ can be ignored (WKBJ approximation):

$$
H_{\alpha\beta} \approx K_{\alpha\beta} = k_\alpha \delta_{\alpha\beta}.
\tag{4.195}
$$

If the scale length of the boundary roughness is assumed much smaller than the propagation distance, the autocorrelation $N_n(r)$ will have small side lobes, and then the integration over a few correlation lengths can be approximated as

$$
\int N_n(r) \tilde{P}_{\beta\alpha}(x + r, x) \, dr \approx \int N_n(r) \exp\{iK_{\beta\alpha} r\} \, dr.
\tag{4.196}
$$

There is a direct mapping between the diagonal matrix and its function:

$$
\{f(\mathbf{K})\}_{\alpha\beta} = f(K_{\alpha\beta}),
\tag{4.197}
$$

i.e.,

$$
\tilde{P}_{\alpha\beta}(x + r, x) = \exp\{iK_{\alpha\beta} r\}
\tag{4.198}
$$

For the weakly varying reference structure, the modal scattering cross section is

$$
\sigma_\alpha = \frac{2}{E^0} \sum_n \left\langle \gamma_n^2 \right\rangle_E |g_\alpha^n(x)|^2 \frac{a}{1 + a^2 k_\alpha^2} \quad \text{for} \quad N_n(r) = \exp\left(-\frac{|r|}{a}\right),
\tag{4.199}
$$

$$
\sigma_\alpha = \frac{\sqrt{\pi} \, a}{E^0} \sum_n \left\langle \gamma_n^2 \right\rangle_E |g_\alpha^n(x)|^2 \exp\left\{-\left(\frac{k_\alpha a}{2}\right)^2\right\}
$$

$$
\text{for} \quad N_n(r) = \exp\left(-\frac{r^2}{a^2}\right),
\tag{4.200}
$$

and the scattering Q_S^{-1} is

$$
Q_S^{-1} = \frac{2}{\omega I^0} \sum_\alpha \sum_n \left\langle \gamma_n^2 \right\rangle_E U_\alpha |g_\alpha^n(x)|^2 \frac{a}{1 + k_\alpha^2 a^2}
$$

$$\text{for} \quad N_n(r) = \exp\left(-\frac{|r|}{a}\right), \tag{4.201}$$

$$Q_S^{-1} = \frac{\sqrt{\pi}a}{\omega I^0} \sum_\alpha \sum_n \langle\gamma_n^2\rangle_E U_\alpha |g_\alpha^n(x)|^2 \exp\left[-\left(\frac{k_\alpha a}{2}\right)^2\right]$$

$$\text{for} \quad N_n(r) = \exp\left(-\frac{r^2}{a^2}\right). \tag{4.202}$$

From eqs. (4.201) & (4.202), we can numerically synthesize scattering Q_S^{-1} for the range dependent medium with given statistical properties and at a given frequency, and generate a Q_S^{-1} curve in the frequency domain. The temporal decay of the signal envelope can be predicted from the synthesized Q_S^{-1}. On the other hand, we can retrieve the statistical properties of the boundary roughness from the fact that Q_S^{-1} is an explicit function of the roughness variance $\langle\gamma_n^2\rangle_E$ and the correlation length a. If we assume that the stochastic roughness $\gamma_n(x)$ is a stationary process, i.e., the statistical properties of $\gamma_n(x)$ do not depend on their absolute position, we can design an inverse problem for the variance and the correlation by fitting the spectral Q_S^{-1} curve, predicted by the model vector of ($\langle\gamma_n^2\rangle_E$, a), to the observed data in a least squares sense (Scherbaum & Sato 1991). The temporal decay of the envelope can be measured by means of an analysis of peak and half-maximum amplitude arrivals of the envelopes of signals filtered by a narrow band pass filter.

For numerical computation, first we choose a simple depth dependent model which consists of a fluid layer over solid half space. The sound speed in water is 1500 m/s and the compressional and the shear wave speeds of the half space are 3270 m/s and 1620 m/s, respectively. The water depth is 200 m. In Fig. 4.7, the first 5 modes computed at f = 50 Hz are shown. Their phase velocities are 1310.7 m/s, 1504.3 m/s, 1517.1 m/s, 1538.8 m/s and 1569.5 m/s, respectively. Their horizontal modal wavelengths range between 26.2 m and 31.4 m. The fundamental mode is a Stoneley wave and the next four higher overtones are confined mostly to the water layer. There exists only one rough boundary between the fluid layer and the solid half space. Note that the choice of 1m for the roughness variance is only a convenience for the computations.

Figure 4.7: Simple computational model. The vertical displacement eigenfunctions of first 5 normal modes are computed for a depth-dependent model at f = 50 Hz. The model consists of a water layer over solid half space. The dotted line indicates the water depth (200 m).
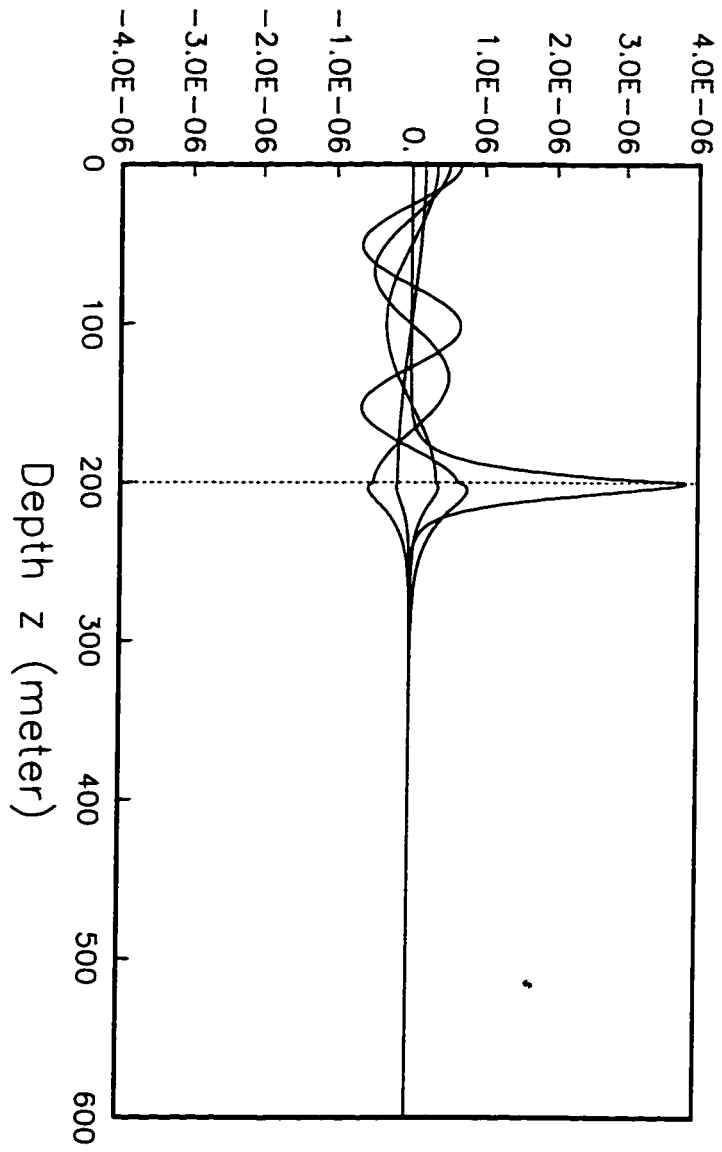
Figure 4.8: Semi-log plots of the modal scattering cross sections computed with the Gaussian autocorrelation function for the correlation length $a = 1\,m$ and the variance $\langle \gamma_n^2 \rangle_E = 1\,m$.
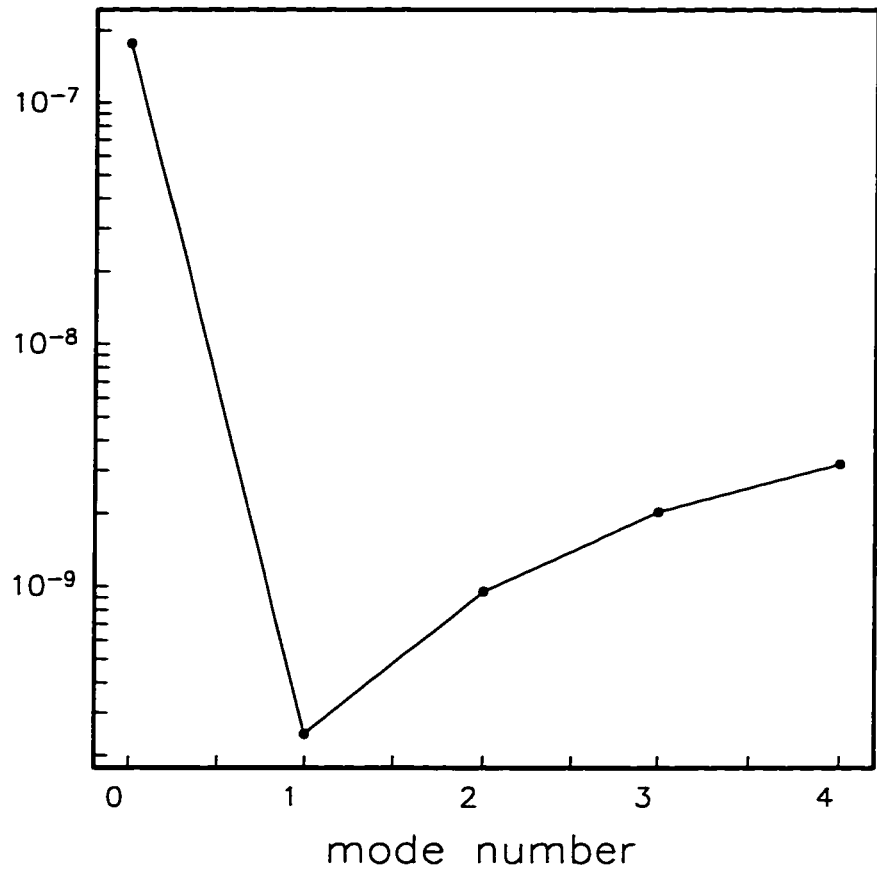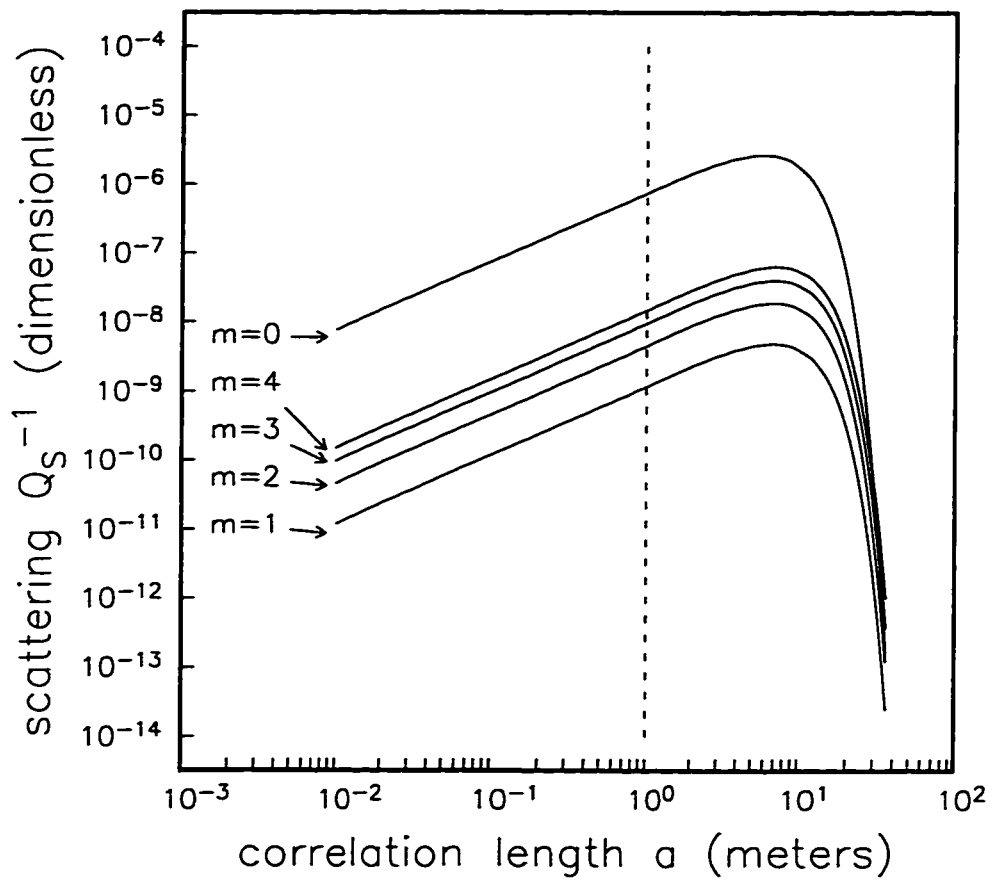
Figure 4.9: Log plots of the scattering Q_S^{-1} computed with the Gaussian autocorrelation function for the variance $\langle \gamma_n^2 \rangle_E = 1\,m$.

The curves for Q_S^{-1} are computed from the Born approximation and the roughness variance enters only as a scale factor. The shape of the curves do not depend on the roughness variance.

The modal scattering cross section is computed with a roughness variance of 1 m and a correlation length 1 m using the Gaussian autocorrelation function (Fig. 4.8). The modal scattering cross section of the Stoneley wave (m=0) is larger than those of other higher modes. That means that the interface wave is more strongly affected by the interface roughness than the water waves. Also the scattering Q_S^{-1} is computed for the same model with a variance of 1 m and employing the Gaussian autocorrelation function (Fig 4.9). The peaks of the scattering Q_S^{-1} curves are correlated with their modal wavelengths. In fact the maxima occur at the values $a_{max} = \frac{\lambda}{\sqrt{2}\pi}$ for the Gaussian autocorrelation function.

As a second example, we have computed the modal scattering cross section and scattering Q_S^{-1} for a realistic shallow water environment. In Fig. 4.10, the model structure, the velocity and the density profiles, and the mode functions are illustrated for a frequency of 10 Hz. The model can be characterized by an upper water layer, low-velocity sediment layers, and a high-velocity hard bottom with two-dimensional range dependence. The range dependence is assumed to be confined between $x = 0$ m and $x = 76$ m, and the slope of the interfaces varies up to 45°. The first 9 modes are used for computation. The energy of the first four modes, whose phase velocities range between 145.6 m/s and 815.3 m/s at 10 Hz, is mainly confined in the low-velocity sediment layers (depth 40 - 80 m at $x = 0$). The next five modes, whose phase velocities range between 1015.6 m/s and 1162.2 m/s at the same frequency, propagate in the hard bottom (depth 200 - 600 m at $x = 0$).

The modal scattering cross section, normalized by the variance, is computed with unit incident energy flux density. Each mode is assumed to have equal amplitude c_α^0 upon incidence. In Fig. 4.11 and Fig. 4.12, the modal scattering cross sections are computed at two different point in the medium, point A (5.7° slope) and point B

141

Figure 4.10: Computational model. (a) First 9 normal modes at $x = 0$. (b) Density (solid line), compressional velocity (dashed line), and shear velocity (dotted line) at $x = 0$. (c) 2-dimensional shallow water structure. Diamond symbols indicate the point where local normal modes are computed and point A and B represent the location where the modal scattering cross sections are computed.
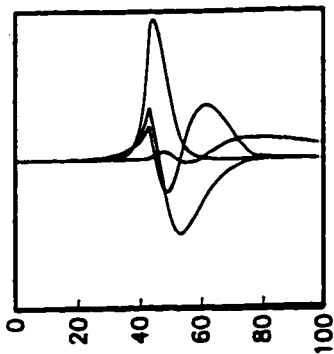
(a) Normal Modes (u_z) (b) Velocity Profile (c) Shallow-Water Structure
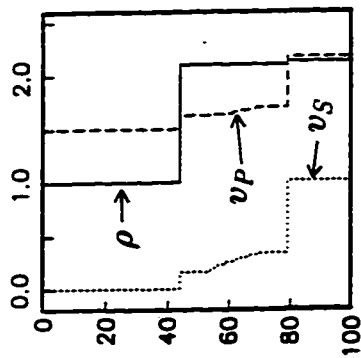
x (meter)

z (meter)

(45° slope) (see Fig. 4.10) using the exponential autocorrelation function with two different correlation lengths $a = 1$ m and $a = 10$ m. In Fig. 4.13 and Fig. 4.14, the Gaussian correlation function is used.
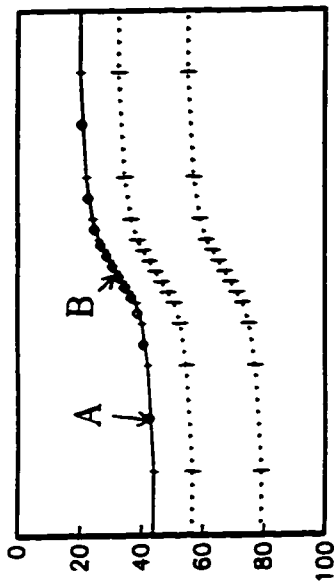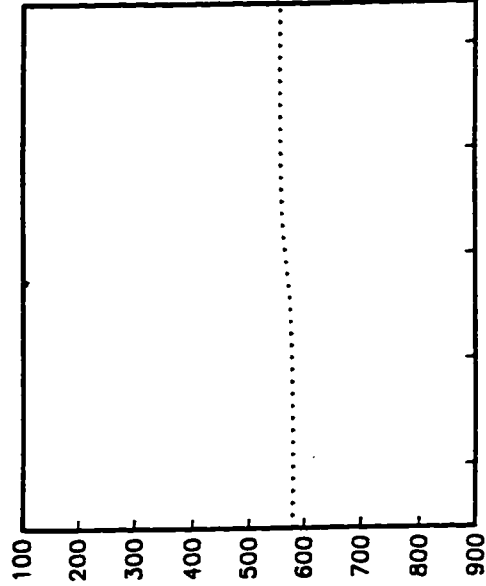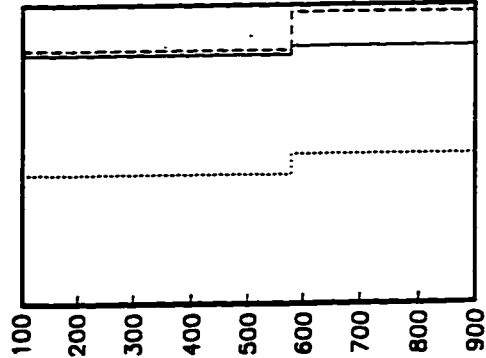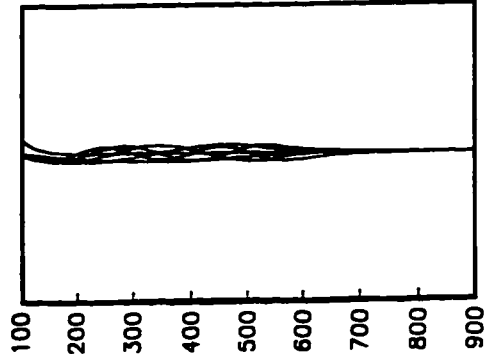
The somewhat complicated dependence of the cross section on mode number becomes clear on examination of Figure 4.15 and 4.16, which show the scattering Q_S^{-1} for the exponential and Gaussian autocorrelation functions, respectively. The two vertical lines indicate the correlation length values for which the cross section are shown in Figures 4.11- 4.14.

There are two groups of curves in Figures 4.15 and 4.16. The solid curves are for the first four modes and the dashed curves are for the next five modes. Generally, the first four modes, which are mostly confined to the layers between the water and the hard bottom, scattered more strongly than the higher modes, while higher modes, propagating deeper in the hard bottom, scattered less. The fourth mode scattered the least and the modal scattering cross sections of the higher modes gradually increase because the energy, propagating along the deep interface ($z \approx 600$ m), increases as the mode number increases. The relatively smaller scattering of the fourth mode is the reason for the pronounced minimum in the cross section, Figures 4.11- 4.14. Especially affected by boundary roughness are the first, the fifth and sixth modes. The first mode is the Stoneley (Scholte) wave at the water-sediment boundary. The third and the fourth modes propagate just above and along the boundary between the softer sediment and hard bottom. Therefore, scattered intensity is sensitive to the magnitude of the impedance contrast across a boundary. However, the slope of the reference boundary does not have a large effect on the scattered intensity. This is likely due to the very long correlation length of the mean structure compared to what was chosen for the boundary roughness. The weak dependence of the scattering cross section on the reference structure can be readily seen by comparing Figures 4.11 and 4.12, which are computed at two different point A and B in the reference structure (Fig. 4.10). This is also apparent upon comparison of Figures 4.13 and 4.14.

Figure 4.11: Semi-log plots of the normalized modal scattering cross sections computed with the exponential autocorrelation function for the correlation length $a = 1\,m$ (dots), and for $a = 10\,m$ (circles) at point A on Fig. 4.6, where the slope is $5.7°$.
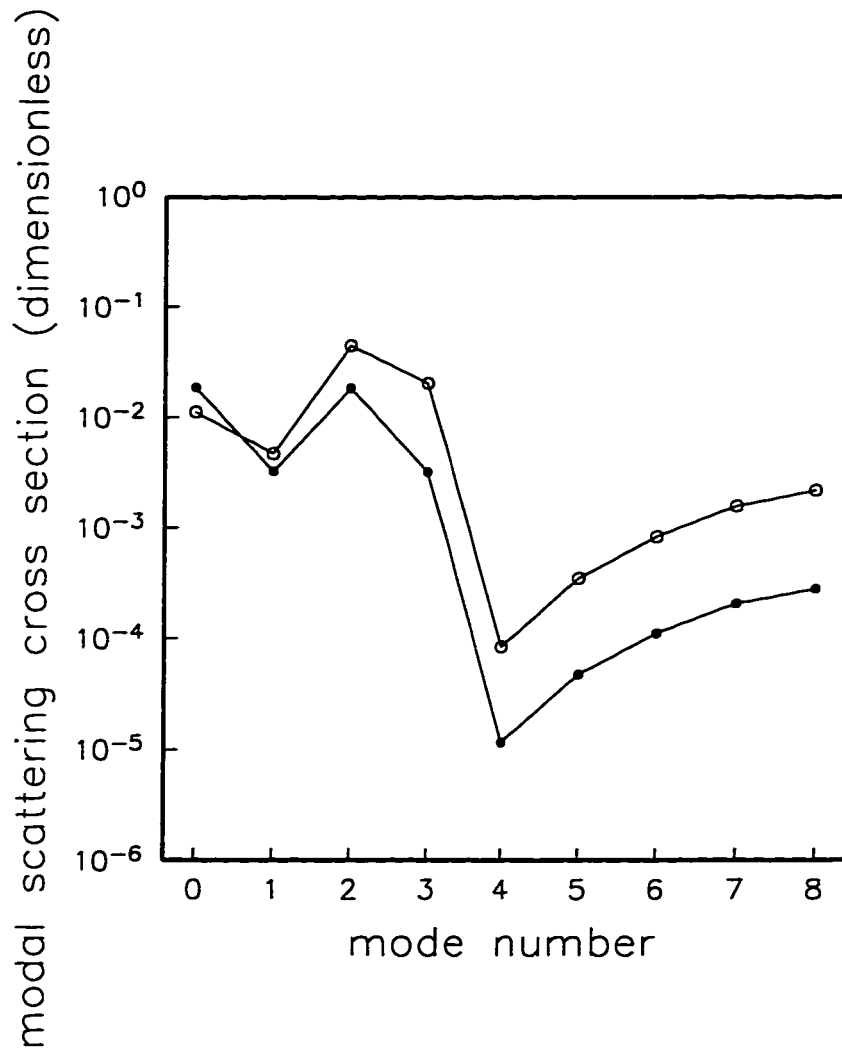
Figure 4.12: Same as Fig. 4.11 at point B on Fig. 4.6, where the slope is 45°, with the exponential function.
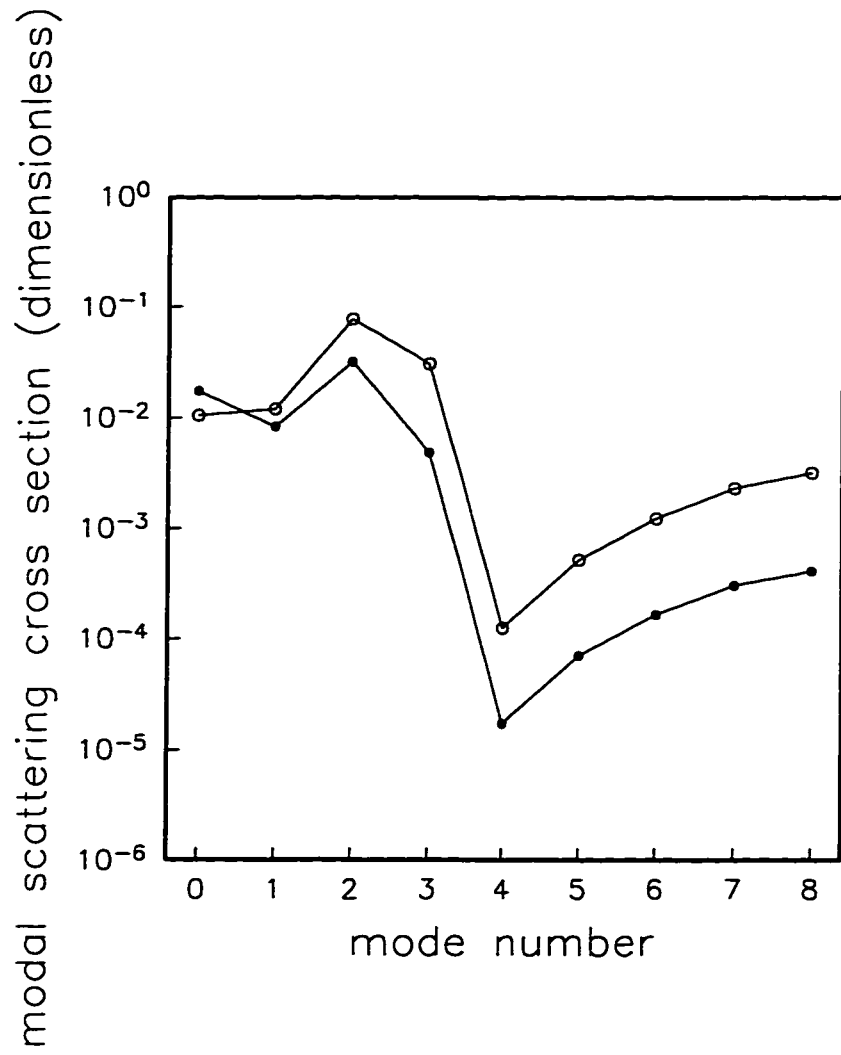
145

Figure 4.13: Same as Fig. 4.11 at point A on Fig. 4.6, where the slope is 5.7° with the Gaussian autocorrelation function.
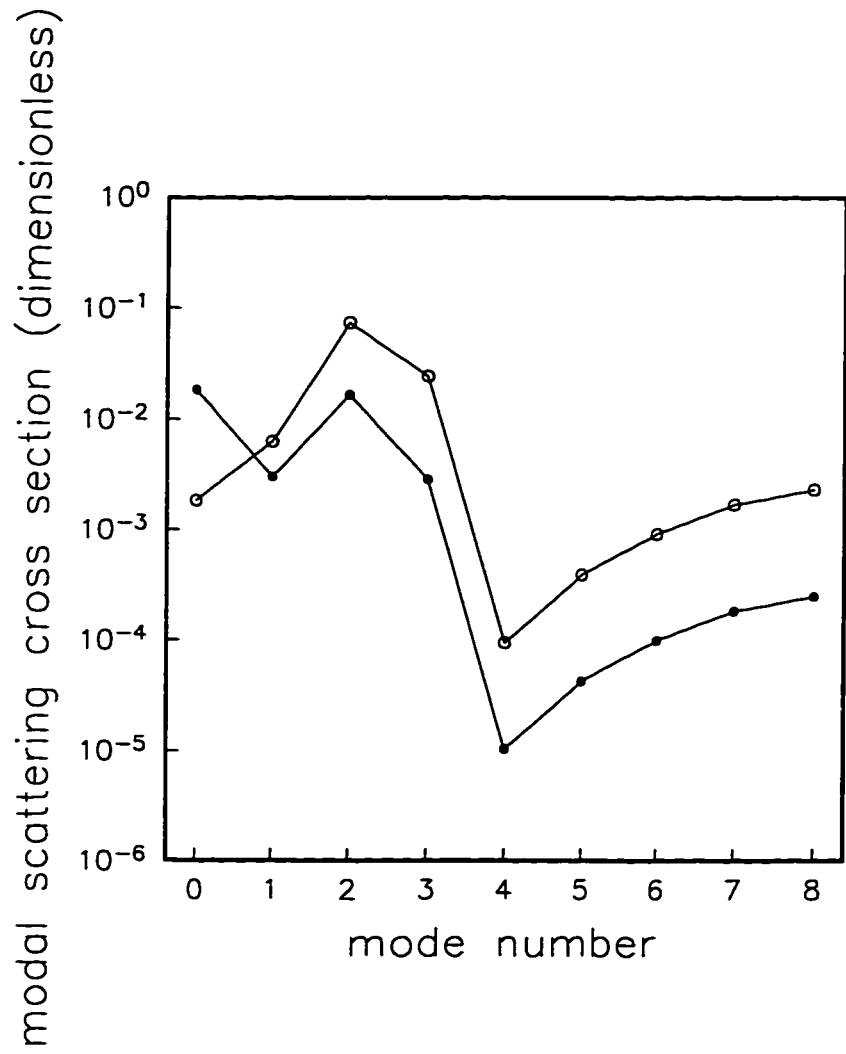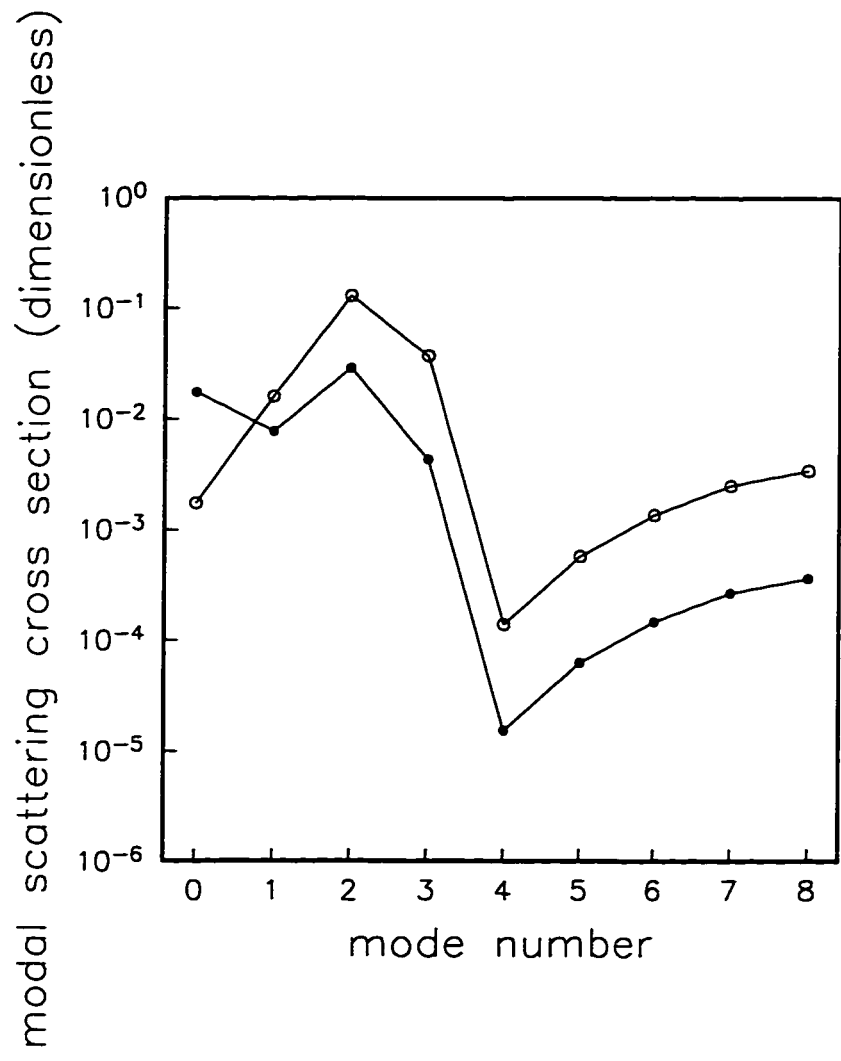
Figure 4.14: Same as Fig. 4.11 at point B on Fig. 4.6, where the slope is 45°, with the Gaussian autocorrelation function.

Now concentrating on Figures 4.15 and 4.16, it can be seen that the correlation length for which Q_S^{-1} reaches a maximum increases with mode number. The maximum correlation length a_{max} for a particular mode linearly depends on the horizontal modal wavelenth λ. The analytically derived relation is $a_{max} = \frac{\lambda}{\sqrt{2}\pi}$ for the Gaussian autocorrelation function, and $a_{max} = \frac{\lambda}{2\pi}$ for the exponential autocorrelation function. The horizontal modal wavelengths of the first four modes at 10 Hz are $\lambda_0 = 14.6$ m, $\lambda_1 = 25.0$ m, $\lambda_2 = 34.9$ m & $\lambda_3 = 81.5$ m. The horizontal modal wavelengths of the higher modes have a rather narrow range (101.6 m $\leq \lambda \leq 116.2$), which makes the locations of the maximum for the higher modes appear nearly the same.

The scattering Q_S^{-1} must be computed assuming a Gaussian correlation function (Fig. 4.16) falls off much more rapidly after reaching a maximum than does Q_S^{-1} for the exponential correlation function. However, the slopes of the Q_S^{-1} curves prior to their maxima are independent of the form of the correlation function for our two choices. Also the Q_S^{-1} curves are more sharply peaked for Gaussian correlations than for exponential correlations. This is an indication that boundary roughness with exponential correlations is a more efficient scatterer than boundary roughness with Gaussian correlations. The final thing to notice is that the first four modes, confined mostly to the sediment, are scattered more strongly than the last five basement modes. The maximum of the Q_S^{-1} curves for the first four modes occur at shorter correlation lengths because the horizontal modal wavelengths are shorter as mentioned.

For a strongly varying reference structure, we cannot disregard the off-diagonal terms of the transformed coupling matrix $\mathbf{H}$, i.e., we cannot ignore the deterministic mode coupling. The relation eq. (4.198) is no longer valid for the general coupling matrix. Therefore, the scattering cross section and the Q_S^{-1} curve must be computed by numerical integration of eqs. (4.184) & (4.191) instead of by analytical integration.

148

Figure 4.15: Log plots of the normalized scattering Q_S^{-1} of the first nine modes computed with the exponential autocorelation function at a frequency of 10 Hz . Solid lines are for the first four modes, and broken lines are for the next five modes. The unit of the correlation length a is meter and scattering Q_S^{-1} is dimensionless. The vertical dashed lines mark the two values of the correlation length a for which the cross section are shown in Figures 4.11 - 4.14.
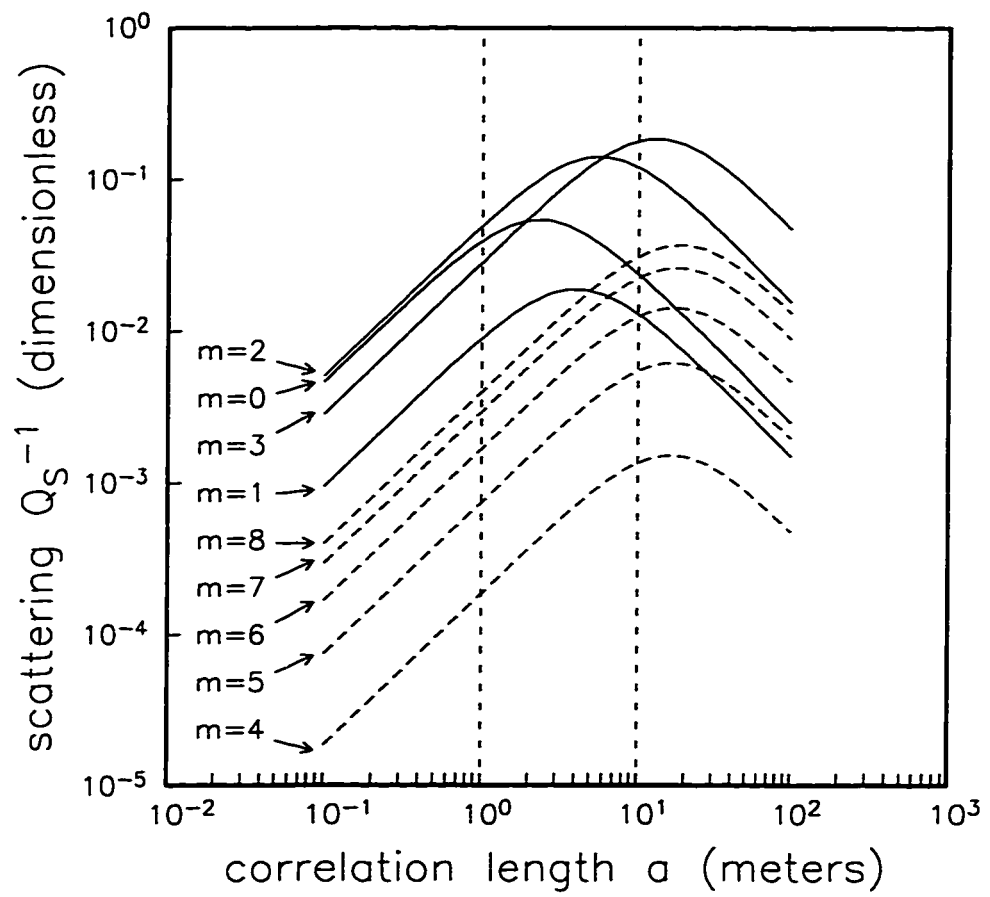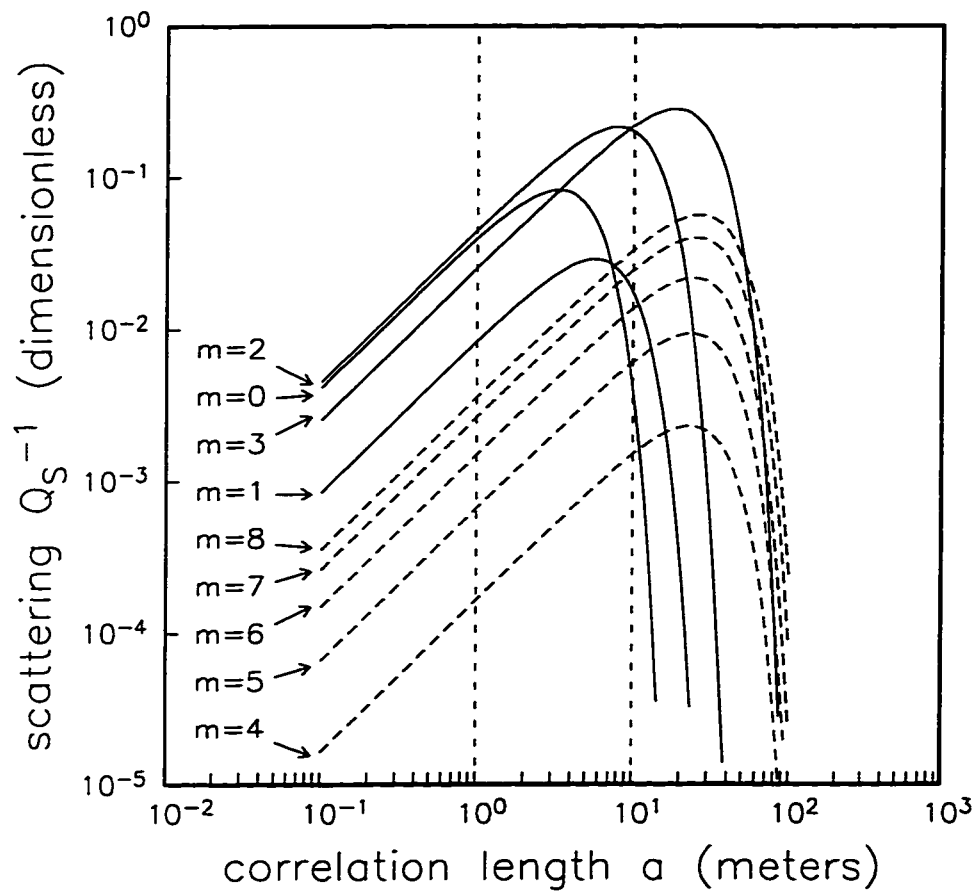
Figure 4.16: Same as Fig. 4.15 with the Gaussian autocorrelation function.

4.10 An Inverse Problem for the Roughness Variance and Correlation Length

In the preceding section, we proposed that the inverse problem can be solved by a least-squares fit of the predicted Q_S^{-1} curve to the observed data in the frequency domain. However, for the case when we cannot assume that the stochastic roughness is a locally stationary process, we cannot retrieve the laterally varying statistical properties from only the measurement of Q_S^{-1}. For the case of a locally stationary roughness, we have derived an expression for the power spectrum from the Born approximation of the coherent field, and designed a power spectrum inversion by iterative fitting of the synthetic power spectrum to the observed signal's tail (e.g., seismic coda waves). The purpose of this section is to describe how to retrieve the local variance and the correlation length of roughness by spectrum fitting, with the assumption that the material properties of the reference structure are known. Using the orthogonality of the local modes, the total power carried by the coherent field across planes $x = x_r$, can be written as (Aki & Richards 1980, ch. 13)

$$
\begin{aligned}
\|v_0^{(1)}(x_r,\omega)\|^2 &= \ <v_0^{(1)}(x_r,\omega), v_0^{(1)}(x_r,\omega)> \\
&= \ <v_0^{(0)}(x_r,\omega), v_0^{(0)}(x_r,\omega)> - <v_1^{(1)}(x_r,\omega), v_1^{(1)}(x_r,\omega)> \\
&= \ I^0 - I^S \\
&= \ \sum_\alpha |\hat{c}_\alpha^{(0)}(x_s,\omega)|^2 - \sum_\alpha |\hat{d}_\alpha(x_r,\omega)|^2.
\end{aligned}
\tag{4.203}
$$

Substituting eq. (4.179) into eq. (4.203), and taking the ensemble average yield the power spectrum of the mean coherent field I^C:

$$
\begin{aligned}
I^C(x_r,\omega) &= \ \left\langle \|v_0^{(0)}(x_r,\omega)\|^2 \right\rangle_E \\
&= \ \sum_\alpha |\hat{c}_\alpha^{(0)}(x_s,\omega)|^2 - \sum_\alpha \sum_n \int_{x_s}^{x_r} \int_{x_s}^{x_r} \\
&\quad \times \left\{ \left\langle \gamma_n^2 \right\rangle_E \sum_{\beta,\nu} N_n(\xi_1,\xi_2) g_\beta^{n\dagger}(\xi_2) \tilde{P}_{\beta\alpha}^\dagger(x_r,\xi_2) \tilde{P}_{\alpha\nu}(x_r,\xi_1) g_\nu^n(\xi_1) \right\} d\xi_1 d\xi_2
\end{aligned}
$$

$$= \sum_\alpha |\hat{c}_\alpha^{(0)}(x_s,\omega)|^2 - \sum_n \int_{x_s}^{x_r} dx \left\langle \gamma_n^2 \right\rangle_E \int_0^\infty dr$$

$$\times \left\{ \sum_{\beta,\nu} N_n(r) g_\beta^{n\dagger}(x+r) \check{P}_{\beta\nu}(x+r,x) g_\nu^n(x) \right\}. \qquad (4.204)$$

To derive the last form of eq. (4.204), the properties of the coupled-mode propagator are used:

$$\sum_\alpha \check{P}_{\beta\alpha}^\dagger(x_r,\xi_2) \check{P}_{\alpha\nu}(x_r,\xi_1) = \sum_\alpha \check{P}_{\beta\alpha}(\xi_2,x_r) \check{P}_{\alpha\nu}(x_r,\xi_1)$$

$$= \check{P}_{\beta\nu}(\xi_2,\xi_1). \qquad (4.205)$$

To design an inverse problem for the roughness variance, eq. (4.204) is written in terms of the variance mutiplied by its sensitivity kernel:

$$I^C(x_r,\omega) = I^0 - \sum_n \int_{x_s}^{x_r} \left\langle \gamma_n^2 \right\rangle_E \mathcal{K}_n(x) dx, \qquad (4.206)$$

where the sensitivity kernel $\mathcal{K}_n(x)$ is defined as

$$\mathcal{K}_n(x) = \sum_{\alpha,\beta} \int_0^\infty N_n(r) g_\alpha^{n\dagger}(x+r) \check{P}_{\alpha\beta}(x+r,x) g_\beta^n(x) \, dr, \qquad (4.207)$$

where

$$\mathbf{g}^n(x) = (\hat{\mathbf{D}}^n + i\hat{\mathbf{E}}^n\hat{\mathbf{B}})\hat{\mathbf{c}}(x)$$

$$\approx (\hat{\mathbf{D}}^n + i\hat{\mathbf{E}}^n\hat{\mathbf{B}})\hat{\mathbf{c}}^{(0)}(x)$$

$$= (\hat{\mathbf{D}}^n + i\hat{\mathbf{E}}^n\hat{\mathbf{B}})\check{\mathbf{P}}(x,x_s)\hat{\mathbf{c}}^{(0)}(x_s), \qquad (4.208)$$

and

$$\hat{\mathbf{c}}^{(0)}(x_s) = \mathbf{u}^{\alpha*}(x_s,z_s;\omega) \cdot \mathbf{f}^s(\omega) e^{i\frac{\pi}{2}}. \qquad (4.209)$$

Note that the sensitivity kernel $\mathcal{K}_n(x)$ has the form of a spatial convolution of the stochastic effective source weighted by the autocorrelation function $N_n(r)$ (the centered Gaussian function). $\mathcal{K}_n(x)$ depends on the interface number n and the horizontal coordinate x while the sensitivity kernel for the perturbation of the material properties in 2-D is a function of x and z. In the sensitivity kernel, the correlation length

in the autocorrelation function $N_n(r)$ plays a role similar to the resolution length of the Backus-Glibert inversion method (Backus & Gilbert 1970). The Backus-Gilbert method is designed for a deterministic mathematical model, it considers the variance as the error of deterministic properties which can be reduced by decreasing resolution. Whereas, for the inverse problem of the stochastic process, the variance and correlation length are model variables that we wish to estimate. Therefore, there is no trade-off relation between the variance and the correlation length.

First, the variance of the boundary roughness $\langle \gamma_n^2 \rangle_E$ can be parametrized (Nolet 1990):

$$\left\langle \gamma_n^2 \right\rangle_E = \sum_{l=1}^{L} \eta_l^n f_l(x),$$ (4.210)

where the model vector η is defined as $\eta = (\eta_1^1, \eta_2^1, \cdots, \eta_L^{N_h})^t$ and $f_l(x)$ is a set of L basis functions of the horizontal distance x. N_h is the number of interfaces. Using eq. (4.210), eq. (4.206) can be written

$$\Psi(\eta, \omega) = \mathcal{K}\eta,$$ (4.211)

where $\Psi(\eta, \omega) = \left(I^S(\omega_1), I^S(\omega_2), \cdots, I^S(\omega_M) \right)$. The signal may be fit in the frequency domain by minimizing the objective function $F(\eta)$ (Nolet 1987; Scherbaum & Sato 1991):

$$F(\eta) = \frac{1}{2} \sum_{i=1}^{M} \int_0^{\Omega} |\Psi_i(\eta, \omega) - s_i(\omega)|^2 \, d\omega,$$ (4.212)

where M is the total number of spectra available, Ω is a sufficiently large frequency span, Ψ_i is the synthetic power spectrum corresponding to the ith signal time series, and s_i is the observed power spectrum. The objective function $F(\eta)$ can be minimized by the Hessian matrix $\mathcal{H}$ and the conjugate gradient $\tilde{d}$ (Nolet 1987):

$$\begin{aligned} \mathcal{H}(\eta)\Delta\eta &\approx -\nabla_\eta F(\eta) \\ &= \sum_{i=1}^{M} \int_0^{\Omega} \nabla_\eta \Psi_i \left[\Psi_i(\eta, \omega) - s_i(\omega) \right] d\omega, \end{aligned}$$ (4.213)

and

$$\tilde{d}^{i+1} = -(\nabla_\eta F)^{i+1} + \beta^i \tilde{d}^i,$$ (4.214)

where

$$\beta^i = \frac{|(\nabla_\eta F)^{i+1}|^2}{|(\nabla_\eta F)^i|^2}, \qquad \beta_0 = 0, \tag{4.215}$$

a^i denotes the value a for the ith iteration model η^i, and

$$\nabla_\eta = \left(\frac{\partial}{\partial \eta_1}, \frac{\partial}{\partial \eta_2}, \cdots, \frac{\partial}{\partial \eta_L} \right)^t. \tag{4.216}$$

From the least-squares fit of the predicted Q_S^{-1} curve to the observed data in the preceding section, the constant variance η^* and the constant correlation length a^* over the region are assumed to have been retrieved. Then the correlation length a^* may be applied over the whole propagation region, and the variance η^* can be used as an initial background value for the model parameter with unit block functions:

$$\left\langle \gamma_n^2 \right\rangle_E = \sum_{l=1}^L \eta^* f_l(x), \tag{4.217}$$

where

$$f_l(x) = H(x - x_{l-1}) H(x_l - x) \tag{4.218}$$

and $H(x)$ is the Heavyside unit step function.

The advantage of the power spectrum inversion compared to the inversion from the measurement of Q_S^{-1} explained in the preceding section is that range-dependence is considered in a parametrization of the variance, i.e., the range-dependent variance can be retrieved segment by segment.

4.11 Summary and Conclusion

The elastic wave scattering from stochastic rough surfaces has been treated in this paper by applying 1st order perturbation theory to the coupled mode equations. We have derived the evolution equation which describes the coupling from modes of the primary field to the modes of the scattered field.

The coupled-mode propagator is defined in the local mode space by applying the product integral to the evolution equation for the primary field. The coupled-mode

propagator is shown to be unitary, and the reciprocity theorem for the coupled-mode surface waves is demonstrated from the unitarity.

An integral equation formally identical to the Lippmann-Schwinger equation is also found for the propagator of the $\mathcal{O}(\varepsilon)$ system. By the diagram method, the Dyson equation is obtained for the mean propagator which enables us to synthesize the mean field including the effects of multiple scattering. The Bethe-Salpeter equation for the covariance of the propagator is also obtained, which can be used to analyze the effects of the multiple scattering on the envelope decay of the siganls.

We derived the expression for the modal scattering cross section and scattering Q_s from the Born approximation of the scattered field, and compute them for weakly varying reference structure. Based on numerical computations, first, we can conclude that the scattered intensity is sensitive to the magnitude of the impedance contrast across a boundary. That is, roughness between layers with similar impedance cannot greatly contribute to scattering. The slope of the reference boundary does not have a large effect on the scattered intensity because the reference structure can be thought as a stochastic process with an infinitely long correlation length. Also, each mode has the minimum Q_S^{-1} value at a different correlation length because of the different sampling by different modal wavelengths.

For the acoustic wave scattering problem in shallow water, the rough seabottom plays an important role in scattering of coherent signals through the interaction with the interface wave. Synthesis of Q_S^{-1} and the envelope of signals enable us to predict the temporal decay rate of signals.

The formula for the power spectra is expressed from the Born approximation of the coherent field and the inveerse problem is designed by iterative fitting of the synthetic power spectrum to the observed signals.

There should be futher work to study the Dyson equation and the Bethe-Salpeter equation for the propagator to study the multiple scattering problem. Solution of those equations applied to specific problems enable us to generate the mean field

signals and to predict the envelope decay including multiple scattering effect.

BIBLIOGRAPHY

Aki, K., 1969. Analysis of seismic coda of local earthquakes as scattered waves, *J. Geophys. Res.*, **74**, 615-631.

Aki, K. and Chouet, B., 1975. Origin of coda waves: Source, attenuation and scattering effects, *J. Geophys. Res.*, **80**, 3322-3342.

Aki, K. and Richards, P.G., 1980. *Quantitative Seismology, 2 volumes*, W. H. Freeman and Company, New York, NY.

Auld, B.A., 1990. *Acoustic Fields and Waves in Solids*, Vol. I, pp. 64-86, 2nd ed., Krieger, Malabar, FL.

Bachman, R.T., 1979. Acoustic anisotropy in marine sediments and sedimentary rocks, *J. Geophys. Res.*, **84**, 7661-7663.

Bachman, R.T., 1983. Elastic anisotropy in marine sedimentary rocks, *J. Geophys. Res.*, **88**, 539-545.

Backus, G.E., 1962. Long-wave anisotropy produced by horizontal layering, *J. Geophys. Res.*, **67**, 4427-4440.

Backus, G.E. & Gilbert, F., 1970. Uniqueness in the inversion of inaccurate gross earth data, *Phil. Trans. R. Soc. Lond.* **266**, 123-192.

Bahar, E., 1978. Full wave and physical optics solutions for scattered radiation fields by rough surfaces-energy and reciprocity relationships, *IEEE Trans. Ant. Prop.* **AP-26**, 603-614.

Bahar, E., 1980. Full wave solutions for scattered radiation fields from rough surfaces with arbitrary slope and frequency, *IEEE Trans. Ant. Prop.* **AP-28**, 11-21.

Bahar, E., 1990. Full wave solutions for the scattering of acoustic waves excited by arbitrary source distributions in irregular layered media, *Wave Motion* **12**, 301-314.

Bass, F.G. and Fuks, I.M., 1979. *Wave Scattering from Statistically Rough Surfaces*, Pergamon Press, Oxford, England.

Berge, P.A., Mallick, S., Fryer, G.J., Barstow, N., Carter, J.A., Sutton, G.H., and Ewing, J.I., 1991. In *situ* measurement of transverse isotropy in shallow-water marine sediments, *Geophys. J. Int.*, **104**, 241-254.

Berryman, J.G., 1979. Long-wave anisotropy in transversely isotropic media, *Geophysics* **44**, 869-917.

Boyles, C.A., 1984. *Acoustic Waveguides*, pp312-314, Wiley, New York, NY.

Buchen, P.W. and Ben-Hador, R., 1996. Free mode surface-wave computations, *Geophys. J. Int.*, **124**, 869-887.

Burridge, R. and Knopoff, L., 1964. Body-force equivalents for seismic dislocations, *Bull. seism. Soc. Am.*, **54**, 1875-1888.

Carlson, R.L., Schaftenaar, C.H. & Moore, R.P., 1984. Causes of compressional wave anisotropy in carbonate-bearing deep sea sediments, *Geophysics* **49**, 525-532.

Chernov, L.A., 1960. *Wave Propagation in a Random Medium*, McGraw-Hill Book Company Inc., New York, NY.

Chwieroth, F.S., Nagl, A., Überall, H. & Zarur, G.L., 1978. Mode coupling in a sound channel with range-dependent parabolic velocity profile, *J. Acoust. Soc. Am.* **64**, 1105-1112.

Cohen-Tannoudji, C., Diu, B. & Laloë, F., 1977. *Quantum Mechanics*, Vol. I, Hermann and John Wiley & Sons, Inc., Paris, France.

DeSanto, J.A. & Brown, G.S., 1985. Analytical techniques for multiple scattering from rough surfaces, in *Progress in Optics*, Vol. XXI, pp. 1-62, ed. E. Wolf, North-Holland, Amsterdam.

DeWitt-Morette, C., Maheshwari, A. & Nelson, B., 1979. Path integration in non-relativistic quantum mechanics, *Phys. Rep.* **50**, 255-372.

Dieci, L., 1992. Numerical integration of the differential Riccati equation and some related issues, *Siam J. Numer. Anal.*, **29**, 781-815.

Frisch, V., 1968. Wave propagation in random media, in *Probabilistic Methods in Applied Mathematics*, Vol. 1, pp. 76-198, ed. A.T. Barucha-Reid, Academic Press, New York, NY.

Evans, R.B., 1983. A coupled mode solution for acoustic propagation in a waveguide with stepwise depth variations of a penetrable bottom, *J. Acoust. Soc. Am.*, **74**, 188-195.

Evans, R., 1986a. The decoupling of stepwise coupled modes, *J. Acoust. Soc. Am.*, **80**, 1414-1418.

Evans, R., 1986b. The decoupling of seismic waves, *Wave Motion*, **8**, 321-328.

Ewing, J., Carter, J.A., Sutton, G.H. & Barstow, N., 1992. Shallow water sediment properties derived from high-frequency shear and interface waves, *J. Geophys. Res.*, **97**, 4739-4762.

Fawcett, J.A., 1993. A derivation of the differential equations of coupled-mode propagation, *J. Acoust. Soc. Am.*, **92**, 290-295.

Fryer, G.J. & Miller, D.J., 1986. Effects and consequences of transverse isotropy in the seafloor, in *Ocean Seismo-Acoustics; Low frequency Underwater Acoustics*, pp. 589-597, eds. Akal, T. & Berkson, J.M., Plenum Press, New York, NY.

Gao, L.S., Lee, L.C., Biswas, N.N., and Aki, K., 1983a. Comparison of the effect beween single and multiple scattering on coda waves for local earthquakes, *Bull. Seismol. Soc. Am.*, **73**, 377-390.

Gao, L.S., Biswas, N.N., Lee, L.C., and Aki, K., 1983b. Effects of multiple scattering on coda waves in a three-dimensional medium, *Pure Appl. Geophys.*, **121**, 3-15.

Gear, C.W., 1971. *Numerical Initial Value Problems in Ordinary differential Equations*, Prentice-Hall, Englewood Cliffs, NJ.

Gilbert, F. & Backus, G., 1966. Propagator matrices in elastic wave and vibration problems, *Geophysics* **31**, 326-332.

Gillette, G., 1994. Coupled modes in a waveguide with a range-dependent rigid basement, *J. Acoust. Soc. Am.*, **95**, 187-200.

Hall, M., 1986. The effects of variations in sound speed on coupling coefficients between acoustic normal modes in shallow water over a sloping bottom, *J. Acoust. Soc. Am.*, **79**, 332-337.

Hamilton, E.L., 1980. Geoacoustic modeling of the sea floor, *J. Acoust. Soc. Am.* **68**, 1313-1340.

Haskell, N.A., 1953. The dispersion of surface waves on multilayered media, *Bull. seism. Soc. Am.*, **43**, 17-34.

Hawker, K.E., 1978. Influence of Stoneley waves on plane-wave reflection coefficients: Characteristics of bottom reflection loss, *J. Acoust. Soc. Am.*, **64**, 548-555.

Hoshiba, M., 1991. Simulation of multiple-scattered coda wave excitation based on the energy conservation law, *Phys. Earth Planet. Inter.*, **67**, 46-54.

Ishimaru, A., 1978. *Wave Propagation and Scattering in Random Media*, vol. 2, Academic, San Diego, Calif.

Kennett, B.L.N., 1983. *Seismic Wave Propagation in Stratified Media*, Cambridge University Press, Cambridge, England.

Kennett, B.L.N., 1984. Guided-wave propagation in laterally varrying media-I. Theoretical development, *Geophys. J. R. astr. Soc.*, **79**, 235-255.

Knobles, D.P., 1994. Solutions of coupled-mode equations with a large dimension in underwater acoustics, *J. Acoust. Soc. Am.*, **96**, 1741-1747.

Kopnichev, Y.F., 1977. The role of multiple scattering in the formation of a seismogram's tail, *Izv. Acad. Sci. USSR Phys. Solid Earth*, **13**, 394-398.

Kuperman, W.A., 1975. Coherent component of specular reflection and transmission at a randomly rough two-fluid interface, *J. Acoust. Soc. Am.*, **86**, 1511-1522.

Kuperman, W.A. & Schmidt, H., 1989. Self-consistent perturbation approach to rough surface scattering in stratified elastic media, *J. Acoust. Soc. Am.*, **86**, 1511-1522.

Liu, J.-Y. Schmidt, H. & Kuperman, W.A., 1993. Effect of a rough seabed on the spectral composition of deep ocean infrasonic ambient noise, *J. Acoust. Soc. Am.*, **93**, 753-769.

Love, A.E.H., 1944. *A Treatise on the Mathematical Theory of Elasticity*, Dover, New York, NY.

Marquering, H. and Snieder, R., 1995. Surface-wave mode coupling for efficient forward modelling and inversion of body-wave phases, *Geophys. J. Int.*, **120**, 186-208.

Mattheij, R.M.M., 1985. Decoupling and stability of algorithms for boundary value problems, *SIAM Rev.*, **27**, 1-44.

Maupin, V., 1988. Surface waves across 2-D structures: a method based on coupled local modes, *Geophys. J.*, **93**, 173-185.

Maupin, V., 1992. Modelling of laterally trapped surface waves with application to Rayleigh waves in the Hawaiian swell, *Geophys. J. Int.*, **110**, 553-570.

Maupin, V. and Kennett, B.L.N., 1987. On the use of truncated modal expansion in laterally varying media, *Geophys. J. R. astr. Soc.*, **91**, 837-851.

McDaniel, S.T., 1982. Mode coupling due to interaction with the seabed, *J. Acoust. Soc. Am.*, **72**, 916-923.

McDaniel, S.T. & McCammon, D.F., 1986. Effect of sub-bottom inhomogenieties on shallow water spatial coherence, in *Ocean Seismo-Acoustics: Low-Frequency Underwater Acoustics*, pp. 397-405, eds. Akal, T. & Berkson, J.M., Plenum Press, New York, NY.

Morse, P.M. and Feshbach, H., 1953. *Methods of theoretical physics*, Vol. I, McGraw-Hill Book Company, Inc., New York, NY.

Milder, D.M., 1969. 'Ray and wave invariants for SOFAR channel propagation, *J. Acoust. Soc. Am.* **46**, 1259-1263.

Nagl, A., Überall, H., Haug, A.J. & Zarur, G.L., 1978. Adiabatic mode theory of underwater sound propagation in a range dependent environment, *J. Acoust. Soc. Am.* **63**, 739-749.

Nayfeh, A.H., 1973. *Perturbation methods*, John Wiley & Sons, Inc., New York, NY.

Nolet, G., 1990. Partitioned waveform inversion and two dimensional structure under the network of autonomously recording seismographs, lithosphere, *J. Geophys. Res.*, **95**, 8499-8512.

Nolet, G., 1987. Waveform tomography, in *Seismic Tomography*, chapter 13, pp. 301-322, ed. Nolet, G., D. Reidel Publishing Company, Hingham, Mass.

Oakley, D.W. & Vidmar, P.J., 1983. Acoustic reflection from transversely isotropic consolidated sediments, *J. Acoust. Soc. Am.* **73**, 513-519.

Odom, R.I., 1980. Experimental and Theoretical Investigations of Ocean-Earth Acoustic Coupling, Ph.D. Dissertation, Geophysics, University of Washington, Seattle.

Odom, R.I., 1986. A coupled mode examination of irregular waveguides including the continuum spectrum, *Geophys. J. R. astr. Soc.*, **86**, 425-453.

Odom, R.I., Park, M., Mercer, J.A., Crosson, R.S. & Paik, P.,1996. Effects of transverse isotropy on modes and mode coupling in shallow water, *J. Acoust. Soc. Am.*, **100**, 2079-2092.

Ogilvy, J.A., 1991. *Theory of Wave Scattering from Random Rough Surfaces*, IOP Publishing Ltd., Bristol, England.

Park, M. & Odom, R.I., 1997a. Effects of elastic heterogeneities and anisotropy on mode coupling and signals in shallow water, submitted to *J. Acoust. Soc. Am.*.

Park, M. & Odom, R.I., 1997b. The effect of stochastic rough interfaces on coupled-mode elastic waves, submitted to *Geophys. J. Int.*

Pierce, A.D., 1965. Extension of the method of normal modes to sound propagation in an almost-stratified medium, *J. Acoust. Soc. Am.* **37**, 19-27.

Postma, G.W., 1955. Wave propagation in a stratified medium, *Geophysics* **20**, 780-806.

Rutherford, S.R. & Hawker, K.E., 1981. Consistent coupled mode theory of sound propagation for a class of non-separable problems, *J. Acoust. Soc. Am.*, **70**, 554-564.

Rytov, S.M., Kravtsov, Yu.A. & Tatarskii, V.I., 1987. *Principles of statistical radiophysics vol. 1: Elements of random process theory*, Springer-Verlag, Berlin.

Rytov, S.M., Kravtsov, Yu.A. & Tatarskii, V.I., 1989. *Principles of statistical radiophysics vol. 4: Wave propagation through random media*, Springer-Verlag, New York, NY.

Saito, M., 1988. DISPER80: A Subroutine Package for the Calculation of Seismic Normal-Mode Solutions, in *SEISMOLOGICAL ALGORITHMS: Computational Methods and Computer Programs*, pp. 293-319, ed. Doornbos, D., Academic, San Diego, California.

Sato, H., 1977. Energy propagation including scattering effects: single isotropic scattering approximation, *J. Phys. Earth.*, **25**, 27-41.

Scherbaum, F. and Sato, H., 1991. Inversion of full seismogram envelopes based on the parabolic approximation: Estimation of randomness and attenuation in southeast Honshu, Japan, *J. Geophys. Res.*, **96**, 2223-2232.

Schreiner, A.E. & Dorman, L.M., 1990. Coherence lengths of seafloor noise: Effect of ocean bottom structure, *J. Acoust. Soc. Am.*, **88**, 1503-1514.

Schulman, L.S., 1981. *Techniques and applications of path integration* John Wiley & Sons, Inc., New York, NY.

Schultz, C.A. & Toksöz, 1993. Enhanced backscattering of seismic waves from a highly irregular, random interface: *SH* case, *Geophys. J. Int.*, **114**, 91-102.

Schultz, C.A. & Toksöz, 1994. Enhanced backscattering of seismic waves from a highly irregular, random interface: *P−SV* case, *Geophys. J. Int.*, **117**, 783-810.

Shilov, G.E., 1977. *Linear Algebra*, Dover Publication, Inc., New York, NY.

Snieder, R., 1986. 3-D linearized scattering of surface waves and a formalism for surface wave holography, *Geophys. J.*, **84**, 581-605.

Sobczyk, K., 1985. *Stochastic Wave Propagation*, Elsevier Science Publishing Co., New York, NY.

Stoneley, R., 1949. The seismological implications of aeolotropy in continental structure, *Monthly Notices Roy. Astron. Soc., Geophys. Suppl.*, **5**, 222-232.

Takeuchi, H. & Saito, M., 1972. Seismic surface waves, in *Seismology: Surface waves and earthquake oscillations* (methods in computational physics, Vol. 11), pp. 217-295, ed. Bolt, B.A., Academic Press, New York, NY.

Thomson, W.T., 1950. Transmission of elastic waves through a stratified solid medium, . *J. Appl. Phys.*, **21**, 89-93.

Urhig, L.F. & Van Melle, F.A., 1955. Velocity anisotropy in stratified media, *Geophysics* **20**, 774-779.

Wang, C.-Y. & Hermann, R.B., 1988. Synthesis of coda waves in layered medium, *Pageoph.*, **128**, 7-42.

Woodhouse, J.H., 1974. Surface waves in a laterally varying layered structure, *Geophys. J. R. astr. Soc.*, **37**, 461-490.

Wu, R.-S., 1985. Multiple scattering and energy transfer of seismic waves - separation of scattering effect from intrinsic attenuation -I. Theoretical modelling, *Geophys. J. R. astr. Soc.*, **82**, 57-80.

Appendix A

MAUPIN'S COUPLING MATRIX FOR A RANGE DEPENDENT FLUID-ELASTIC MEDIUM

We give the explicit expression for Maupin's coupling matrix for a fluid-elastic medium.

$$
\begin{aligned}
B_{qr} = {} & \frac{1}{k^q - k^r} \Bigg(\int_0^{h_1(x)} \Big(w_x^{q*} \dot{\rho} \omega^2 w_x^r + t^{q*} \Big(\frac{1}{\lambda} - \frac{\dot{p}^2}{\rho \omega^2} \Big) t^r + \frac{\partial t^{q*}}{\partial z} \frac{i}{\rho \omega^2} \frac{\partial t^r}{\partial z} \Big) dz \\
& + \int_{h_1(x)}^{\infty} \Big(\mathbf{w}^{q*} \dot{\rho} \omega^2 \mathbf{w}^r - \frac{\partial \mathbf{w}^{q*}}{\partial z} \dot{Q}_{33} \frac{\partial \mathbf{w}^r}{\partial z} - \mathbf{w}^{q*} i p \dot{Q}_{23} \frac{\partial \mathbf{w}^r}{\partial z} \\
& + \frac{\partial \mathbf{w}^{q*}}{\partial z} \dot{Q}_{32} i p \mathbf{w}^r - \mathbf{w}^{q*} \dot{Q}_{22} p^2 \mathbf{w}^r - \frac{\partial \mathbf{w}^{q*}}{\partial z} (C_{31} \dot{C}_{11}^{-1}) t^r - \mathbf{w}^{q*} i p (C_{21} \dot{C}_{11}^{-1}) t^r \\
& - t^{q*} (C_{11}^{-1} \dot{C}_{13}) \frac{\partial \mathbf{w}^r}{\partial z} + t^{q*} (C_{11}^{-1} \dot{C}_{12}) i p \mathbf{w}^r + t^{q*} \dot{C}_{11}^{-1} t^r \Big) dz \\
& + \sum_m \dot{h}_m \Big[-\mathbf{w}^{q*} \rho \omega^2 \mathbf{w}^r - \frac{\partial \mathbf{w}^{q*}}{\partial z} Q_{33} \frac{\partial \mathbf{w}^r}{\partial z} + \mathbf{w}^{q*} Q_{22} \mathbf{w}^r p^2 + \frac{\partial \mathbf{w}^{q*}}{\partial z} (C_{31} C_{11}^{-1}) t^r \\
& - t^{q*} (C_{11}^{-1} C_{13}) \frac{\partial \mathbf{w}^r}{\partial z} + t^q C_{11}^{-1} t^r \Big]_n \Bigg) \exp \Big(i \int_0^x (k^q - k^r) d\zeta \Big)
\end{aligned}
\qquad (A.1)
$$

The first integral is over the water column only, where $h_1(x)$ is the water-sediment interface, λ is the incompressibility of the water, and the overdot indicates the derivative with respect to range. There are also two additional terms that must be added to the summation over the interface terms. These two terms arise from the boundary conditions the water-sediment interface. An ideal inviscid fluid does not support shear, so the boundary condition at the fluid-solid bottom boundary requiring continuity of the tangential component of displacement is relaxed and replaced with a free slip boundary condition. This free slip boundary condition results in a physically unrealistic discontinuity in the tangential component of displacement w_x, which can

be remedied by including a small nonzero viscosity in the equations of motion for the fluid. The details are given by Maupin (1988).

On the solid side of the interface it is necessary to add

$$-i\dot{h}(k^q - k^r)(w_x^{q*}\tau_{zz}^r + \tau_{zz}^{q*}w_x^r) \qquad \text{(A.2)}$$

to the terms which already hold for a purely solid medium. On the fluid side of the interface it is necessary to add the term

$$-\dot{h}\left(-\frac{\partial t^{q*}}{\partial z}\frac{1}{\rho\omega^2}\frac{\partial t^r}{\partial z} - t^{q*}\left(\frac{1}{\lambda} - \frac{p^2}{\rho\omega^2}\right)t^r + w_x^{q*}\rho\omega^2 w_x^r\right). \qquad \text{(A.3)}$$

where t is the scalar pressure, λ is the fluid incompressibility, and p is the spatial wavenumber in the y (cross-range) direction. These additional interface terms must of course be multiplied by the global term:

$$\frac{1}{(k^q - k^r)}exp\left(i\int_0^x (k^q - k^r)d\zeta\right) \qquad \text{(A.4)}$$

Note that the first integral extends from the surface to the ocean bottom $h_1(x)$, and the second integral is over the semi-infinite halfspace comprising the sub-bottom from $h_1(x)$ to infinity. It would also be a simple matter to incorporate an additional solid layer at the surface to model the mode coupling in an ice covered sea.

Appendix B

STOCHASTIC COUPLING MATRICES FOR RAYLEIGH WAVES IN A TRANSVERSELY ISOTROPIC MEDIUM

The stochastic coupling matrices, $\mathbf{D}$ and $\mathbf{E}$ for Rayleigh waves in a transversely isotropic medium are calculated as an example. We substitute the appropriate transversely isotropic eigenfunctions into the expressions for $\mathbf{D}$ and $\mathbf{E}$ which are derived in Park & Odom (1997).

$$D_{qr} = \sum_n \gamma_n D_{qr}^n \exp\left\{ i \int_{x_s}^x (k^q(\xi) - k^r(\xi))\, d\xi \right\}, \tag{B.1}$$

$$E_{qr} = \sum_n \gamma_n E_{qr}^n \exp\left\{ i \int_{x_s}^x (k^q(\xi) - k^r(\xi))\, d\xi \right\}. \tag{B.2}$$

where

$$
\begin{aligned}
D_{qr}^n = \ & - \ \frac{\left\langle \dot{h}_n \right\rangle_E \left\langle \ddot{h}_n \right\rangle_E}{\left(1 + \left\langle \dot{h}_n \right\rangle_E^2\right)^2} \left[\frac{F^2 - AC}{C} k^r y_3^q y_3^r + \frac{F}{C} y_3^q y_2^r - y_1^q y_4^r \right]_n \\
& - \ \frac{\left\langle \dot{h}_n \right\rangle_E}{1 + \left\langle \dot{h}_n \right\rangle_E^2} \left[\left(\frac{F^2 - AC}{C} k^{r\,2} + \frac{F}{C}\rho\omega^2 \right) y_3^q y_1^r \right. \\
& - \left(\frac{F}{C} + \frac{F^2 - AC}{CL} \right) k^r y_3^q y_4^r \\
& + \left(\frac{F^2 - AC}{C} k^{r\,2} + \rho\omega^2 \right) y_1^q y_3^r + \frac{F}{C} k^R y_1^q y_2^r \Big]_n \\
& - \ i \frac{\left\langle \dot{h}_n \right\rangle_E^2}{1 + \left\langle \dot{h}_n \right\rangle_E^2} \left[\frac{F^2 - AC}{C} k^{r\,2} y_3^q y_3^r + \frac{F}{C} k^r y_3^q y_2^r - k^r y_1^q y_4^r \right]_n \\
& + \ i \frac{1}{1 + \left\langle \dot{h}_n \right\rangle_E^2} \left[\left(\frac{F^2 - AC}{C} k^{r\,2} + \rho\omega^2 \right) y_3^q y_3^r \right. \\
& - \rho\omega^2 y_1^q y_1^r + \frac{F}{C} k^r y_3^q y_2^r + k^r y_1^q y_4^r \Big]_n \tag{B.3}
\end{aligned}
$$

$$E_{qr}^m = - \frac{\left\langle \dot{h}_n \right\rangle_E^2}{1 + \left\langle \dot{h}_n \right\rangle_E^2} \left[\frac{F^2 - AC}{C} k^r y_3^q y_3^r + \frac{F}{C} y_3^q y_2^r - y_1^q y_4^r \right]_n \qquad \text{(B.4)}$$

where the elastic parameters A, C, F, L & N for transversely isotropic media are defined in the main text. The eigenfunction notation of Takeuchi & Saito (1972), $\{y_i; i = 1, 2, 3, 4\}$ is used. The square brackets indicate the jump across the interface, e.g.,

$$\left[\frac{F^2 - AC}{C} k_r y_3^q y_3^r \right]_n \equiv$$
$$\left(\frac{F_{n+1}^2 - A_{n+1} C_{n+1}}{C_{n+1}} - \frac{F_n^2 - A_n C_n}{C_n} \right) k_r y_3^q \left(z = \left\langle h_n \right\rangle_E \right) y_3^r \left(z = \left\langle h_n \right\rangle_E \right). \quad \text{(B.5)}$$

Appendix C

SCATTERING OPERATOR AND STOCHASTIC COUPLING MATRICES FOR RAYLEIGH WAVES IN AN ISOTROPIC MEDIUM

The matrix representations of the scattering operator $\mathbf{S}$ and its components $\mathbf{D}$ & $\mathbf{E}$ are derived for Rayleigh waves in an isotropic medium in terms of the deterministic coupling matrix $\hat{\mathbf{B}}$ and the stochastic coupling matrices, $\hat{\mathbf{D}}$ and $\hat{\mathbf{E}}$. We substitute the appropriate isotropic eigenfunctions into equations (4.71) & (4.72). The phase term is omitted (see eqs. (4.131) & (4.132)).

$$\mathbf{S}(x) = \hat{\mathbf{D}} + i\hat{\mathbf{E}}\hat{\mathbf{B}}, \tag{C.1}$$

$$\hat{D}_{\alpha\beta} = \sum_n \gamma_n \hat{D}^n_{\alpha\beta}, \tag{C.2}$$

$$\hat{E}_{\alpha\beta} = \sum_n \gamma_n \hat{E}^n_{\alpha\beta}. \tag{C.3}$$

where

$$
\begin{aligned}
\hat{D}^n_{\alpha\beta} = \ & \frac{\dot{h}^0_n \dot{h}^0_n}{\left(1 + \left(h^0_n\right)^2\right)^2} \left[\mathcal{D}k_\beta r^\alpha_1 r^\beta_1 + \mathcal{C}r^\alpha_1 r^\beta_4 + r^\alpha_2 r^\beta_3\right]_n \\
& - \frac{\dot{h}^0_n}{1 + \left(h^0_n\right)^2} \left[(\mathcal{D}k^2_\beta - \mathcal{C}\rho\omega^2)r^\alpha_1 r^\beta_2 + (\mathcal{B} - \mathcal{C})k_\beta r^\alpha_1 r^\beta_3 \right. \\
& \left. + (\mathcal{C}k_\beta + \rho\omega^2)r^\alpha_2 r^\beta_1 - \mathcal{A}r^\alpha_2 r^\beta_4\right]_n \\
& - i\frac{\left(h^0_n\right)^2}{1 + \left(h_n\right)^2} \left[\mathcal{D}k^2_\beta r^\alpha_1 r^\beta_1 + \mathcal{C}k_\beta r^\alpha_1 r^\beta_4 + k_\beta r^\alpha_2 r^\beta_3\right]_n \\
& + i\frac{1}{1 + \left(h^0_n\right)^2} \left[(\mathcal{D}k^2_\beta - \rho\omega^2)r^\alpha_1 r^\beta_1 - \rho\omega^2 r^\alpha_2 r^\beta_2 + \mathcal{C}k_\beta r^\alpha_1 r^\beta_4 - k_\beta r^\alpha_2 r^\beta_3\right]_n
\end{aligned} \tag{C.4}
$$

$$\hat{E}^n_{\alpha\beta} = - \frac{\left(\dot{h}^0_n\right)^2}{1 + \left(\dot{h}^0_n\right)E^2} \left[\mathcal{D}k_\beta r^\alpha_1 r^\beta_1 + \mathcal{C} r^\alpha_1 r^\beta_4 + r^\alpha_2 r^\beta_3\right]_n \qquad (C.5)$$

where the elastic parameters $\mathcal{A}$, $\mathcal{B}$, $\mathcal{C}$, & $\mathcal{D}$ are defined as

$$\mathcal{A} = \frac{1}{\lambda + 2\mu}, \qquad (C.6)$$

$$\mathcal{B} = \frac{4(\lambda + \mu)}{\lambda + 2\mu}, \qquad (C.7)$$

$$\mathcal{C} = \frac{\lambda}{\lambda + 2\mu}, \qquad (C.8)$$

$$\mathcal{D} = \frac{4\mu(\lambda + \mu)}{\lambda + 2\mu}. \qquad (C.9)$$

The deterministic coupling matrix $\hat{\mathbf{B}}$ is derived in Maupin (1988). Here, we use the eigenfunction notation of Aki & Richards (1980), $\{r_i; i = 1, 2, 3, 4\}$. The square brackets indicate the jump across the interface:

$$\left[\frac{\lambda}{\lambda + 2\mu} r^\alpha_1 r^\beta_4\right]_n \equiv \left(\frac{\lambda_{n+1}}{\lambda_{n+1} + 2\mu_{n+1}} - \frac{\lambda_n}{\lambda_n + 2\mu_n}\right) r^\alpha_1 \left(z = h^0_n\right) r^\beta_4 \left(z = h^0_n\right). \qquad (C.10)$$

VITA

Name, Birth date:

Minkyu Park (Born 3 July 1961)

Education:

Diploma, Kyung Shin High School, Seoul, Korea, 1980

B.S., Seoul National University (Geological Sciences), Seoul, Korea, 1990

Ph.D., University of Washington (Geophysics), Seattle, Washington, 1997

Publication:

Park, M., R.I. Odom, and J.A. Mercer, 1993. Mode Coupling and Diffusion of Bottom Interacting Seismo-Acoustic Signals in Shallow Water, (Abstract), EOS, **74**, p. 396.

Park, M., R.I. Odom, and J.A. Mercer, 1994. Stochastic Extensions to Coupled Mode Surface Waves, (Abstract), EOS, **75**, p. 420.

Park, M., R.I. Odom, and J.A. Mercer, 1995. The Effect of Lateral Heterogeneities on Energy Conversion to Stochastic Modes. (Abstract), EOS, **76**, p. 371.

Park, M., R.I. Odom, and J.A. Mercer, 1996. Elastic Wave Scattering from Random Rough Surfaces, (Abstract), EOS, **77**, p. 468.

Odom, R.I., M. Park, J.A. Mercer, R.S. Crosson and P. Paik, 1996. Mode Coupling in Shallow Water with a Transversely Isotropic Bottom, *J. Acoust. Soc. Am.*, **100**, 2079-2092.

Park, M. and R.I. Odom, 1997a. Effects of elastic heterogeneities and anisotropy on mode coupling and signals in shallow water, submitted to *J. Acoust. Soc. Am.*

Park, M. and R.I. Odom, 1997b. The effect of stochastic rough interfaces on coupled-mode elastic waves, submitted to *Geophys. J. Int.*